UNIVERSITY OF CALIFORNIA
Santa Barbara

Development of Nonlinear and Coupled Microelectromechanical Oscillators for Sensing Applications

A Dissertation submitted in partial satisfaction
of the requirements for the degree of

Doctor of Philosophy

in

Mechanical Engineering

by

Barry Ernest DeMartini

Committee in Charge:

Professor Kimberly L. Turner, Chair

Professor Jeff Moehlis

Professor Karl J. Åström

Professor Noel C. MacDonald

Professor Steven W. Shaw

September 2008

The Dissertation of
Barry Ernest DeMartini is approved:

Professor Jeff Moehlis

Professor Karl J. Åström

Professor Noel C. MacDonald

Professor Steven W. Shaw

Professor Kimberly L. Turner, Committee Chairperson

August 2008

Development of Nonlinear and Coupled Microelectromechanical Oscillators for Sensing Applications

by

Barry Ernest DeMartini

Acknowledgements

First of all, I would like to dedicate this dissertation to my parents, Sharon and Ernie, my brothers, Kevin and Joel, and my girlfriend Michele for their unconditional love and support over the past years.

I would like to give special thanks to my advisors, Kimberly Turner and Jeff Moehlis, for giving me the opportunity to work in their research groups, for their guidance, and for all that they have taught me over the past five years. I would also like to thank Steve Shaw, Karl Åström, and Noel MacDonald for being on my committee and for their vital input on the various projects that I have worked on in graduate school.

I would like to thank Jeff Rhoads and Nick Miller for the valuable collaborations and for being such great people to work with. I would also like to thank past and present members of Kimberly Turner's group, Raji Baskaran, Wenhua Zhang, Weibin Zhang, Laura Oropeza, Abhishek Srivastava, Mike Requa, Mike Northen, Matt Garten, Kyle Owen, Holly Butterfield, Mark Zielke, Benedikt Zeyen, Kari Moran, John Tamelier, Sathya Chary, Chris Burgner, Zi Yie, and Ashfaque Uddin, and the Jeff Moehlis' group Lina Kim, Allison Kolpas, Per Danzl, and Margot Kimura, who have all helped me through this endeavor in their own way. Finally, I would like to thank Dave Bothman for all of his help with lab equipment and the cleanroom staff for all of their advise on fabrication.

The content and figures in Chapter 2 and 3 is reprinted with permission from "B.E. DeMartini, J.F. Rhoads, K.L. Turner, S.W. Shaw, and J. Moehlis, Linear and Nonlinear Tuning of Parametrically Excited MEMS Oscillators. Journal of Microelectromechanical Systems, 16(2): p. 310-318, 2007. (©2007 IEEE)" and "B.E. DeMartini, H.E. Butterfield, J. Moehlis, and K.L. Turner, Chaos for a Microelectromechanical Oscillator Governed by the Nonlinear Mathieu Equation, Journal of Microelectromechanical Systems, 16(6): p. 1314-1323, 2007. (©2007 IEEE)", respectively.

Figures 6.1, 6.4, 6.5, 6.7, 6.8, and 6.9 are reprinted with permission from "Barry E. DeMartini, Jeffrey F. Rhoads, Steven W. Shaw, Kimberly L. Turner, A single input-single output mass sensor based on a coupled array of microresonators, Sensors and Actuators A Physical, 137(1): p. 147-156, 2007. (©2007 Elsevier)", "Jeff F. Rhoads, Barry E. DeMartini, Steve W. Shaw, and Kimberly L. Turner. A SISO Multi-Analyte Sensor Based on a Coupled Microresonator Array, 2006 ASME Mechanical Engineering Congress and Exposition, Chicago, Il 2006. (©2006 ASME)", and "Barry E. DeMartini, Jeff F. Rhoads, Steve W. Shaw, and Kimberly Turner, A Resonant SISO Sensor Based on a Coupled Array of Microelectromechanical Oscillators, Hilton Head 2006: A Solid-State Sensor, Actuator, and Microsystems Workshop, Hilton Head, SC 2006. (©2006 Transducer Research Foundation)".

Finally, Figures 7.1, 7.7, 7.10, and 7.11 are reprinted with permission from: "Barry E. DeMartini, Jeffrey F. Rhoads, Mark A. Zielke, Kyle G. Owen, Steven W. Shaw, and Kimberly L. Turner, A single input-single output coupled microresonator array for the detection and identification of multiple analytes, Applied Physics Letters, 93(5): 054102, 2008. (©2008 American Institute of Physics)."

Curriculum Vitæ

Barry Ernest DeMartini

Education

September 2008	Doctor of Philosophy, Mechanical Engineering, University of California, Santa Barbara.
2003	Bachelor of Science, Mechanical Engineering, University of California, Santa Barbara.

Experience

Summer 2000	Intern, Bovis Lend Lease, San Francisco, CA.
Summer 2001	Intern, Agilent Technologies, Rohnert Park, CA.
Summer 2003	Intern, Friedman Research Corp., Santa Barbara, CA.
Fall/Winter 2003	Teaching Assistant, University of California, Santa Barbara.
Summer 2006	Mentor, Summer Institute in Mathematics and Science (SIMS), University of California, Santa Barbara.
2007 – 2008	Mentor, Expanding Pathways to Science, Engineering, and Mathematics (EPSEM), University of California, Santa Barbara.
2004 – 2008	Graduate Research Assistant, University of California, Santa Barbara.

Publications

- J.F. Rhoads, S.W. Shaw, K.L. Turner, J. Moehlis, **B.E. DeMartini**, and W. Zhang. *Generalized parametric resonance in electrostatically-actuated microelectromechanical oscillators.* Journal of Sound and Vib., 296 (4-5): 797-829, 2006.
- **B.E. DeMartini**, J.F. Rhoads, K.L. Turner, S.W. Shaw, and J. Moehlis. *Linear and nonlinear tuning of parametrically excited MEMS oscillators.* Journal of Microelectromechanical Systems, 16 (2): 310-318, 2007.
- G. Schitter, K.J. Astrom, **B. DeMartini**, P.J. Thurner, K.L. Turner, and P.K. Hansma. *Design and modeling of a high-speed AFM-scanner.* IEEE Transactions on Control Systems Technology, 15 (5): 906-915, 2007.
- **B.E. DeMartini**, J.F. Rhoads, S.W. Shaw, and K.L. Turner. *A single input-single output mass sensor based on a coupled array of microresonators.* Sensors and Actuators A: Physical, 137: 147-156, 2007.
- **B.E. DeMartini**, H.E. Butterfield, J. Moehlis, and K.L. Turner. *Chaos for a microelectromechanical oscillator governed by the nonlinear mathieu equation.* Journal of Microelectromechanical Systems, 16 (6): 1314-1323, 2007.
- **B.E. DeMartini**, J.F. Rhoads, M.A. Zielke, K.G. Owen, S.W. Shaw, and K.L. Turner. *A single input-single output coupled microresonator array for the detection and identification of multiple analytes.* Submitted to Applied Physics Letters. 2008.

Conference Proceedings

- J.F. Rhoads, S.W. Shaw, K.L. Turner, J. Moehlis, **B.E. DeMartini**, and W. Zhang. *Nonlinear response of parametrically-excited MEMS.* ASME International Design Engineering Technical Conferences, 20th Biennial Conference on Mechanical Vibration and Noise, Long Beach, California, 2005.

- **B. DeMartini**, J. Moehlis, K. Turner, J. Rhoads, S. Shaw, and W. Zhang. *Modeling of parametrically excited microelectromechanical ocillator dynamics with application to filtering.* IEEE Sensors, 4th IEEE Conference on Sensors, Irvine, California, 2005.

- **B.E. DeMartini**, J. F. Rhoads, S. W. Shaw, and K. L. Turner. *A resonant SISO sensor based on a coupled array of microelectromechanical oscillators.* Hilton Head: A Solid-State Sensor, Actuator, and Microsystems Workshop, Hilton Head, South Carolina, 2006.

- G. Schitter, K.J. Astrom, **B. DeMartini**, G.E. Fantner, K. Turner, P.J. Thurner, and P. K. Hansma. *Design and modeling of a high-speed scanner for atomic force microscopy.* American Control Conference, Minneapolis, Minnesota, 2006.

- J.F. Rhoads, **B.E. DeMartini**, S.W. Shaw, and K.L. Turner. *A SISO, multi-analyte sensor based on a coupled microresonator array.* ASME Mechanical Engineering Congress and Exposition, Chicago, Illinois, 2006.

- **B.E. DeMartini**, H.E. Butterfield, J. Moehlis, and K.L. Turner. *Prediction and validation of chaotic behavior in an electrostatically actuated microelectromechanical oscillator.* Transducers 2007 and Eurosensors XXI, Lyon, France, 2007.

Conference Talks

- J.F. Rhoads, S.W. Shaw, K.L. Turner, **B.E. DeMartini**, J. Moehlis, and W. Zhang. *Generalized parametric resonance in electrostatically driven MEM oscillators.* SIAM Conference on Applications of Dynamical Systems, Snowbird, Utah, 2005.

- J.F. Rhoads, S.W. Shaw, K.L. Turner, **B.E. DeMartini**, J. Moehlis, and W. Zhang. *Generalized parametric resonance in electrostatically-actuated microelectromechanical systems.* ENOC, 5th EUROMECH Nonlinear Dynamics Conference, Eindhoven, The Netherlands, 2005.

- **B.E. DeMartini**, H.E. Butterfield, J. Moehlis, and K.L. Turner. *Chaotic behavior for an electrostatically actuated microelectromechancial oscillator.* SIAM Conference on Applications of Dynamical Systems, Snowbird, Utah, 2007.

- **B.E. DeMartini**, J.F. Rhoads, M.A. Zielke, K.G. Owen, S.W. Shaw, and K.L. Turner. *Detection and identification of multiple chemicals using a single input-single output coupled microresonator array.* International Workshop on Nanomechanical Cantilever Sensors, Mainz, Germany. 2008.

Abstract

Development of Nonlinear and Coupled Microelectromechanical Oscillators for Sensing Applications

Barry Ernest DeMartini

Microelectromechanical systems (MEMS) have gained a great deal of interest over the years due to their small size, low power consumption, ability to be batch fabricated, and ability to be integrated with on-chip electronics. These benefits, coupled with the fact that their minute masses and high frequencies lead to unprecedented sensitivities, make MEMS extremely attractive for sensing applications. To date, the conventional approach to these applications has been to utilize linear, uncoupled microresonators. While this method has proved to be successful, nonlinear and/or coupled MEMS resonators possess rich dynamic behavior that is not obtainable with linear, uncoupled MEMS resonators. This dissertation is focused on exploiting nonlinearity and coupling to improve the performance of MEMS resonators in sensing applications.

The first part of this dissertation investigates a highly tunable nonlinear parametrically excited MEMS for filtering and mass sensing applications. The device utilizes two sets of noninterdigitated comb drives, one for tuning and one for actuation, that allow the effective linear and nonlinear stiffness to be electrostatically

tuned. This work focuses on the design, fabrication, and testing of tunable parametrically excited MEMS oscillators to demonstrate a novel linear and nonlinear tuning scheme developed for creating bandpass filters with nearly ideal stopband rejection and sharp response roll-off. The tunability of these nonlinear oscillators is also shown to allow chaos under certain conditions. Using Melnikov's method, a criterion for the existence of chaos is derived. Numerical and experimental investigations verify the existence of chaos for certain parameter sets.

The second part of this dissertation details the theoretical and experimental study of a novel mass sensor array capable of detecting multiple analytes with a single input and single output (SISO) signal. This sensor differs from traditional mass sensor arrays in that it exploits vibration localization in an array of coupled, frequency mistuned microbeams. The modeling, analysis, and design of these mass sensors is presented. In the experimental portion of this work a variety of devices are created to help prove the concept and evaluate the viability of the sensor. In the process, SISO detection and identification of multiple chemicals is demonstrated for the first time and an innovative concept for a high-Q SISO multi-analyte biosensor is presented. The current SISO multi-analyte chemical sensor achieves femtogram mass sensitivities when operated in air, which shows promise for this technology in future sensing applications.

Contents

List of Figures

List of Tables

Chapter 1

Introduction

In Richard Feynman's famous lecture, "There's Plenty of Room at the Bottom" in 1959 [44], he discusses the enormous potential for a field of science where manipulating, controlling, and measuring individual atomic sized particles is possible. Since then the extremely broad field of nanotechnology has grown and impacted a vast number of technical application areas. In the early 1980's the scanning tunneling microscope was developed [19, 18] and allowed for the detection of forces as small as attonewtons (10^{-18} N). Shortly after, in 1990, this tool was used by IBM researchers to manipulate individual xenon atoms [40]. Another extremely valuable tool emerged in 1986, the atomic force microscope [17, 110, 121, 109], which gave scientists the ability to image at the atomic scale. Recently, nanomechanical sensors have demonstrated the ability to sense the spin of a single electron [107]

and detect zeptogram (10^{-21} g) mass changes [143]. The unprecedented sensitivities achieved with micro-/nano- scale mechanical structures are largely due to their ultra-small size, which leads to favorable scaling benefits. Not surprisingly, micro- and nano- electromechanical systems (MEMS and NEMS, respectively) have gained a lot of interest in nanotechnology applications over the years.

In recent years, the development of MEMS has been made possible by the innovation of silicon-based fabrication technology that has been leveraged from the IC industry [91]. As a result, MEMS have the unique ability to be fabricated on-chip with Complimentary Metal-Oxide-Semiconductor (CMOS) electronics and batch fabricated to reduce the overall fabrication costs. In addition, their small size, low power consumption, and ability to operate in harsh environments [20] makes them ideal candidates for applications such as chemical/biological sensing, inertial sensing, signal filtering, and switching.

To date, MEMS research in the above application areas has focused on the development of single-degree-of-freedom (SDOF), linear resonators. While these devices have proven to be successful, recent work has shown that nonlinear and/or coupled MEMS resonators possess unique properties that can potentially lead to improved performance over conventional linear, uncoupled MEMS resonators. This dissertation will primarily focus on the development of novel nonlinear and coupled MEMS resonators for mass sensing applications. Specifically, the unique

tunability of a nonlinear MEMS oscillator that has been proposed for mass sensing and filtering applications [147, 148, 151, 104] is investigated experimentally and interesting phenomena such as chaos are predicted and verified. The other portion of the dissertation involves the development of a coupled microresonator array that allows for the detection of multiple analytes with a single input signal and single output signal. The remainder of this chapter will provide background on mass sensing, nonlinear MEMS, and coupled MEMS oscillators, and it will also motivate and discuss the novel developments presented in this dissertation.

1.1 Mass Sensing

Over the past twenty years, mass sensors based on micro- and nano-mechanical resonators have gained a significant amount of attention. Early studies showed that the resonance frequency characteristic to a microresonator can be used to determine the presence of an analyte on its surface [58, 59, 129, 130]. Since then mass sensors have been proposed for a host of chemical [15, 54, 71, 89, 93, 94, 131, 155] and biological [26, 23, 53, 61, 62, 63, 68, 86, 99, 122] sensing applications (e.g. for medical research and diagnostics, national security and defense, and public health and safety). Due to their small masses and high frequencies, these sensors have shown ground breaking sensitivities in recent years. Possibly the most

impressive demonstration was by Yang *et al* [143], who demonstrated a mass sensitivity of several zeptograms (10^{-21} g) for a nanoscale resonator operated in an ideal environment (ultra-low temperature and ultra-low pressure). By integrating measurement electronics on-chip with the resonator, femtogram [45] and, more recently, attogram resolution [136] has been achieved in air using capacitive readout. Ekinci *et al* have established an expression for the theoretical limit, which has been widely used to determine the ultimate sensitivity of mass sensors [42].

Resonance-based mass sensing involves the binding of an analyte to a chemically specific or partially specific surface, which physically changes the mass and/or stiffness of the resonant structure. Since the resonance frequency of the sensor is related to the effective stiffness (k_{eff}) and effective mass (m_{eff}) of a given resonant mode by $\omega_0 = \sqrt{k_{eff}/m_{eff}}$, these changes result in a resonance shift, which can be tracked in real-time. These sensors effectively transduce a chemomechanical process into an electrical signal to facilitate detection. Figure 1.1 shows a simulated gain and phase response for a conventional linear, single-degree-of-freedom (SDOF) resonator before (black curves) and after (blue curves) mass addition. Notice that the added mass causes a downward shift in resonance frequency. One method for tracking these resonance shifts, commonly referred to as slope detection, involves driving the oscillator at a fixed frequency near resonance and tracking the amplitude of oscillation. When the resonance frequency

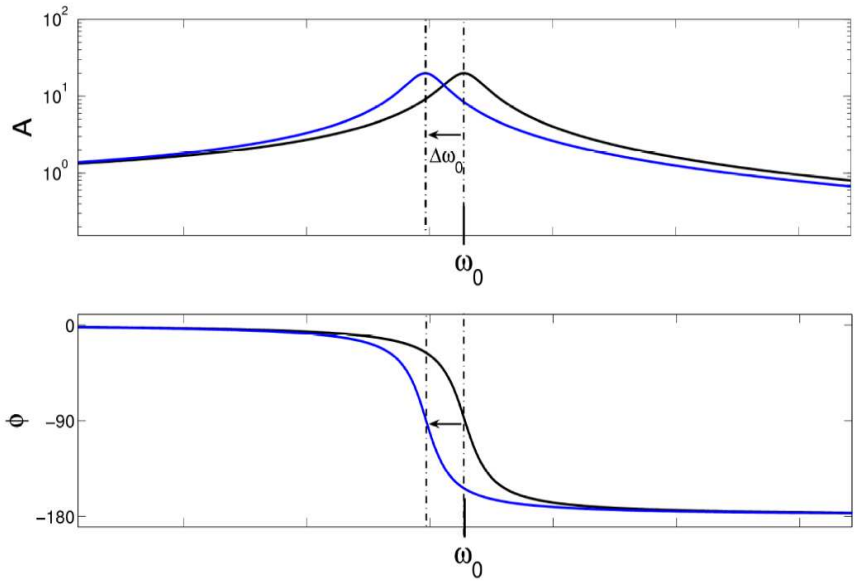

Figure 1.1: Resonant mode mass sensing concept depicting the the amplitude (top panel) and phase (bottom panel) responses before (black curve) and after (blue curve) mass loading.

shifts, the amplitude changes due to the sloped nature of the Lorentzian [78, 5]. High Q-values ($Q = m_{eff}\omega_0/c$, where c is the damping coefficient) achievable with microresonators lead to large time constants, which ultimately increase measurement time for this method [5]. Phase locked loop and self-excitation methods have become popular for mass sensing because they allow for the direct measurement of resonance frequency and bypass the issues associated with slope detection [127, 128, 41, 42, 67]. To facilitate detection, these MEMS resonators can be sensed (electrostatically, piezoelectrically, piezoresistively, optically, or magnetically) and actuated (electrostatically, piezoelectrically, magnetically, and thermally) using a

number of methods, which are typically chosen based on the specific needs of the application.

A single linear mass sensor with a functionalized surface is capable of detecting a single analyte. Arrays of mass sensors with differently functionalized surfaces have been studied to facilitate the detection of multiple analytes [15, 70, 86]. Unfortunately, when an array of isolated resonators is used, individual inputs and outputs are required to address each sensor in the array. For large arrays this leads to increased hardware and signal processing, which therefore increase the cost and complexity of the overall system [54, 71]. This work seeks to circumvent this issue by exploiting coupling in an array of microresonators to create a sensor that is capable of detecting multiple analytes with a single input and single output (SISO) signal (see Section 1.3.1 for a more thorough overview of the topic).

1.2 Nonlinear MEMS

Nonlinearities inherent in MEMS resonators have historically been avoided in many applications. These nonlinear effects often arise from mechanical spring hardening and/or nonlinear forcing. Typically nonlinear effects are avoided by operating the MEMS resonator below a critical displacement and forcing amplitude, which sets a linear threshold. This places a limit on the dynamic range

(the range between the maximum output amplitude and the noise floor) of the oscillator, which becomes crucial for nanomechanical resonators where the noise floor is inherently small [95]. Operating MEMS resonators in a nonlinear regime above the linear limit leads to increased dynamic range and a number of other benefits that are discussed below.

Recently, microelectromechanical oscillators exploiting parametric resonance have gained attention due to their benefits over conventional linear based micro-oscillators. Parametric resonance in MEMS was first proposed for amplification of harmonically excited oscillators in [108], and since then parametric excitation has been investigated for improving the performance of scanning probe microscopes [134], mass sensors [148, 150, 151, 102, 103], single frequency bandpass filters [116, 104], and inertial sensors [90]. Some of the promising features of parametrically excited MEMS reported in these applications include highly tunable dynamic behavior, extremely sharp response roll-off and nearly ideal stopband rejection, improved dynamic range, improved sensitivity in ambient conditions, and the ability to achieve high sensitivities without device scaling. Parametric resonance has also been observed in nanowire resonators [145] and coupled cantilevers [82, 21].

Characteristic to these devices, which feature time and displacement varying coefficients, is the ability to resonate when driven at frequencies near $2\omega_0/n$, where

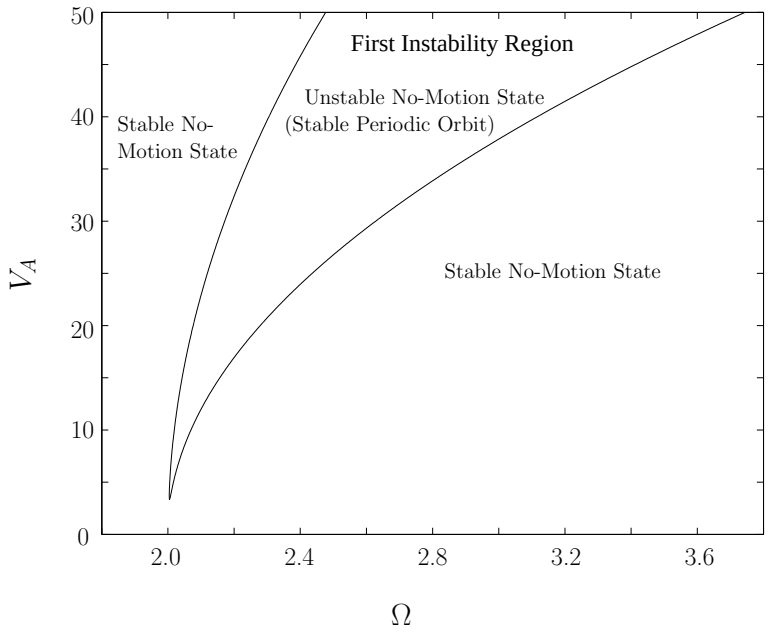

Figure 1.2: Representative first parametric region of instability in excitation voltage amplitude V_A vs. nondimensional frequency Ω space.

n is an integer greater than or equal to one and ω_0 is the natural frequency [83]. In the aforementioned applications the oscillator's primary parametric resonance region was utilized, corresponding to $n = 1$, where the the oscillator is driven near twice its resonant frequency. Driving an oscillator in this manner results in a wedge shaped instability region, such as that shown in Figure 1.2, where the oscillator remains motionless outside the wedge and transitions sharply to (relatively) large amplitude oscillatory motion inside the wedge. These sharp transitions to large amplitude motion are promising for a variety of applications.

A thorough analysis of the governing equation of motion has provided an accurate model of the dynamic response of parametrically excited MEMS devices

[105, 36, 3], which has compared well with experimental results. Gaining a full understanding of how these devices behave is vital for successful implementation. As a result, the goal of this work will be to investigate, both experimentally and theoretically, the dynamics of a class of tunable parametrically excited MEMS oscillator, which has recently shown promise for filtering and mass sensing applications. This work is introduced below.

1.2.1 Linear and Nonlinear Tuning

In recent work, parametrically excited MEMS have shown unique tuning capabilities [4, 147, 104, 38]. The tunability and abrupt nature of their stability boundaries allows parametrically exited MEMS to operate as bandpass filters with extremely sharp response roll-off and nearly ideal stopband rejection [105]. Also, the ability to tune and manipulate the frequency response characteristics is desirable for mass sensing applications [147, 148, 149, 151], where parametric excitation has been proposed for improving sensitivity metrics. It is envisioned that the unique flexibility of these devices will make them attractive for many applications in the future.

Recently techniques have been developed that allow for frequency tuning of general MEMS oscillators, which include localized thermal stressing of mechanical beam structures [101], power dissipation through filament annealing [140], resistive

heating to induce thermal strains in MEMS resonators [125], and electrostatic tuning for parallel plate capacitor and comb finger driven oscillators [35, 153, 144, 87]. While these tuning techniques aid in the design and implementation of a variety of MEMS devices, the tuning techniques in this study are unique to nonlinear parametrically excited devices and offer a high degree of tunability. Specifically, the oscillators studied in Chapters 2 and 3 make use of two sets of noninterdigitated comb drives. An AC signal is applied to one comb drive set to provide a time- and displacement-dependent force that drives the device. To the second set, a DC voltage is applied to tune the effective linear and nonlinear stiffness of the device.

In the Chapter 2, two oscillators are designed, fabricated, and tested in order to demonstrate the tuning concepts developed in [104]. Specifically, a linear tuning scheme is used to rotate the instability region, and a nonlinear tuning scheme is used to achieve desired hardening or softening behavior in the system's response. A single frequency filter, utilizing these tuning concepts, has been successfully realized with simulations [104]. Despite this work's emphasis on filtering applications, the tuning methods can be leveraged in any application where the dynamics inherent to parametric oscillators need to be manipulated (e.g., resonant mass sensors based on parametric resonance [148]).

1.2.2 Chaotic Behavior

Chaotic behavior has been discovered and reported for many physical systems. A classical example of a chaotic system is the Lorenz equations [76], which were derived to help understand the dynamics of cellular convection. Chaos due to various mechanisms has also been reported for nonlinear MEMS oscillators, including AFM microcantilevers [14, 10, 9, 60, 64], an in-plane MEMS oscillator with separated comb drive actuators for signal encryption applications [141], an electrostatically actuated MEMS cantilever control system [75], and MEMS oscillators based on variable gap capacitors [77, 34]. To the author's knowledge, the presence of chaos has not been thoroughly investigated for the tunable oscillators with time varying linear and nonlinear stiffness terms discussed above.

Knowledge of the conditions that cause such behavior to occur is important both for creating devices that exploit chaotic vibrations for applications such as signal encryption and for creating robust devices with predictable dynamic behavior. Here, Melnikov's method [52] has been employed to define the regions of parameter space where homoclinic chaos can occur. Numerical analysis was used to study the system's behavior for various parameter sets and to verify the result from Melnikov's method. Finally, a MEMS oscillator was designed and fabricated such that for a range of applied voltages and driving frequencies chaos

is predicted to occur from Melnikov's method. The chaotic behavior of this device was verified experimentally using a laser vibrometer.

1.3 Coupled MEMS

Both linear and nonlinear coupled MEMS resonators have gained a fair amount of attention in recent years. For instance, recent developments have enabled high frequency, high quality factor signal filters using arrays of mechanically coupled linear microresonators [73, 84, 85, 139]. The effect of mechanical and electrostatic coupling on closely spaced cantilevers for for parallel scanning probe microscopy applications was found to exhibit strongly nonlinear behavior, which is important to understand for optimizing the device performance [82]. For a larger array of electrostatically coupled, parametrically excited microbeams, the tunability of collective modes of vibration was demonstrated, which shows promise for optomechanical signal processing applications [22, 74]. Further studies showed that synchronization can occur in these coupled lattices [33], which leads to large amplitude oscillations of the entire lattice at a single frequency, even in the presence of small fabrication induced imperfections. Large arrays of micromechanical oscillators have also been found to exhibit highly localized structural vibrations, which result from disorder and nonlinear coupling in the lattice [111, 113, 112, 146]. Re-

cently, coupled micromechanical oscillators have been proposed for increasing the sensitivity of mass sensors [118, 117, 98]. In the present work, arrays of coupled microbeams are studied for mass sensing applications, but for a different purpose.

1.3.1 SISO Multi-Analyte Mass Sensor

As discussed in section 1.1, conventionally, arrays of uncoupled mass sensors are conventionally utilized to enable the detection of multiple analytes. In this case, however, multiple input signals and output signals are required to address each resonator in the array. For large isolated arrays, this leads to increased hardware and signal processing requirements, which ultimately lead to increased cost and complexity [54, 71]. In this dissertation, a novel sensor platform that is capable of detecting multiple analytes with a single input signal and single output signal is presented. This sensor technology is enabled by exploiting vibration localization [7, 56, 92, 6, 65] in an array of coupled, frequency-mistuned microbeams.

In this dissertation, the theoretical work presented in Chapter 5, which includes a discussion of the mathematical model, the frequency response, design considerations, and sensor metrics, is used to realize three generations of SISO multi-analyte mass sensors. The first generation sensor, detailed in Chapter 6, is used to experimentally investigate the SISO multi-analyte mass sensor concept.

In this investigation the concept is successfully proved and some key issues are are observed. Knowledge of these issues helped improve the performance of the second generation device detailed in Chapter 7. With the second generation device, the microbeams are functionalized with different polymer coatings, and single input-single output detection and identification of multiple chemicals is demonstrated for the first time. By self-exciting the sensor using positive feedback, the coupled system's resonances are tracked in real-time. Using this method, the sensor is shown to have a mass sensitivity of 59 fg in air, which clearly demonstrates this sensor's ability of achieve high sensitivities in realistic environments. Finally, the concept for a third generation SISO multi-analyte biosensor is outlined in Chapter 8. This unique structure makes use of an array of coupled microbeams that serve as resonators and microchannels [24, 25, 26]. By allowing liquids to flow through the inside of the microbeams, while the surrounding environment is pumped down to low pressure, issues associated with operating the resonator in a low-Q environment are eliminated.

Chapter 2

Tuning of Parametrically Excited MEMS Oscillators

In the work detailed in this chapter, tuning techniques for a class of nonlinear parametrically excited microelectromechanical (MEM) oscillator are investigated and demonstrated experimentally (also see [38]). Of interest in this study is the oscillator's primary parametric resonance region, where the the oscillator is driven near twice its resonant frequency. Operating an oscillator in this manner leads to a highly sensitive response where the oscillator sharply transitions from a no motion state to a relatively large amplitude oscillatory state. As discussed in the introduction, the rich dynamic behavior of these nonlinear devices can be leveraged in a variety of applications (i.e. mass sensing, single frequency bandpass

filtering, inertial sensing, and scanning probe microscopy) for improved performance over the conventional linear approaches. In many applications (i.e. single frequency bandpass filtering [104]), tuning the linear and nonlinear system parameters to achieve the desired frequency response characteristics will be necessary [4, 147, 104]. In this work, two devices are designed, fabricated, and tested in order to demonstrate the some of these useful tuning concepts.

In Section 2.1 the governing equation of a tunable parametrically excited MEM oscillator with linear and nonlinear time varying stiffness terms, commonly referred to as a Nonlinear Mathieu Equation, is described. The addition of the nonlinear time varying stiffness term included here and in [148, 105] results in interesting dynamics, which differ from those of Mathieu oscillators containing only linear time varying stiffness terms [154]. In Section 2.2 the linear tuning scheme is reviewed, the design for two MEM devices is discussed, and finally experimental results obtained for each device are presented and discussed. Section 2.3 has the same structure as Section 2.2 but for the case of nonlinear tuning.

2.1 Mathematical Model

The oscillators studied here consist of a backbone (M), noninterdigitated comb drives (A and B), and flexures (K). A standard silicon-on-insulator (SOI) process

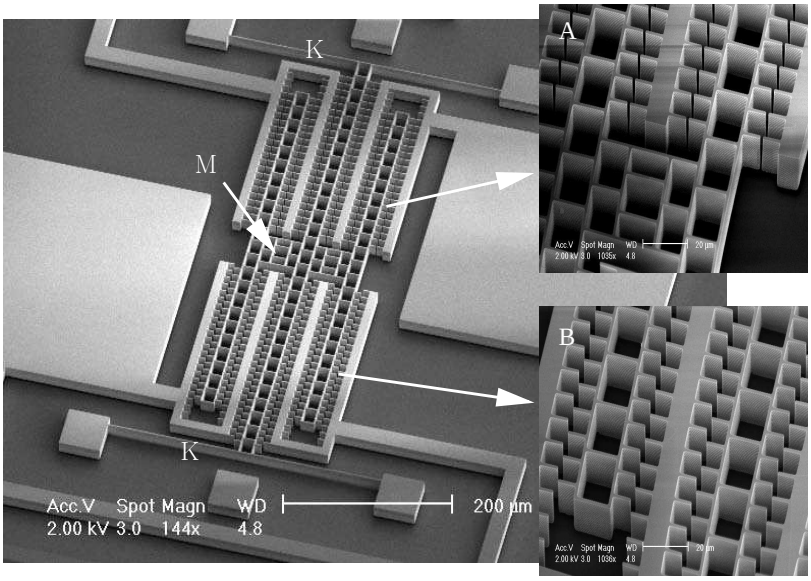

Figure 2.1: Scanning electron image of a parametrically excited MEM oscillator with noninterdigitated driving and tuning comb drives (A and B), Flexures (K), and Backbone (M).

flow (see [152]) is used to fabricate the representative device shown in Figure 2.1. This work utilizes two sets of noninterdigitated comb drives, one for actuation and one for tuning. In [4], the concept of using a set of DC noninterdigitated comb drives to tune an oscillator's effective linear and nonlinear stiffness coefficients is presented. Here oscillators are driven by applying an AC signal to a driving set of electrodes and tuned by a DC signal that is applied to a second set of electrodes. The tuning scheme used in this work has been analyzed theoretically in [104] and will be reviewed in sections to follow. The electrostatic force produced by these noninterdigitated drives, which has been previously studied and validated via numerical simulation, finite element analysis, and experimental investigation

[4, 148], is modeled as a cubic function of displacement [148]

$$F_{es}(x,t)= \left(r_{10}x + r_{30}x^3\right) V_0^2 + \left(r_{1A}x + r_{3A}x^3\right) V_A^2 \left(1 + \cos\omega t\right), \tag{2.1}$$

where r_{10} and r_{30} are, respectively, the linear and nonlinear electrostatic stiffness coefficients due to the DC excited electrodes, r_{1A} and r_{3A} are, respectively, the linear and nonlinear electrostatic stiffness coefficients due to the the AC excited electrodes, and V_0 and V_A are, respectively, the applied DC and AC signal amplitudes. It is important to note that the oscillator is driven with a square root cosine signal, giving rise to the AC forcing term in Equation (2.1), in order to demodulate harmonic and parametric excitation [134]. A restoring force is generated by the flexures,

$$F_r(x) = k_1 x + k_3 x^3, \tag{2.2}$$

where k_1 and k_3 are, respectively, the linear and cubic nonlinear stiffness coefficients. Note, k_3 arises due to boundary conditions that impart stress on the neutral axis of each flexure and that $k_3 > 0$ due to the natural hardening nature of the beams. Combining Equations (2.1) and (2.2) along with the force due to aerodynamic damping, gives the equation of motion [104]

$$\begin{aligned} m\ddot{x} + c\dot{x} + k_1 x + k_3 x^3 + \left(r_{10}x + r_{30}x^3\right) V_0^2 \\ + \left(r_{1A}x + r_{3A}x^3\right) V_A^2 \left(1 + \cos\omega t\right) = 0, \end{aligned} \tag{2.3}$$

where c is the damping coefficient and m is the oscillator's mass. For analytical purposes, see [104] and [105], the time in the equation of motion is rescaled according to

$$\tau = \omega_0 t, \tag{2.4}$$

where ω_0 is the pure elastic natural frequency

$$\omega_0 = \sqrt{\frac{k_1}{m}}, \tag{2.5}$$

and displacement is rescaled according to

$$\epsilon^{1/2} z = \frac{x}{x_0}, \tag{2.6}$$

where ϵ is a scaling parameter and x_0 is a characteristic length, e.g. the length of the oscillator backbone (note this is the scaling adopted in [104]). As in [105], displacement can also be scaled according to $z = x/x_0$ and the scaling parameter ϵ can be introduced by assuming that nondimensional damping, electrostatic forces, and mechanical nonlinearities are small. In either case, the rescaled equation of motion becomes

$$z'' + 2\epsilon\zeta z' + z\left[1 + \epsilon\nu_1 + \epsilon\lambda_1 \cos\left(\Omega\tau\right)\right] + \epsilon z^3\left[\chi + \nu_3 + \lambda_3 \cos\left(\Omega\tau\right)\right] = 0. \tag{2.7}$$

Table 2.1 describes each parameter and the derivative operator of (2.7); also see [105] and [104]. Equations (2.3) and (2.7) are generalizations of the Mathieu Equation, which are valid provided that the shuttle mass moves primarily in one

Table 2.1: Nondimensional parameter and operator descriptions for (2.7)

Parameters	*Descriptions*
$(\bullet)' = \frac{d(\bullet)}{d\tau}$	scaled time derivative
$\epsilon\zeta = \frac{c}{2m\omega_0}$	scaled damping ratio
$\epsilon\nu_1 = \frac{r_{10}V_0^2 + r_{1A}V_A^2}{k_1}$	linear electrostatic stiffness coefficient
$\epsilon\lambda_1 = \frac{r_{1A}V_A^2}{k_1}$	linear electrostatic excitation amplitude
$\Omega = \frac{\omega}{\omega_0}$	nondimensional excitation frequency
$\chi = \frac{x_0^2 k_3}{k_1}$	nonlinear mechanical stiffness coefficient
$\nu_3 = \frac{x_0^2\left(r_{30}V_0^2 + r_{3A}V_A^2\right)}{k_1}$	nonlinear electrostatic stiffness coefficient
$\lambda_3 = \frac{x_0^2 r_{3A}V_A^2}{k_1}$	nonlinear electrostatic excitation amplitude
$\gamma_3 = \chi + \nu_3$	combined nonlinear stiffness coefficient

direction (i.e. no other modes of oscillation affect the motion of the oscillator), that the aligned comb fingers remain approximately aligned and misaligned comb fingers remain approximately misaligned during oscillation, and the dominant source of damping in the system is due to viscous effects and is linear (dynamic model was previously studied and validated for a similar device in [148, 105, 36]).Note that both linear and nonlinear stiffness terms vary with time, whereas the conventional Mathieu Equation only contains linear time-varying stiffness terms, e.g. [154]. The presence of nonlinear parametric excitation leads to interesting dynamics, which have been accurately modeled in [105]. In this analysis, averaged equations were determined for (2.7) through a perturbation technique and steady-state solutions to these averaged equations were determined. By analyzing the stability of the trivial solution, a boundary for the primary parametric stability region can be determined; Figure 1.2 depicts a representative stability boundary. The nontrivial solutions to the averaged equations represent different branches of the system's response and ultimately allow for effective nonlinearities to be defined. In the end, the qualitative behavior of the system's response is determined by these effective nonlinearities. These analytical results are instrumental in the design portion of this work.

2.2 Linear Tuning

For applications such as filtering, having an amplitude dependent bandwidth (as in Figure 1.2) is undesirable. As a result, a method for tuning this wedge shaped region has been developed [104] and is briefly reviewed here. Specifically, the system's natural frequency is forced to depend on the excitation voltage amplitude, V_A. This is accomplished by applying a DC voltage V_0, which is proportional to the AC voltage amplitude (i.e., $V_0 = \alpha V_A$), to a second set of noninterdigitated comb drives. The linear and nonlinear stiffness coefficients are redefined as

$$\epsilon\nu_1 = \left(\frac{r_{10}\alpha^2 + r_{1A}}{k_1}\right) V_A^2, \tag{2.8}$$

$$\nu_3 = \left[\frac{x_0^2\left(r_{30}\alpha^2 + r_{3A}\right)}{k_1}\right] V_A^2, \tag{2.9}$$

respectively. Next, a tuning parameter is introduced,

$$\rho = \frac{\nu_1}{\lambda_1} = 1 + \frac{r_{10}\alpha^2}{r_{1A}}. \tag{2.10}$$

Linearizing about the no motion state and rewriting in the form, $z'' + \omega_n^2 z = -\epsilon f\left(z, z', t\right)$, Equation (2.7) becomes,

$$z'' + \left(1 + \epsilon\lambda_1\rho\right) z = -\epsilon\left[2\zeta z' + z\lambda_1\cos\left(\Omega\tau\right)\right]. \tag{2.11}$$

The oscillator's nondimensional time independent natural frequency now depends on excitation amplitude

$$\omega_n = \sqrt{1 + \epsilon\rho\lambda_1} = \sqrt{1 + \epsilon\nu_1}. \tag{2.12}$$

With the introduction of the new parameter ρ comes the ability to tune the system's instability region. Specifically, as V_A changes, therefore changing λ_1, the natural frequency changes. As a result, by choosing the correct magnitude and sign for ρ and sign for r_{1A} the instability region in Figure 1.2 can be rotated clockwise or counter clockwise to a specific location [104]. For filtering applications tuning the wedge shaped region to have a vertical, frequency independent, boundary is desirable. Perturbation analysis used in [104] shows that by choosing $\rho = 1/2$ for $r_{1A} > 0$ (or $\rho = -1/2$ for $r_{1A} < 0$), the left boundary of the instability zone is rotated to the vertical position. Likewise, the right boundary can be tuned to the vertical position by choosing $\rho = -1/2$ for $r_{1A} > 0$ (or $\rho = 1/2$ for $r_{1A} < 0$). As detailed in [104], the implementation of two tuned oscillators (one with $\rho = 1/2$ and another with $\rho = -1/2$) in a single system can render a highly effective single frequency bandpass filter.

2.2.1 Designing Linear Tunable Oscillators

Noninterdigitated comb drives and flexures can be designed to achieve specific linear tuning characteristics. The main concern for designers, however, is the geometry of the comb drives because the linear mechanical stiffness k_1 only changes in magnitude for different flexure designs. The geometric factors affecting electrostatics between comb fingers are spacing, gap, length, width, and alignment

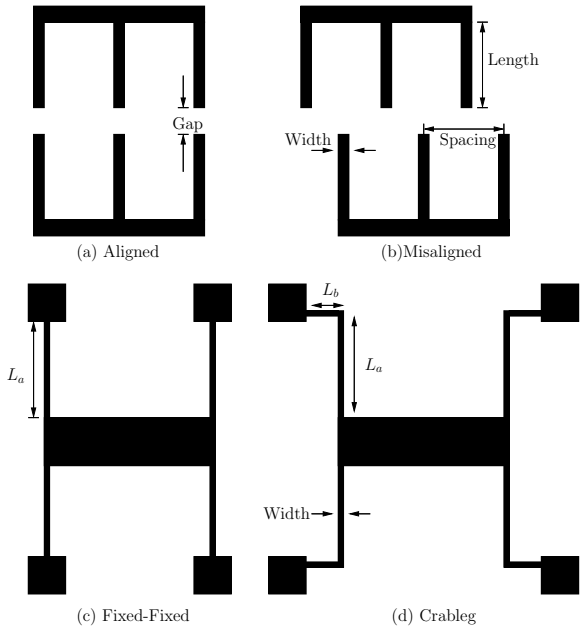

Figure 2.2: Noninterdigitated comb finger and flexure geometries.

(depicted in Figure 2.2 (a) and (b)). For details on how comb finger geometry affects the electrostatic coefficients refer to [4]. For design purposes, the multi-physics environment in ANSYS [**?**] is used to determine the force-displacement relationship for different comb drive geometries.

To achieve rotation of the instability regime in a desired direction, Equation (2.10) is considered. Specifically, the coefficients r_{10} and r_{1A} must be of opposite sign to rotate the wedge and achieve verticality of either boundary, which is of interest here. Of course the ratio can be chosen to be positive, however, then vertical boundaries cannot be achieved. If $r_{1A} > 0$ then the instability zone bends off to the right and the introduction of a negative r_{10} effectively rotates the wedge

counterclockwise. On the other hand, for $r_{1A} < 0$ a positive r_{10} rotates the wedge clockwise. In either case the magnitude of α dictates how far the wedge rotates and whether the right or left boundary of the wedge is vertical.

Here, two oscillators have been designed, both having a comb finger width of 1.5 μm, comb finger gap of 1 μm, comb finger spacing of 10 μm, and comb finger length of 8 μm (Table 2.2). It turns out that aligned comb fingers (Figure 2.2(a)) having this geometry exhibit a positive linear electrostatic stiffness, and misaligned comb fingers (Figure 2.2(b)) exhibit a negative linear electrostatic stiffness. Therefore by designing one pair of comb drives to be aligned and one pair of comb drives to be misaligned, the oscillators' parametric regions of instability can be tuned with the scheme presented in [104] (reviewed above). The two oscillator designs are discussed in Table 2.2. It is important to note that Device 1 has 160 aligned comb fingers, 164 misaligned comb fingers, and an effective mass of approximately $5.95 \times 10^{-10} kg$, while Device 2 has 128 aligned comb fingers, 130 misaligned comb fingers, and an effective mass of approximately $4.89 \times 10^{-10}\ kg$. The force-displacement relationships, determined from Finite Element Analysis, for each design's aligned and misaligned comb drives are shown in Figures 2.3 and 2.4, respectively.

For Device 1 the linear electrostatic stiffness coefficient, r_{1A}, is positive, so that the wedge shaped instability region bends off toward the right. For proof

Table 2.2: Oscillator Design Descriptions and Coefficients (See Figure 2.2 for labeled geometries)

Geometry Common to Both Designs		
	Geometry	
All Comb drives	$Width = 1.5\,\mu m$ $Gap = 1\,\mu m$ $Spacing = 10\,\mu m$ $Length = 8\,\mu m$	
Device 1		
	Geometry	Coefficients
AC Comb drives	*aligned* *160 Fingers*	$r_{1A} = 5.3 \times 10^{-3}\ \frac{\mu N}{\mu m V^2}$ $r_{3A} = -1.5 \times 10^{-3}\ \frac{\mu N}{\mu m^3 V^2}$
DC Comb drives	*misaligned* *164 Fingers*	$r_{10} = -9.7 \times 10^{-4}\ \frac{\mu N}{\mu m V^2}$ $r_{30} = -1.8 \times 10^{-5}\ \frac{\mu N}{\mu m^3 V^2}$
Flexures	*crableg* $L_a = 200\,\mu m$ $L_b = 20\,\mu m$ $Width = 1.5\,\mu m$	$k_1 = 5.36\ \frac{\mu N}{\mu m}$ $k_3 = 0.032\ \frac{\mu N}{\mu m^3}$
Effective Mass		$m = 5.95 \times 10^{-10}\,kg$
Device 2		
	Geometry	Coefficients
AC Comb drives	*misaligned* *130 Fingers*	$r_{1A} = -7.7 \times 10^{-4}\ \frac{\mu N}{\mu m V^2}$ $r_{3A} = -1.4 \times 10^{-5}\ \frac{\mu N}{\mu m^3 V^2}$
DC Comb drives	*aligned* *128 Fingers*	$r_{10} = 4.3 \times 10^{-3}\ \frac{\mu N}{\mu m V^2}$ $r_{30} = -1.2 \times 10^{-3}\ \frac{\mu N}{\mu m^3 V^2}$
Flexures	*fixed-fixed* $L_a = 160\,\mu m$ $Width = 1.5\,\mu m$	$k_1 = 11.21\ \frac{\mu N}{\mu m}$ $k_3 = 15.16\ \frac{\mu N}{\mu m^3}$
Effective Mass		$m = 4.89 \times 10^{-10}\,kg$

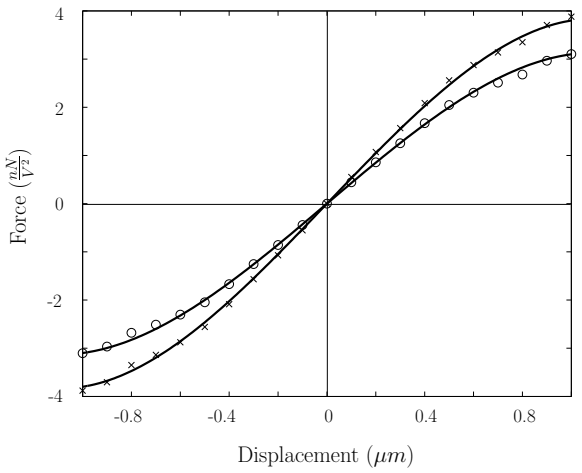

Figure 2.3: Aligned comb drive force-displacement relationship determined using ANSYS [**?**] for Device 1 (x's) and Device 2 (o's). The polynomials are fit to this data to determine linear and cubic nonlinear stiffness coefficients (solid curves).

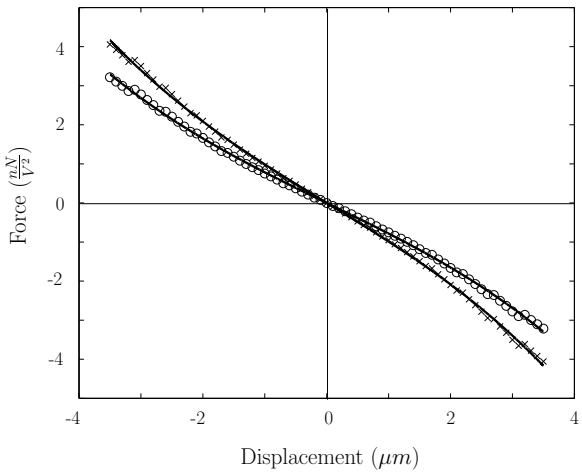

Figure 2.4: Misaligned comb drive force-displacement relationship determined using ANSYS [**?**] for Device 1 (x's) and Device 2 (o's). The polynomials are fit to this data to determine linear and cubic nonlinear stiffness coefficients, (solid curves).

of concept of the theory presented in [104], the right instability boundary of this device was chosen to be made vertical. Since $r_{1A} > 0$, the tuning parameter should be $\rho = -1/2$ and the applied DC and AC voltages should be related by the proportionality constant $\alpha = 2.86$ from Equation (2.10). Device 2, on the other hand, has $r_{1A} < 0$, so that the wedge bends off toward the left. In this case the goal was to rotate the left stability boundary to the vertical position, so $\rho = -1/2$ should be chosen and the DC and AC voltages should be related by $\alpha = 0.52$.

Flexure designs are discussed in the nonlinear tuning design section of this paper because the magnitude of the linear mechanical stiffness does not strongly affect the linear electrostatic tuning of the instability region. It is important, however, to point out that Device 1 and Device 2 have different flexure configurations (crableg and fixed-fixed respectively), different flexure lengths, and different effective masses, so each has a different resonant frequency. Figure 2.1 shows a scanning electron image of Device 2 with fixed-fixed flexures.

2.2.2 Experimental Results

Parametrically excited MEM oscillators have successfully been tuned by applying a DC voltage to a second set of noninterdigitated comb fingers, which is proportional to the AC excitation voltage applied to the other set of comb fingers.

To test the dynamics of these devices, a single point laser vibrometer was used [132]. Taking the α values calculated in Section 2.2.1, which theoretically tune one stability boundary for each device to be vertical, as starting points in experiment, the parametric stability regions are manipulated until the correct rotation is achieved. As expected, by driving Device 1 with the aligned set of comb drives, the untuned wedge bends off to the right (shown in Figure 2.5(a)). This confirms finite element simulations, which predict that an aligned set of comb fingers, with the geometry discussed in Section 2.2.1, has a positive linear electrostatic stiffness coefficient. By applying DC voltages proportional to the AC excitation voltages, specifically $\alpha = 1.66$, the wedge shaped region has been rotated counterclockwise, roughly to the vertical position. Since a counterclockwise rotation was achieved the linear electrostatic stiffness coefficient for this set must be negative, again confirming finite element results.

In the case of Device 2, results shown in Figure 2.5(b), the region of instability bends left in the untuned case when driving the device with misaligned comb fingers. By tuning with the aligned comb fingers, the parametric stability region rotates clockwise. Tuning with a proportionality constant $\alpha = 0.42$, the left boundary has been tuned roughly to the vertical position. Again the misaligned comb fingers exhibit a negative linear electrostatic stiffness, while aligned comb

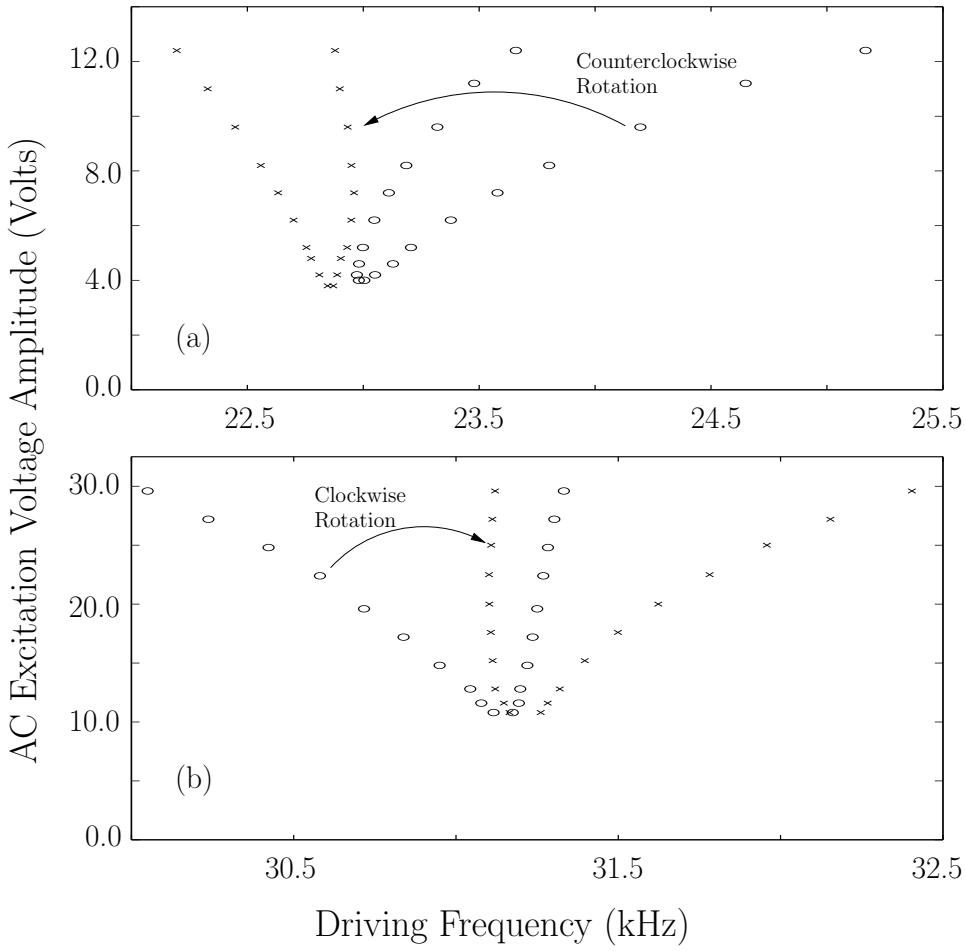

Figure 2.5: Experimental untuned (o's) and tuned (x's) instability zones for (a) Device 1 and (b) Device 2. An AC signal is applied solely to the driving set of comb fingers for the untuned wedges and both DC and AC signals are applied to the respective comb drives for the tuned wedges. Tuning coefficients for each case are: (a) $\alpha = 1.66$, (b) $\alpha = 0.42$.

fingers exhibit a positive linear electrostatic stiffness for the geometry presented in Section 2.2.1.

In both cases, the linear electrostatic stiffness for the driving and tuning sets of comb fingers are of opposite sign, therefore allowing an α to be chosen which rotates the right (Device 1) or left (Device 2) stability boundary roughly to the vertical position. Experimental α values for Device 1 and Device 2 both compare well with theoretically obtained α values, especially considering the amount of uncertainty in the dimensions of the fabricated devices. These results prove the concepts proposed in [4] and [104]. Since proof of concept is the main goal here, a system identification procedure has not been performed. If system parameters needed identification, however, methods similar to those discussed in [36] can be adopted. Also, it is important to note that more testing and finer tuning of α can yield better verticality if desired for specific applications, i.e. filtering, where a frequency independent boundary is desired.

2.3 Nonlinear Tuning

Due to the presence of nonlinearities in its equation of motion, this type of tunable oscillator can exhibit oscillatory motion outside the stability region and hysteresis. In [105] the qualitative nature of the system's nonlinear response is

characterized analytically. To accomplish this, a standard perturbation analysis, averaging, was employed. After using a standard coordinate transformation, and introducing a detuning parameter, $\sigma = (\Omega - 2)/\epsilon$, the averaged equations become

$$a' = \frac{1}{8} a\epsilon \left[-8\zeta + \left(2\lambda_1 + a^2 \lambda_3 \right) \sin\left(2\psi \right) \right] + O\left(\epsilon^2 \right), \tag{2.13}$$

$$\psi' = \frac{1}{8} \epsilon [3a^2 \left(\chi + \nu_3 \right) + 4\lambda_1 \rho - 4\sigma + 2 \left(\lambda_1 + a^3 \lambda_3 \right) \cos\left(2\psi \right)] + O\left(\epsilon^2 \right), \tag{2.14}$$

where a is the amplitude and ψ is the phase of oscillators' response. Assuming zero damping and solving for the steady state responses of the averaged equations it was found that there is one trivial and three nontrivial solutions. The trivial solution corresponds to the no motion state of the system and the first two nontrivial solutions correspond to branches of periodic orbits originating from the no motion state with amplitudes

$$\bar{a}_{1,2} = \sqrt{\frac{4\sigma - 2\lambda_1 \left(2\rho - 1 \right)}{3 \left(\chi + \nu_3 \right) - 2\lambda_3}}, \ \sqrt{\frac{4\sigma - 2\lambda_1 \left(2\rho + 1 \right)}{3 \left(\chi + \nu_3 \right) + 2\lambda_3}}. \tag{2.15}$$

Depending on the sign and magnitude of each linear and nonlinear electrostatic stiffness coefficient and the magnitude of the AC excitation voltage V_A, these two branches can independently bend toward each other, away from each other, or in the same direction. As a result, the system's response can exhibit hardening, softening, or mixed hardening and softening effective nonlinearities. The third nontrivial solution describes a constant amplitude branch

$$\bar{a}_3 = \sqrt{\frac{-2\lambda_1}{\lambda_3}}, \tag{2.16}$$

which only exists when $\lambda_1/\lambda_3 < 0$. Effective nonlinearities for the system are defined by examining the denominator in Equation (2.15)

$$\eta_1 = 3\left(\chi + \nu_3\right) - 2\lambda_3, \tag{2.17}$$

$$\eta_2 = 3\left(\chi + \nu_3\right) + 2\lambda_3, \tag{2.18}$$

where $\gamma_3 = \chi + \nu_3$ is the combined stiffness coefficient, subsequently designated in Table 2.1. In [105], by analyzing the three nontrivial steady state solutions and effective nonlinearities, it was found that the nonlinear parameter space (γ_3 versus λ_3) can be split into six different regions, where the responses within each region have a distinct qualitative behavior. The six different regions of parameter space and the corresponding responses are described in [105].

2.3.1 Designing Nonlinear Tunable Oscillators

The two oscillators discussed in Section 2.2.1 were also designed to exhibit certain nonlinear behavior. Specifically, Device 1 was designed to have a softening qualitative nonlinearity and Device 2 was designed to have a hardening qualitative nonlinearity. In other words, the non-hysteretic side of each response originates from the vertically tuned side of the instability zones. Typical responses showing the hysteresis characteristic to this class of parametric oscillator can be seen in the experimental section, which follows. For switching applications tuning this

nontrivial side of the response to occur away from the tuned, frequency independent stability boundary is desirable [104]. During the design process, the effective nonlinearities, η_1 and η_2, for the system are used to help achieve the correct nonlinear behavior for Devices 1 and 2. In physical terms the effective nonlinearities are

$$\eta_1 = \frac{3x_0^2}{k_1}\left[k_3 + \left(r_{30}\alpha^2 + \frac{1}{3}r_{3A}\right)V_A^2\right], \tag{2.19}$$

$$\eta_2 = \frac{3x_0^2}{k_1}\left[k_3 + \left(r_{30}\alpha^2 + \frac{5}{3}r_{3A}\right)V_A^2\right]. \tag{2.20}$$

In order to obtain a softening effective nonlinearity for Device 1, η_1 and η_2 must both be negative; and to obtain a hardening effective nonlinearity for Device 2, η_1 and η_2 must both be positive, as found in [105]. First considering Device 1, by designing the driving set of comb fingers such that r_{3A} is large in magnitude and negative and the tuning set such that $r_{30}\alpha^2 + 1/3r_{3A} < 0$, the driving voltage V_A can be tuned so that the naturally positive nonlinear mechanical stiffness k_3 is overcome and both effective nonlinearities are negative. The critical voltage for softening can be lowered if k_3 is designed to be small. For a fixed-fixed beam the stress on the neutral axis is relatively large due to the boundary conditions, therefore leading to a large cubic nonlinear mechanical stiffness. By creating small folds in the beams (commonly referred to as crableg beams), the cubic nonlinear mechanical stiffness can be mitigated by several orders of magnitude.

For a comparison of crableg and fixed-fixed flexures see [148]. To help achieve softening behavior for Device 1, crableg beams are used with $L_a = 200\,\mu m$, $L_b = 20\,\mu m$, and $width = 1.5\,\mu m$ (see Figure 2.2(d) for labeling and Table 2.2 for calculated stiffness values). Note that fold lengths L_b are made small enough to ensure that unwanted torsional and out of plane modes occur at much larger frequencies than the primary parametric resonant frequency, but long enough to provide ample stress relief and decrease k_3 significantly.

To aid in the design process ANSYS [**?**] simulations were used, ultimately helping to understand how comb drive and flexure geometries affect the respective nonlinear coefficients. Through these simulations the electrostatic and mechanical nonlinearities were determined for each device, as shown in Table 2.2. The theoretical parameters for Device 1 yield an effective nonlinearity which transitions from a hardening to a mixed then to a softening response as AC excitation voltage is increased both when the oscillator is tuned and untuned, as shown in Figure 2.6.

So, as AC voltage is increased the response of the tuned oscillator starts off hardening (region VI) transitions to a mixed softening and hardening response at $3.5\,V$ (regions Va and Vb) and finally transitions to a softening response at $7.1\,V$. Theoretically Device 1 should exhibit a softening response for AC voltages above $7.1\,V$ when tuned by a DC voltage, which is related to the AC voltage by

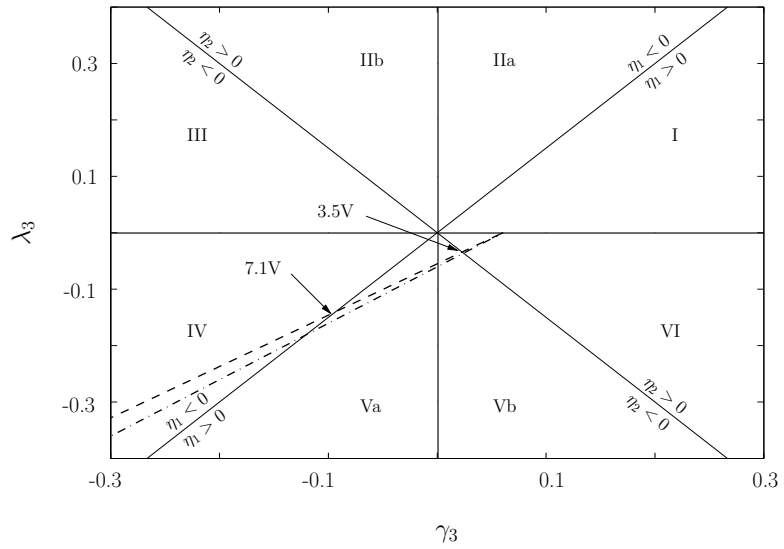

Figure 2.6: Nonlinear parameter space showing the transition of Device 1's response as AC excitation voltage V_A is varied, with tuned oscillator represented by dashed line and untuned oscillator by dash-dotted line.

$\alpha = 2.86$. Also from Figure 2.6, when the DC tuning electrodes are activated, the line cutting through this parameter space rotates clockwise since r_{30} is negative. Having a negative r_{30} is desirable when designing a device to have a softening response because it effectively lowers the critical voltage to achieve two negative effective nonlinearities.

Next, considering Device 2, note that the effective nonlinearities η_1 and η_2 can be both made positive in several ways. First of all, the geometry of the comb fingers can be designed so that r_{3A} and r_{30} are both positive, in which case η_1 and η_2 will also be positive because k_3 is always positive. Second, either one or both of r_{3A} and r_{30} could be designed to be negative and k_3 large enough so that both

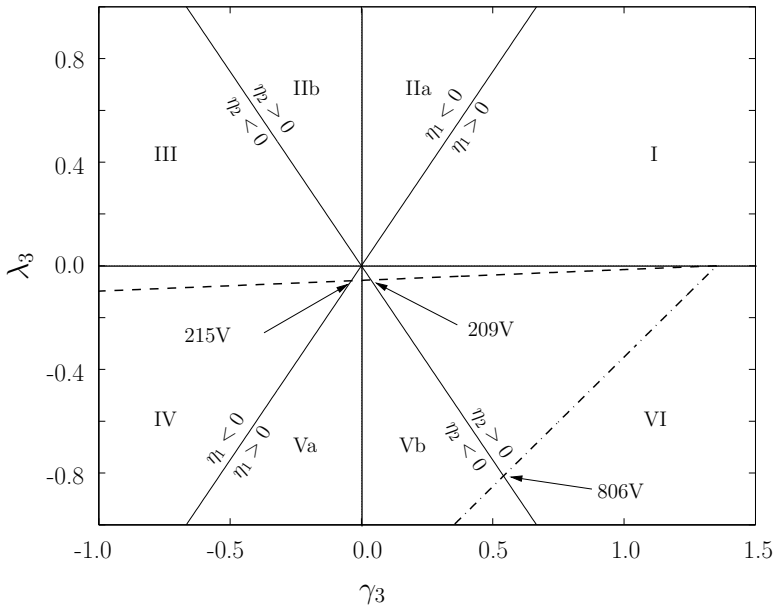

Figure 2.7: Nonlinear parameter space showing the transition of Device 2's response as AC excitation voltage V_A is varied, with tuned oscillator represented by dashed line and untuned oscillator by dash-dotted line.

effective nonlinearities are positive for a large range of AC excitation voltages. For this study the latter is chosen, where both nonlinear electrostatic coefficients are negative. In this case, the flexure design becomes important because hardening behavior is desired for a wide range of applied AC voltage. To achieve this, fixed-fixed beams were implemented (each with a length $L_a = 160\,\mu m$, which leads to the calculated stiffness values shown in Table 2.2) which yield a cubic nonlinear stiffness that is several orders of magnitude larger than crableg beams. The resulting parameters for this design yield effective nonlinearities that transition through $\gamma_3 - \lambda_3$ parameter space as a function of applied voltage as shown in

Figure 2.7. The system's response, when tuned, should remain hardening until an AC voltage of $209\,V$ is reached (using $\alpha = 0.52$). Since the nonlinear electrostatic coefficient for the tuning electrodes is relatively large and negative, the untuned oscillator will remain in the hardening response regime for a much wider range of excitation voltage than the tuned oscillator, specifically $806\,V$, a range well beyond the physical limits of the oscillator. Specifically, the oscillator will fail as a result of breakdown well before the $806\,V$ is reached. Again this negative nonlinear tuning coefficient effectively rotates the oscillator's path through this parameter space clockwise.

2.3.2 Experimental Results

Using the aforementioned analytical techniques, Devices 1 and 2 have successfully been developed to exhibit pure softening and pure hardening nonlinearities, respectively, for a wide range of excitation voltages. Figure 2.8(a) shows a softening response for Device 1 when a $5.20\,V$ AC signal is applied to the aligned set of driving comb fingers and no DC tuning voltage is applied to the misaligned comb fingers. It is important to note that the experimental transition voltages presented in this section are slightly different than the theoretical transition voltages above because imperfections in the fabricated devices cause the actual parameters to differ slightly from those predicted assuming no structural imperfections.

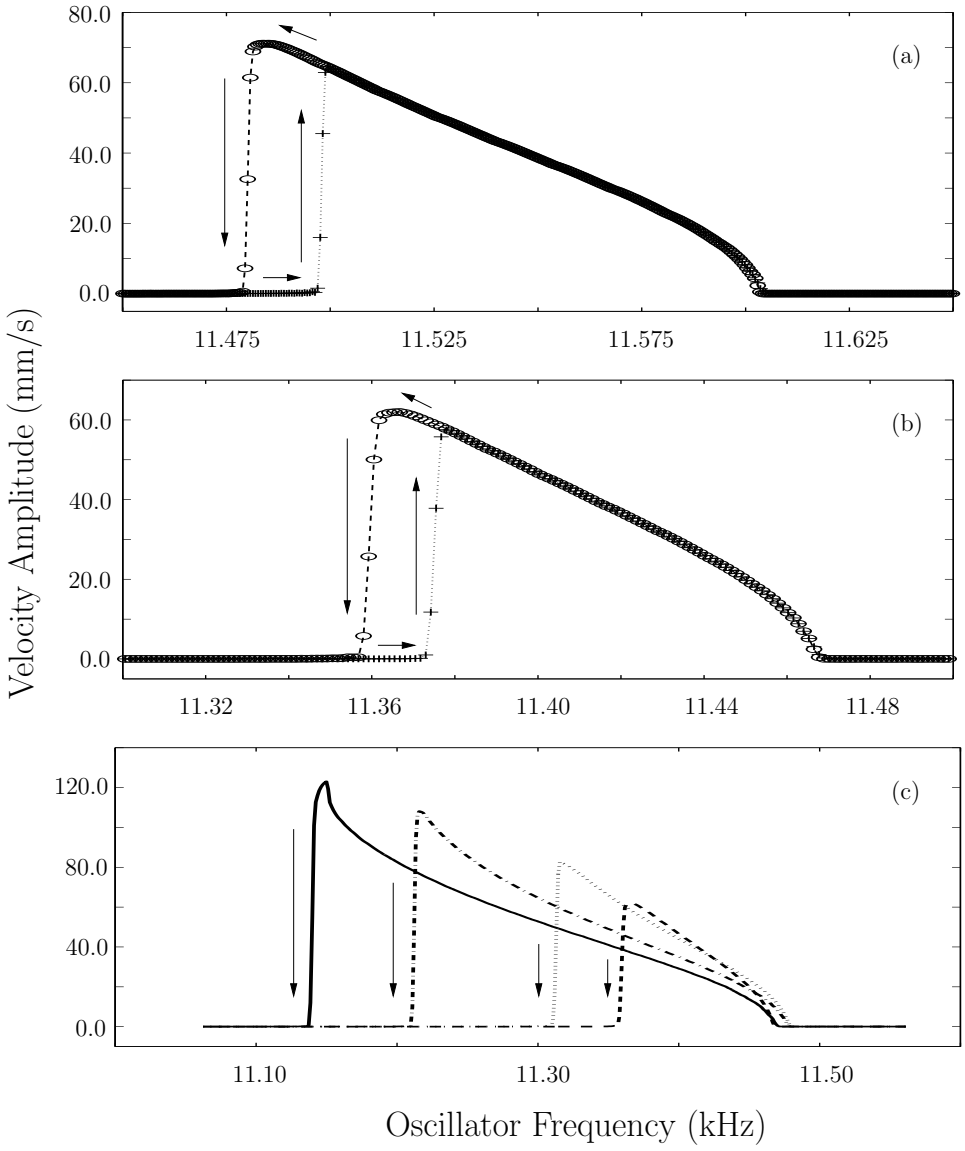

Figure 2.8: Softening Responses for Device 1 (a) untuned with $5.20\,V$ AC excitation, (b) tuned with $5.20\,V$ AC excitation and $8.63\,V$ DC tuning, and (c) tuned, $\alpha = 1.66$, with various AC excitation voltages (sweeping down in frequency): $dashed = 5.20\,V$ AC, $dotted = 6.20\,V$ AC, $dash - dotted = 8.20\,V$ AC, and $solid = 9.20\,V$ AC.

Adding a DC voltage of $8.63\,V$ to the misaligned set of comb fingers, the response is shifted to the right, but remains softening as seen in Figure 2.8(b). In both cases, the hysteresis is found on the left side of the response, indicating that both effective nonlinearities, η_1 and η_2, are negative. Keeping the AC and DC voltages proportional, specifically $\alpha = 1.66$, effectively rotated the instability region counterclockwise as seen in Figure 2.5(a); Figure 2.8(c) depicts experimental responses, obtained by sweeping down in frequency, that originate from the right boundary of this wedge. Notice that the right side of the responses originate very close to one another, therefore indicating that the linear tuning scheme has succeeded in rotating the right stability boundary roughly to the vertical position. Likewise, the nonlinear tuning scheme has successfully produced responses where the non-hysteretic region lives on the tuned boundary. Also important to note is the fact that the softening has been achieved for considerably low excitation voltages, as low as $4.2\,V$, in both tuned and untuned cases.

Figure 2.9(a) shows the untuned hardening response for Device 2 when a $10.80\,V$ AC signal is applied to the misaligned set of comb fingers. As expected, including fixed-fixed beams to the design has shifted the system's effective nonlinearity to the right in nonlinear parameter space, therefore substantially increasing the voltage range where hardening occurs. After applying a DC voltage of $4.52\,V$ to the aligned fingers, the response, as shown in Figure 2.9(b), remains hardening.

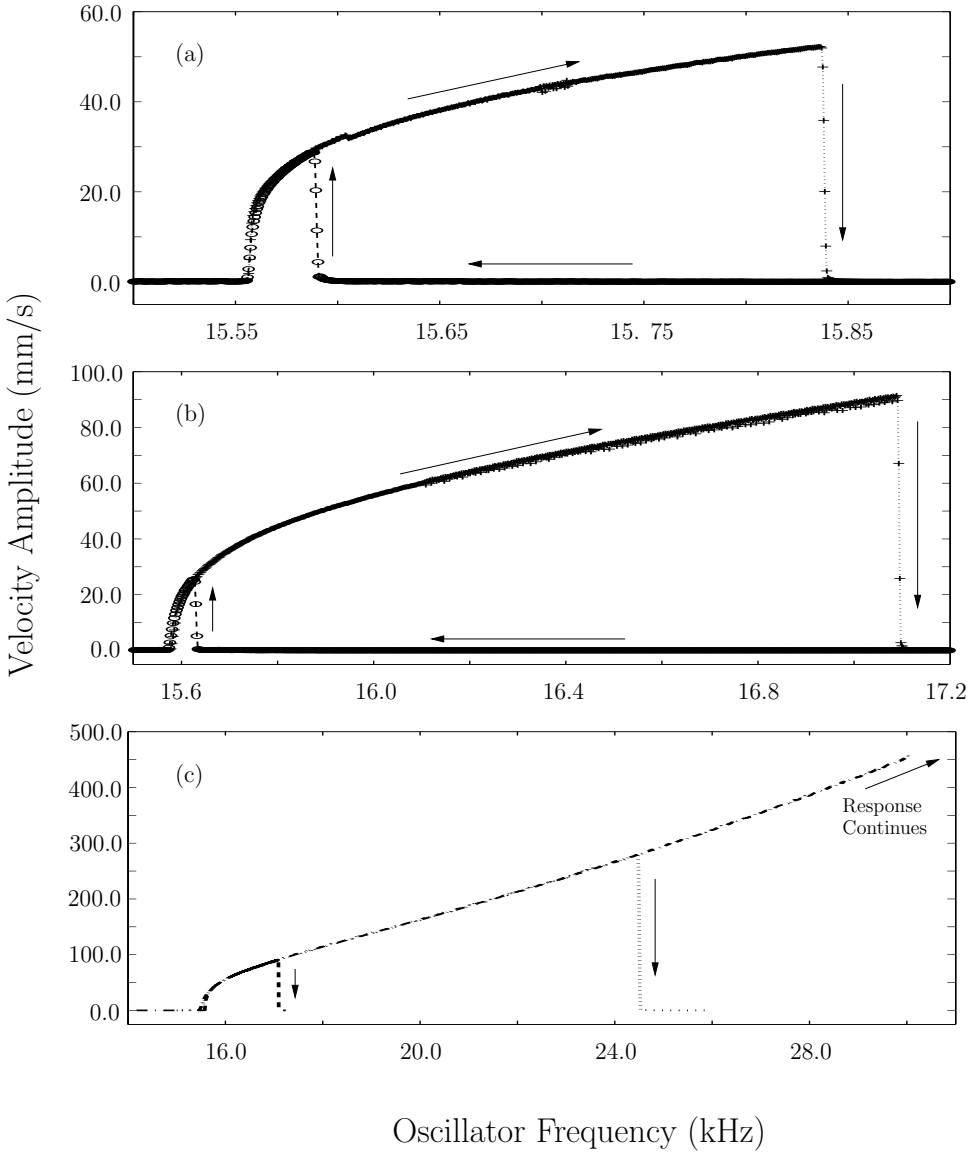

Figure 2.9: Hardening Responses for Device 2 (a) untuned with $10.80\,V$ AC excitation, (b) tuned with $10.80\,V$ AC excitation and $4.52\,V$ DC tuning, and (c) tuned, $\alpha = 0.42$, with various AC excitation voltages (sweeping up in frequency): $dashed = 10.8\,V$ AC, $dotted = 12.8\,V$ AC, and $dash - dotted = 15.2\,V$ AC.

Note, the hysteresis living to the right side of the response extends over a very large band of frequency, indicating that the effective nonlinearities are both large in magnitude and positive. The large hysteresis range can be attributed to the fact that fixed-fixed beams are used, which increase the nonlinear mechanical stiffness by several orders of magnitude when compared to the crableg beams used in Device 1. Figure 2.9(c) depicts three tuned responses for different excitation voltages when sweeping up in frequency, which all have the right side of the response originating very close to each other. This indicates that by tuning the oscillator's instability region with $\alpha = 0.42$, the onset of instability occurs roughly at the same frequency for a range of excitation voltages.

Chapter 3

Chaos for a Microelectromechanical Oscillator

In this chapter the existence of chaos is investigated for the nonlinear parametrically excited MEM oscillator discussed in the introduction and in the previous chapter. In order for these oscillators to be utilized in real-world applications, it is important to have knowledge of the conditions (system parameters) that cause chaotic behavior to occur. Prediction of such behavior is important both for creating devices that exploit chaotic vibrations for applications such as signal encryption [141] and for creating robust devices with predictable dynamic behavior (i.e. for mass sensing [148] and signal filtering [104]).

As discussed in the introduction, chaos has been discovered and reported for many physical systems. A classical example of a chaotic system is the Lorenz equations [76], which were derived to help understand the dynamics of cellular convection. Chaos due to various mechanisms has also been reported for nonlinear MEM oscillators, including AFM microcantilevers [14, 10, 9, 60, 64], an in-plane MEM oscillator with separated comb drive actuators for signal encryption applications [141], an electrostatically actuated MEM cantilever control system [75], and MEM oscillators based on variable gap capacitors [77, 34]. To the author's knowledge, the presence of chaos has not been thoroughly investigated for the tunable oscillators with time varying linear and nonlinear stiffness terms discussed in Chapter 2.

Here, Melnikov's method [52] is employed to define the regions of parameter space where homoclinic chaos can occur. Numerical analysis is used to study the system's behavior for various parameter sets and to verify the result from Melnikov's method. Finally, a description is given for a MEM oscillator which was designed and fabricated such that, for a range of applied voltages and driving frequencies, chaos is predicted to occur from Melnikov's method. The chaotic behavior of this device was demonstrated experimentally.

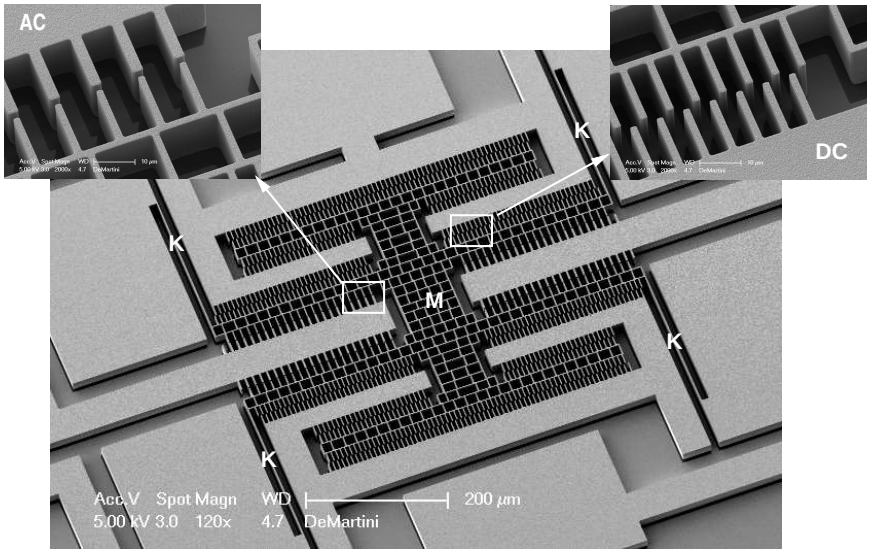

Figure 3.1: Scanning electron image of the MEM Oscillator consisting of a proof mass (M), mechanical flexures (K), a driving set of noninterdigitated comb fingers (AC), and a tuning set of noninterdigitated comb fingers (DC).

3.1 Mathematical Model

The layout of the oscillator studied in this chapter is shown in Figure 3.1, where M is the oscillator's backbone (or proof mass), AC and DC are noninterdigitated comb drive actuators, and K are flexures. To fabricate the device a standard silicon-on-insulator (SOI) process flow (see [152]) was used. A square root cosine voltage signal, $V(t) = V_A\sqrt{1+\cos(\omega t)}$, which decouples parametric and harmonic excitation [134], is applied to the AC actuators. For tuning purposes, a DC voltage V_0 is applied to the DC actuators. The electrostatic force generated by these actuators is described by Equation (2.1) from Section 2.1. A unique feature of this type of electrostatic actuator is that the stiffness coefficients (r_{10}, r_{30}, r_{1A},

and r_{3A}) can be positive or negative depending on the geometry and alignment of the comb fingers [4, 38]. The dimensions of these fingers will also strongly affect the magnitude and sign of these coefficients. The mechanical flexures provide a restoring force to the system described by Equation (2.2), which is modeled with a linear stiffness (k_1) and a cubic nonlinear stiffness (k_3). The equation of motion of this device is given by Equation (2.3), which is a nonlinear version of the Mathieu equation.

For analytical purposes, time in Equation (2.3) is rescaled as $\tau = \omega_0 t$, where $\omega_0 = \sqrt{k_1/m}$ is the system's pure elastic linear natural frequency, and displacement is rescaled as $z = x/x_0$, where x_0 is a characteristic length (say the center to center distance between comb fingers). The ratio of the driving frequency to the natural frequency is defined to be $\Omega = \omega/\omega_0$. Rearranging, the nondimensionalized equation of motion becomes

$$z'' + \alpha z' + \beta z + \delta z^3 + \gamma \left(1 + \cos \Omega\tau\right) z + \eta \left(1 + \cos \Omega\tau\right) z^3 = 0, \qquad (3.1)$$

where the new derivative operator and nondimensional parameters are defined in Table 3.1.

Table 3.1: Derivative operator and nondimensional parameter definitions.

$' = d/d\tau$	derivative operator
$\alpha = c/(\omega_0 m)$	damping coefficient
$\beta = 1 + r_{10}V_0^2/k_1$	tunable linear stiffness
$\delta = x_0^2(k_3 + r_{30}V_0^2)/k_1$	tunable nonlinear stiffness
$\gamma = r_{1A}V_A^2/k_1$	linear electrostatic stiffness coefficient
$\eta = x_0^2 r_{3A}V_A^2/k_1$	nonlinear electrostatic stiffness coefficient

3.2 Melnikov's Method and Chaos

Melnikov's method is an analytical technique which can be used to deduce the presence of chaos in a dynamical system.

Consider the general one degree of freedom system[52]

$$\dot{x} = f_0(x, y) + \epsilon g_0(x, y, t) = \frac{\partial H}{\partial y} + \epsilon g_0(x, y, t), \tag{3.2}$$

$$\dot{y} = f_1(x, y) + \epsilon g_1(x, y, t) = -\frac{\partial H}{\partial x} + \epsilon g_1(x, y, t), \tag{3.3}$$

where ϵ is a small parameter, g is periodic in t with period T, and H is a real Hamiltonian function. Suppose that for the unperturbed ($\epsilon = 0$) autonomous system, a saddle point with overlapping stable and unstable manifolds exists, corresponding to a homoclinic orbit (see Figure 3.2(a)). When a small perturbation is applied (i.e. $\epsilon \neq 0$), there will be a periodic orbit close to the saddle point, which will be a fixed point p of the Poincaré map defined by evolution for a time T (i.e., a point in phase space is recorded once every period T). Parts of the stable and unstable manifolds ($W^s(p)$ and $W^u(p)$ respectively) of p will remain

close to their counterparts for the saddle point for the unperturbed system over semi-infinite time intervals, but the homoclinic orbit will typically be broken, so that $W^s(p)$ and $W^u(p)$ no longer lie on top of one another (see Figure 3.2(b)). By Moser's theorem and the Smale Birkhoff homoclinic theorem, if the the stable and unstable manifolds intersect transversely then the system's dynamics will contain a horseshoe [142]. The existence of a horseshoe implies that there are a countable infinity of periodic orbits, that there are an uncountable number of aperiodic orbits, and that there is a dense orbit which comes arbitrarily close to every point in the invariant set of the horseshoe map. In other words, a chaotic set exists in the system when a transverse intersection of the manifolds occurs. We emphasize that this set is not necessarily an attractor.

The Melnikov function gives a measure of the leading order distance between the stable and unstable manifolds when $\epsilon \neq 0$ and can be used to tell when the stable and unstable manifolds intersect transversely. It is defined to be the integral

$$M(t_0) = \int_{-\infty}^{\infty} [f_0(x_0, y_0) g_1(x_0, y_0, t + t_0) - f_1(x_0, y_0) g_0(x_0, y_0, t + t_0)] dt, \quad (3.4)$$

where $q^0(t) = (x_0, y_0)$ is the solution corresponding to the unperturbed homoclinic trajectory. If $M(t_0) = 0$ and $M'(t_0) \neq 0$ for some t_0 and some set of parameters then the two manifolds have a transverse intersection, a horseshoe exists, and chaos occurs [52]. Melnikov's method can serve as a useful tool in the development

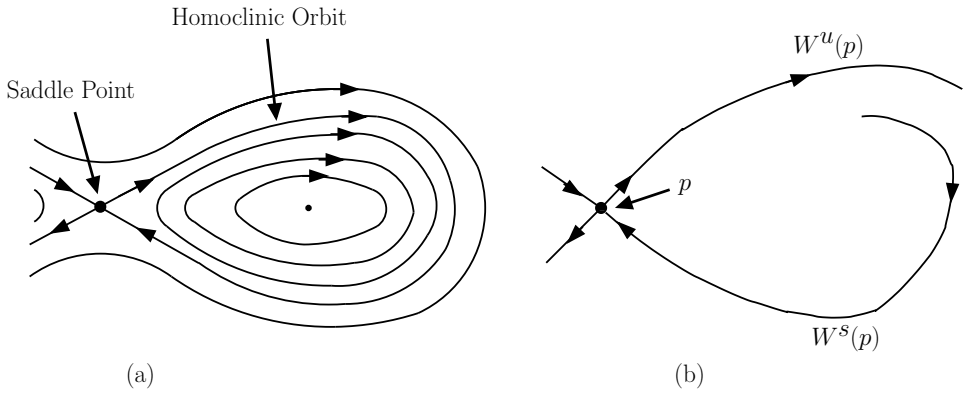

Figure 3.2: Illustrative diagrams showing (a) the phase space for the unperturbed system ($\epsilon = 0$) that contains a saddle point, homoclinic trajectories and periodic orbits and (b) the phase space for the Poincaré map when a perturbation ($\epsilon \neq 0$) is applied where the stable manifold $W^s(p)$ and unstable manifold $W^u(p)$ separate.

of nonlinear MEM oscillators, giving bounds on the parameters of a system where chaos, resulting from such intersections, can occur.

3.3 Chaos Prediction for a MEM Oscillator

3.3.1 Scaling and Conditions for Homoclinic Trajectories

In order to perform Melnikov analysis on Equation (3.1), some rescaling is performed. Specifically, Equation (3.1) needs to be rewritten to take the same form as Equations (3.2) and (3.3). Parameters corresponding to time dependent and velocity terms (i.e. forcing and damping) are assumed to be small:

$$\alpha \equiv \epsilon\tilde{\alpha} = \mathcal{O}(\epsilon), \quad \gamma \equiv \epsilon\tilde{\gamma} = \mathcal{O}(\epsilon), \quad \eta \equiv \epsilon\tilde{\eta} = \mathcal{O}(\epsilon), \tag{3.5}$$

which is a valid assumption for MEM oscillators. All other time independent terms are assumed to be order one quantities (i.e. $\beta = \mathcal{O}(1)$, $\delta = \mathcal{O}(1)$). Defining $z' = v$ and rewriting the second order differential equation as two first order differential equations gives the perturbed system

$$\begin{aligned} z' &= v, \\ v' &= -\beta z - \delta z^3 + \epsilon \left[-\tilde{\alpha} v - \tilde{\gamma} \left(1 + \cos\left(\Omega\tau\right)\right) z - \tilde{\eta} \left(1 + \cos\left(\Omega\tau\right)\right) z^3 \right]. \end{aligned} \tag{3.6}$$

For the unperturbed ($\epsilon = 0$) system, the following Hamiltonian is found:

$$H\left(z, v\right) = \frac{1}{2} v^2 + \frac{1}{2} \beta z^2 + \frac{1}{4} \delta z^4. \tag{3.7}$$

From this Hamiltonian, the following conditions are placed on parameters so that the Hamiltonian exhibits a double-well structure, and hence has a homoclinic trajectory:

$$\beta < 0, \quad \delta > 0. \tag{3.8}$$

The energy of the system can be visualized by plotting the potential energy portion of Equation (3.7), $U(z) = \beta z^2/2 + \delta z^4/4$, as a function of displacement z, shown in Figure 3.3(a). For $\beta = 0$ the potential energy is at a bifurcation point where it has not quite reached a double well state (dotted line in Figure 3.3(a)) and is a symmetric quartic curve. As V_0 is increased past the critical value $V_{0,crit}^{\beta}$, two wells (minima) are created which can be thought of as stable fixed points, and

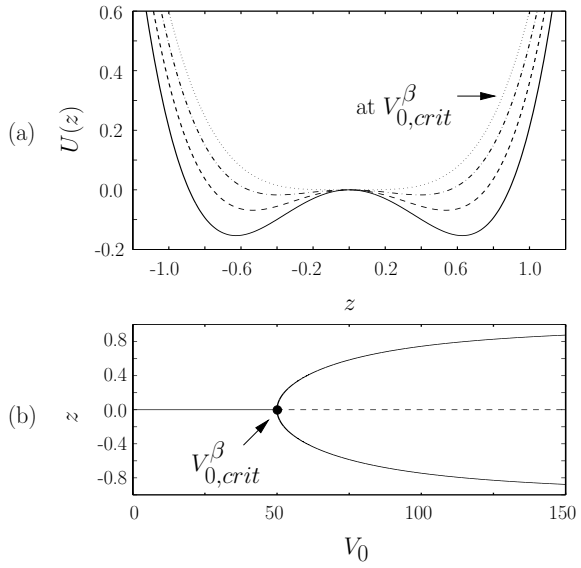

Figure 3.3: Representative figures for $\epsilon = 0$ and $\delta > 0$, showing (a) the potential energy, $U(z) = \frac{1}{2}\beta z^2 + \frac{1}{4}\delta z^4$ with $\beta \leq 0$, as a function of displacement z, illustrating the system's double-well structure (dotted curve represents $V_0 = V_{0,crit}^{\beta}$ and all other curves represent the case when $V_0 > V_{0,crit}^{\beta}$, where the solid curve represents the highest V_0) and (b) bifurcation diagram showing the position of each extremum as a function of V_0 (solid curves give stable solutions and dashed curves give unstable solutions).

the fixed point at the origin becomes unstable. By treating V_0 as a bifurcation parameter and plotting the position of each equilibrium point (the maxima and minimum of the potential energy), Figure 3.3(b) is generated, which is the well-known pitchfork bifurcation. In an experiment, small noise induced perturbations cause the device to leave the unstable origin and settle to one of the two stable positions when $V_0 > V_{0,crit}^{\beta}$. By only activating the DC comb drives and observing the device snap to a new equilibrium position, this behavior can be exploited to verify Conditions (3.8) prior to exploring the chaotic dynamics, as will be done below.

From (3.8), to obtain chaos the main obstacle that needs to be overcome in the design process is to create a net negative linear stiffness, $\beta < 0$. To overcome this seemingly unphysical condition, the DC comb fingers can be chosen to have a large negative linear stiffness, so that under reasonable V_0 the net stiffness, β, is negative. Various aspects of the comb finger and flexure design are discussed in the following subsection.

3.3.2 Design Considerations

In order to create a MEM oscillator satisfying (3.8), the DC tuning comb drives [4, 147, 38] and flexures must be designed accordingly. Since $\beta \sim k_1 + r_{10}V_0^2$ and k_1 is always positive, the tuning comb drives need to be configured so that

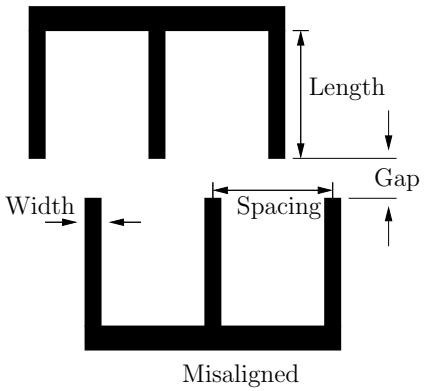

Figure 3.4: Geometry of misaligned noninterdigitated comb drives proposed for tuning the oscillator such that $\beta < 0$ and $\delta > 0$.

$r_{10} < 0$. This is achieved by making the comb fingers misaligned with respect to one another (see Figure 3.4). Furthermore, V_0 must be larger than the following critical voltage

$$V_{0,crit}^{\beta} = \sqrt{-k_1/r_{10}}, \tag{3.9}$$

to achieve $\beta < 0$. To decrease this critical voltage the oscillator can be designed with small k_1 and large r_{10}. Long, thin flexures can be used to reduce k_1.

The other critical coefficient is $\delta \sim k_3 + r_{30}V_0^2$. Since k_3 is always positive, r_{30} can either be positive or negative to satisfy $\delta > 0$. Although it is preferable to design $r_{30} > 0$ so that $\delta > 0$ for all V_0, if $r_{30} < 0$ one can still satisfy $\delta > 0$ by taking V_0 less than the critical voltage

$$V_{0,crit}^{\delta} = \sqrt{-k_3/r_{30}}. \tag{3.10}$$

In this case by designing k_3 large and r_{30} small, the upper bound $V^{\delta}_{0,crit}$ is increased. To increase the magnitude of k_3 fixed-fixed flexures, shown in Figure 3.1 as beams labeled K, can be used.

The magnitudes of r_{10} and r_{30} can be increased by increasing the number of comb fingers and changing their dimensions. One way to achieve this is by decreasing the gap between the comb fingers. Also, increasing the spacing between each finger will make r_{30} more positive. The effects of geometry on these parameters can be explored using finite element software and have been previously documented [4, 147, 38].

3.3.3 Applying Melnikov's Method

Satisfying the conditions for a double well potential gives rise to a homoclinic orbit in the system's phase space for $\epsilon = 0$. The homoclinic trajectory can be found by setting $H(z, v) = 0$. Solving for the resulting displacement and differentiating to determine velocity, the homoclinic trajectory is [52]:

$$z_0(\tau) = \pm\sqrt{2|\beta|/\delta}\,\mathrm{sech}\left(\sqrt{|\beta|}\tau\right), \tag{3.11}$$

$$v_0(\tau) = \mp|\beta|\sqrt{2/\delta}\,\mathrm{sech}\left(\sqrt{|\beta|}\tau\right)\tanh\left(\sqrt{|\beta|}\tau\right). \tag{3.12}$$

The Melnikov function (3.4) can now be evaluated, where $f_0(z,v) = v$, $g_0(z,v,\tau) = 0$, and

$$\begin{aligned} f_1(z,v) &= -\beta z - \delta z^3, \\ g_1(z,v,\tau) &= -\tilde{\alpha} v - \tilde{\gamma}\left(1+\cos\left(\Omega\tau\right)\right) z - \tilde{\eta}\left(1+\cos\left(\Omega\tau\right)\right) z^3. \end{aligned} \tag{3.13}$$

The integral becomes

$$\begin{aligned} M(\tau_0) = \int_{-\infty}^{\infty} v_0(\tau)[&-\tilde{\alpha} z_0'(\tau) - \tilde{\gamma}\left(1+\cos\left(\Omega(\tau+\tau_0)\right)\right) z_0(\tau) \\ &-\tilde{\eta}\left(1+\cos\left(\Omega(\tau+\tau_0)\right)\right)\left(z_0(\tau)\right)^3]d\tau, \end{aligned} \tag{3.14}$$

which yields

$$\begin{aligned} M(\tau_0) = \kappa[&\pi\Omega^2\left(6\delta\tilde{\gamma} + \tilde{\eta}\left(4\left|\beta\right| + \Omega^2\right)\right)\sin(\Omega\tau_0) \\ &+8\tilde{\alpha}\left|\beta\right|^{\frac{3}{2}}\delta\sinh\left(\pi\Omega/\left(2\sqrt{\left|\beta\right|}\right)\right)]. \end{aligned} \tag{3.15}$$

where $\kappa = -\mathrm{csch}(\pi\Omega/(2\sqrt{(|\beta|)})/(6\delta^2)$. In order for the unstable and stable manifolds to intersect, Melnikov's method states that $M(\tau_0) = 0$ for some τ_0. For this to hold, the following criterion must be met:

$$\begin{aligned} Y(\Omega) \equiv \ &\left|8\alpha\left|\beta\right|^{\frac{3}{2}}\delta\sinh\left(\pi\Omega/\left(2\sqrt{\left|\beta\right|}\right)\right)\right| \\ &-\left|\pi\Omega^2\left(6\delta\gamma + \eta\left(4\left|\beta\right| + \Omega^2\right)\right)\right| < 0. \end{aligned} \tag{3.16}$$

Consequently, an oscillator whose parameters satisfy this expression will have a chaotic invariant set, which may or may not be an attractor. It is important to note that a large region of parameter space will satisfy this inequality.

Table 3.2: Physical parameters of a representative device studied using numerical analysis.

k_1	$5\ \mu N/\mu m$
k_3	$7\ \mu N/\mu m^3$
m	$3 \times 10^{-10}\ kg$
c	$1.9 \times 10^{-8}\ kg/s$
r_{10}	$-2 \times 10^{-3}\ \mu N/(V^2 \mu m)$
r_{30}	$2 \times 10^{-3}\ \mu N/(V^2 \mu m^3)$
r_{1A}	$1 \times 10^{-3}\ \mu N/(V^2 \mu m)$
r_{3A}	$-4 \times 10^{-4}\ \mu N/(V^2 \mu m^3)$

3.3.4 Numerical Analysis of a Realistic MEM Oscillator

For the purposes of this analysis, realistic parameters are chosen based on an electrostatically driven Mathieu MEM oscillator presented in DeMartini *et al* [38]; these are shown in Table 3.2. (Note, these are not the exact parameters of that device, rather, they were chosen as representative values for a device that can be designed and manufactured.) This particular device is chosen for study because it satisfies the homoclinic trajectory criterion above, $\beta < 0$ and $\delta > 0$. Since $r_{30} > 0$, $\delta > 0$ will be true for all V_0, and $V_0 > V_{0,crit}^{\beta}$ will therefore be the critical condition in this analysis. It turns out that $V_{0,crit}^{\beta} = 50V$ for these parameters. In DeMartini *et al* [38], the second set of comb fingers, used to drive the oscillator, are aligned relative to one another giving rise to $r_{1A} > 0$ and $r_{3A} < 0$. The driving voltage V_A can be used to tune the parameters γ and η to satisfy Equation (3.16). It is important to note that choosing different comb finger arrangements for actuation,

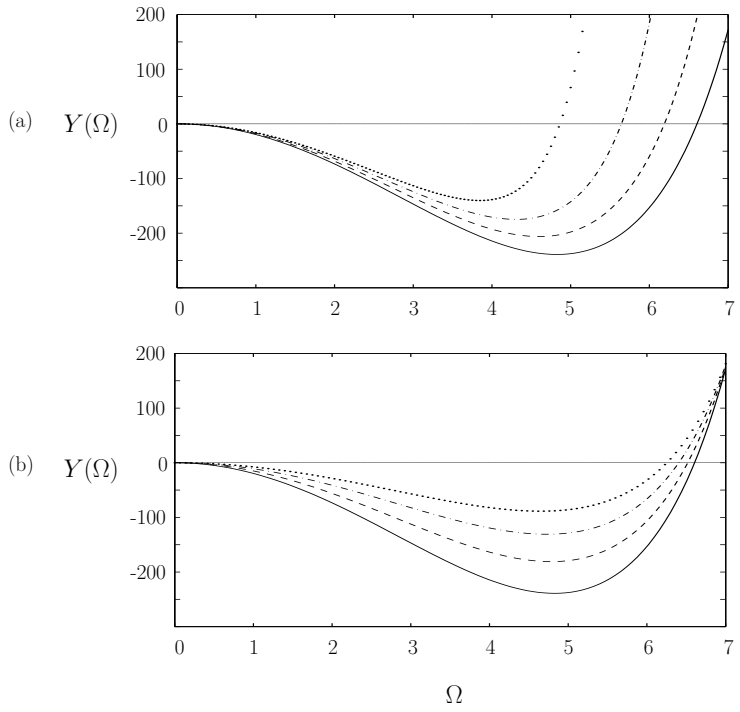

Figure 3.5: Function $Y(\Omega)$ where (a) the AC excitation voltage is held constant at $V_A = 40\,V$ and DC tuning voltage is varied (*solid* : $V_0 = 75\,V$, *dashed* : $V_0 = 70\,V$, *dashed* − *dotted* : $V_0 = 65\,V$, and *dotted* : $V_0 = 60\,V$) and (b) the DC tuning voltage is held constant at $V_0 = 75\,V$ and the AC excitation is varied (*solid* : $V_A = 40\,V$, *dashed* : $V_A = 35\,V$, *dashed* − *dotted* : $V_A = 30\,V$, and *dotted* : $V_A = 25\,V$). When $Y(\Omega) < 0$, Melnikov's method predicts that an invariant chaotic set exists.

say misaligned comb fingers where $r_{1A} > 0$ and $r_{3A} < 0$, Melnikov's criterion can still be satisfied. The aligned arrangement is chosen simply for comparison purposes with the work by DeMartini *et al* [38]. Having the set of representative parameters, numerical analysis is performed to study the system and to verify that Equation (3.16) does in fact describe the set of parameters where chaos occurs.

Depending on the magnitude of the AC and DC voltages chosen, α, β, δ, γ, and η can be tuned to satisfy Equation (3.16). As an example, choosing $V_0 = 75V$, $V_A = 40\,V$, and setting $x_0 = 1$ yields $\alpha = 0.0005$, $\beta = -1.25$, $\delta = 3.65$, $\gamma = 0.32$, $\eta = -0.128$, which not only satisfy (3.16) for a certain range of Ω, but also are consistent with the scaling assumptions above and requirements on β and δ. The function $Y(\Omega)$ is plotted in Figure 3.5. Chaos is predicted to occur for the band of Ω where $Y(\Omega) < 0$. For example consider the solid curve in Figure 3.5(a), where $V_A = 40\,V$ and $V_0 = 75\,V$; for this parameter set chaos is predicted to occur for $0 < \Omega < 6.6$. Notice also in Figure 3.5(a) that as V_0 decreases, the band of Ω for which chaos occurs decreases. A similar trend occurs when V_A is decreased, as shown in Figure 3.5(b).

Next, knowing that Melnikov's method predicts that chaos can occur for a range of parameters, it becomes important to determine what type of chaos occurs, specifically whether transient (temporary) chaos, attracting (sustained) chaos, or both exist. This is done numerically by integrating Equations (3.1) and studying the system's dynamics for a large number of parameter sets and initial conditions. Both attracting and transient chaos are found. Sustained chaos is the main interest in this study, due to its impact in practical engineering applications. Figure 3.6 depicts the system's phase space and time series for a set of parameters ($V_A = 40V$, $V_0 = 75\,V$, and $\Omega = 1.15$) where attracting chaos occurs. We determined that the

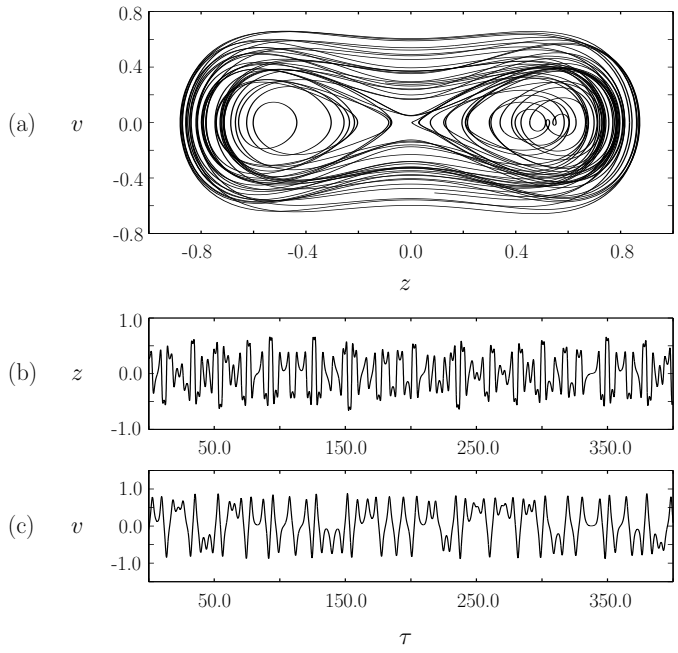

Figure 3.6: Numerical simulations for $V_A = 40\,V$, $V_0 = 75\,V$, and $\Omega = 1.15$ showing attracting chaos in: (a) (z, v) phase space, (b) z time series, and (c) v time series.

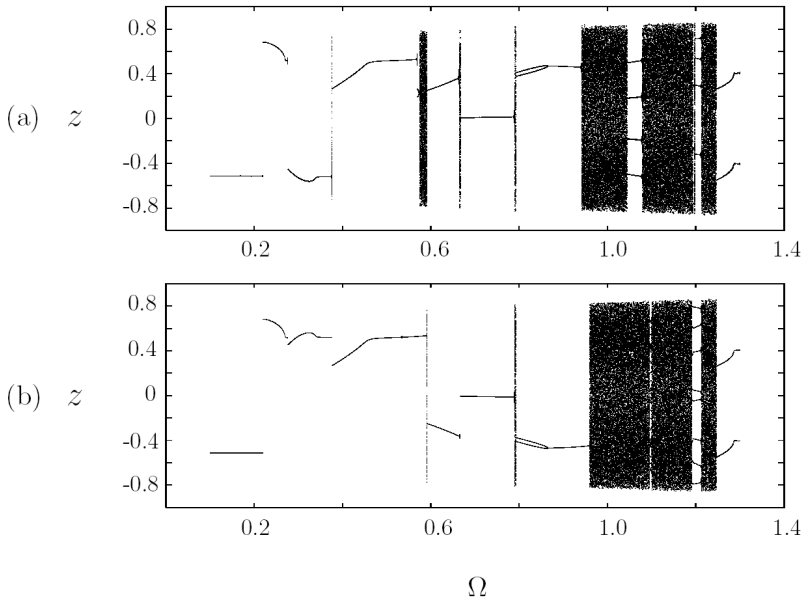

Figure 3.7: Bifurcation diagrams obtained by setting $V_A = 40\,V$ and $V_0 = 75\,V$ and adiabatically decreasing the value of Ω from $\Omega = 1.300$ and omitting transients after integrating for a sufficient number of time units. Here, the instantaneous value of the nondimensionalized displacement z is plotted when the trajectory pierces the Poincaré section defined by $\cos(\Omega\tau) = 0$ and $\sin(\Omega\tau) = 1$. At each value of Ω the equations are integrated for (a) 500 piercings of the Poincaré section and (b) 1500 piercings of the Poincaré section before omitting transients. This system contains multiple attractors at certain Ω values, but only one is depicted in each panel of this figure.

chaos is sustained (attracting) by integrating the equations for 10^6 time units and verifying that the trajectories do not repeat.

Using the same voltages, $V_A = 40\,V$ and $V_0 = 75\,V$, numerical bifurcation analysis with Ω treated as the bifurcation parameter reveals the various transitions between periodic and chaotic states. Figure 3.7(a) was constructed by beginning with $\Omega = 1.3$, adiabatically decreasing Ω, integrating for a sufficient amount of

time at each step to remove transients, and recording the instantaneous value of z each time the trajectory pierced the Poincaré section defined by $\cos(\Omega\tau) = 0$ and $\sin(\Omega\tau) = 1$. The two panels in Figure 3.7 represent different integration times at each Ω value. Due to the system's sensitive dependence on initial conditions, there are slight differences between the two panels. These differences also indicate that this system can have coexisting attractors for certain parameter sets, with only one shown for each Ω in each panel of Figure 3.7. For $1.247 < \Omega < 1.300$ in Figure 3.7(a) there is a stable periodic attractor with a period roughly two times that of the forcing. An abrupt transition to a chaotic state occurs at $\Omega = 1.247$, shown in the figure as a filled band. Within this chaotic region lies $\Omega = 1.15$, which is consistent with the results shown in Figure 3.6. We verified that this is chaotic behavior by integrating Equation (3.1) and observing the oscillations for Ω values that lie within these banded regions, and by analyzing the Poincaré maps and power spectra of the system. There are three large banded chaotic regimes between $0.942 < \Omega < 1.246$, with small periodic windows between, which indicate that there is a fairly large regime of parameter space for which this oscillator can exhibit attracting chaotic behavior; therefore, if an oscillator is created with parameters close to the ones shown in Table 3.2, then chaotic behavior should be relatively easy to find by independently adjusting V_A, V_0, and Ω. We note that

qualitatively similar bifurcation diagrams have been computed for a different, non-parametrically forced nonlinear oscillator in [135].

Holding $V_A = 40\,V$, a series of bifurcation diagrams showing the dependence on V_0 was created in the same manner as Figure 3.7; see Figure 3.8 for $47.5\,V < V_0 < 80\,V$. For $V_0 = 52.5\,V$, which is just above $V_{0,crit}$ for $\beta < 0$, thick banded chaotic regions reside at low frequencies below $\Omega = 0.2$. As the DC voltage is increased, the chaotic bands become wider and spread into the higher frequency regions of parameter space. In a practical MEM device, it is likely that there will be an upper limit on the value of V_0 that the device can handle. For applications where chaos is desirable, such as signal encryption, when operating at lower DC tuning voltages chaos should be present at low frequencies relative to the natural frequency of the device.

3.4 Experimental Verification of Chaos

A MEM oscillator, which satisfies Melnikov's criterion for a range of applied AC and DC voltages, has been designed and fabricated. An SEM image of the device is shown in Figure 3.1. Similar to the device discussed in Section 3.3.4, misaligned comb fingers were chosen for DC tuning, aligned comb fingers were chosen for actuation, and fixed-fixed flexures were chosen to provide the highly nonlinear

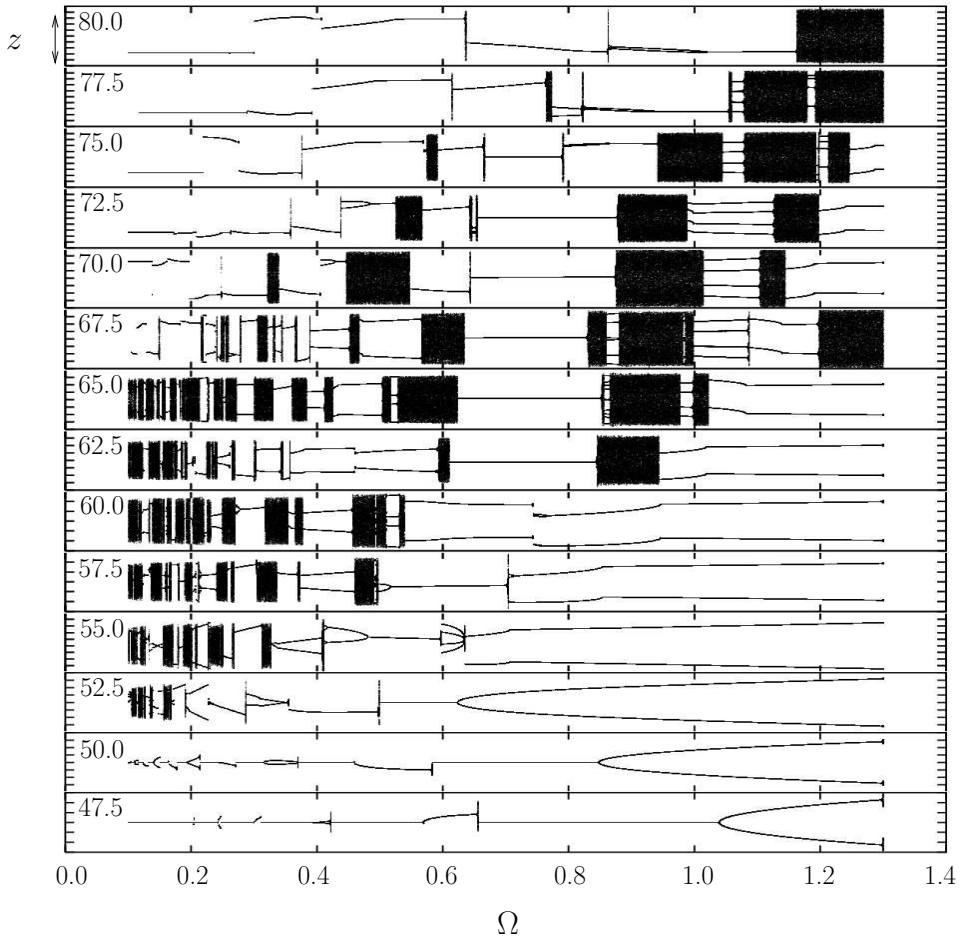

Figure 3.8: Bifurcation diagrams similar to Figure 3.7 ($V_A = 40\,V$) stacked on top of one another for different DC tuning voltages V_0, specified in the upper left hand corner of each diagram. Evident from these plots is the relationship between the banded chaotic regions and the DC tuning voltage.

mechanical restoring force. The DC tuning comb fingers were designed with a $2\,\mu m$ width, $7\,\mu m$ spacing, $1\,\mu m$ gap, and $15\,\mu m$ length. The AC driving comb fingers were designed with a slightly different geometry, specifically the comb fingers attached to the electrode were designed with a $3\,\mu m$ width and comb fingers attached to the oscillator backbone with a $2\,\mu m$ width in order to increase the displacement range of the oscillator (there is an allowable displacement for aligned comb fingers, which if exceeded, will cause the comb drive stiffnesses to change; they would become misaligned). Also, the AC driving comb fingers were made to have $11\,\mu m$ spacing, $1.5\,\mu m$ gap, and $15\,\mu m$ length. Each fixed-fixed flexure was designed with a $2\,\mu m$ width and a $225\,\mu m$ length and the depth of the entire structure was $20\,\mu m$. Parameters estimated through finite element simulations are shown in Table 3.3. Note, the value for Q in this table was estimated experimentally for the device in $535\,mTorr$ vacuum, which was the vacuum pressure used for all the results in this section. The pure elastic linear natural frequency was $9.2\,kHz$ in experiment, which differs slightly from the natural frequency estimated from the Table 3.3 parameters ($12.3\,kHz$). In all experiments the driving frequency is less than the pure elastic linear natural frequency (corresponding to the lowest frequency vibration mode of the structure), so that other vibration modes do not contaminate the oscillator's response.

Table 3.3: Estimated parameters for experimental device.

k_1	$9.6\,\mu N/\mu m$
k_3	$7.3\,\mu N/\mu m^3$
m	$1.6 \times 10^{-9}\,kg$
Q	1558
r_{10}	$-4.7 \times 10^{-3}\,\mu N/(V^2 \mu m)$
r_{30}	$1.8 \times 10^{-4}\,\mu N/(V^2 \mu m^3)$
r_{1A}	$1.1 \times 10^{-3}\,\mu N/(V^2 \mu m)$
r_{3A}	$-1.4 \times 10^{-4}\,\mu N/(V^2 \mu m^3)$

Variations in parameters resulting from small imperfections in the fabricated structure will affect the onset of chaos according to Equation (3.16). However, since parameters β and δ depend on V_0 and γ and η depend on V_A, the device can still be tuned to give chaos, and it is thus qualitatively insensitive to small parameter variations.

To test whether or not the device can achieve (3.8), a DC voltage was applied to the tuning set of comb fingers and was increased until it buckled to a new equilibrium position. This was done statically and the relative position of the device was observed through a microscope. As seen in Figure 3.9, the device's stable equilibrium position, where the comb fingers are completely aligned, becomes unstable somewhere between $V_0 = 36.0\,V$ (Figure 3.9(a)) and $V_0 = 36.5\,V$ (Figure 3.9(b)), giving rise to a bifurcation where two new stable equilibria are born. The slight misalignment at $36.5\,V$ shows that the system settled to one of the new stable equilibria positions. It is important to note that the device snaps to one of

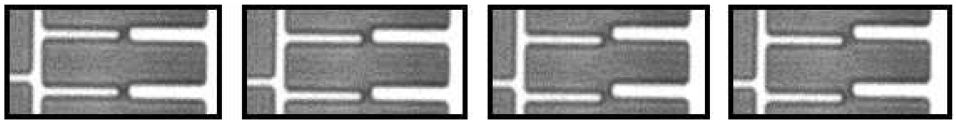

Figure 3.9: Zoomed in views of comb fingers (in each panel the left two fingers are attached to the suspended structure and the right fingers are attached to the static electrode), depicting the transition to the buckled state where the effective linear stiffness is negative ($\beta < 0$) and the effective nonlinear stiffness is positive ($\delta > 0$). Here a DC voltage is applied to the tuning set of comb fingers (corresponding DC voltages are shown below each panel) and no AC excitation is provided to the other set. Note, the comb fingers shown are originally aligned when no DC voltage is applied. The comb fingers remain aligned for $V_0 = 36.0\,V$ (panel (a)), but when the $V_0 = 36.5\,V$ (panel (b)) the structure buckles to one of two new equilibrium positions (i.e. $\beta < 0$ and $\delta > 0$), shown by the slight misalignment of the fingers. As the the voltage is increased, panels (c) and (d), the fingers become more misaligned, which corresponds to the broadening of the double well potential.

the two stable equilibria positions over the other due presumably to the presence of small fabrication-induced asymmetries that give rise to a distorted double well potential. As the DC voltage was increased, say to $37.0\,V$ (Figure 3.9(c)), the oscillator's new equilibrium position moved further away from its original equilibrium position. This is consistent with the behavior of the system's double well potential when V_0 is increased. It is therefore concluded that for DC tuning voltages above $36.5\,V$ the oscillator's phase space will have a homoclinic structure, with $\beta < 0$ and $\delta > 0$. Since $r_{30} > 0$, the $\delta > 0$ criterion will be satisfied for all V_0.

To test the dynamical behavior of the oscillator in its buckled state, a vibrometer was used [132]. Since the motion of the device was in-plane with respect to the substrate, a 45° mirror was machined, with a focused ion beam, next to the proof mass so that the laser could be reflected off its vibrating surface. While applying a DC voltage to the tuning set of comb fingers, which was above the critical DC voltage, a square root cosine signal was applied to the driving comb fingers to actuate the device. For this experiment, there was an upper limit on the DC voltage that was determined by the spacing of the comb fingers. Since the oscillator displaces as V_0 is increased past $V_{0,crit}^{\beta}$, a point can be reached where the relative position of the noninterdigitated comb fingers causes the sign of the electrostatic stiffness coefficients to change (i.e., the misaligned fingers get closer to being aligned and visa versa), in which case a homoclinic orbit may no longer exist. From the force-displacement curve obtained from finite element analysis, it was found that the misaligned tuning comb fingers could only displace $\pm 2.2\,\mu m$ and the aligned driving comb fingers could only displace $\pm 1.8\,\mu m$ before the sign of their respective stiffness coefficients changed. As a result, only a very narrow band of V_0 was explored.

Further evidence that the system contains a homoclinic structure comes from experimentally observed periodic attractors for different choices of V_0, V_A, and ω. Before proceeding, it is important to note that the vibrometer integrates the ve-

locity measurement to obtain the displacement, so there was some drift associated with the experimental displacement values. As a result, the displacement results have some amount of offset so that zero displacement does not correspond to the original equilibrium position. Figure 3.10 shows an experimentally observed periodic attractor for $V_0 = 37.1\,V$, $V_A = 13.2\,V$, and a driving frequency of $1100\,Hz$, and Figure 3.11(a) shows a different experimentally observed periodic attractor for $V_0 = 37.1\,V$, $V_A = 14.8\,V$, and a driving frequency of $1500\,Hz$. The shapes of these periodic orbits in phase space are consistent with a system that contains homoclinic trajectories for $\epsilon = 0$ [52]. Figure 3.11(b) shows a periodic attractor found numerically for the parameters in Table 3.3, with $V_0 = 47\,V$, $V_A = 15.9\,V$, and a driving frequency of $1500\,Hz$. This strongly resembles the periodic orbit shown in Figure 3.11(a), although, interestingly, the period of the periodic orbit shown in Figure 3.11(a) is twice the period of the driving signal, while the period of the periodic orbit shown in Figure 11(b) (and that shown in Figure 3.10) is equal to the period of the driving signal.

In addition to finding numerous periodic attractors, regions of (V_A, V_0, ω) parameter space were found where attracting chaos occurs. For example, when $V_0 = 37.1\,V, V_A = 13.8\,V$, and $\omega/2\pi = 2000\,Hz$, a chaotic attractor was found experimentally, with a time series shown in Figure 3.12(a). Using the parameters from Table 3.3 and nearby V_A, V_0, and ω, attracting chaos was found numerically,

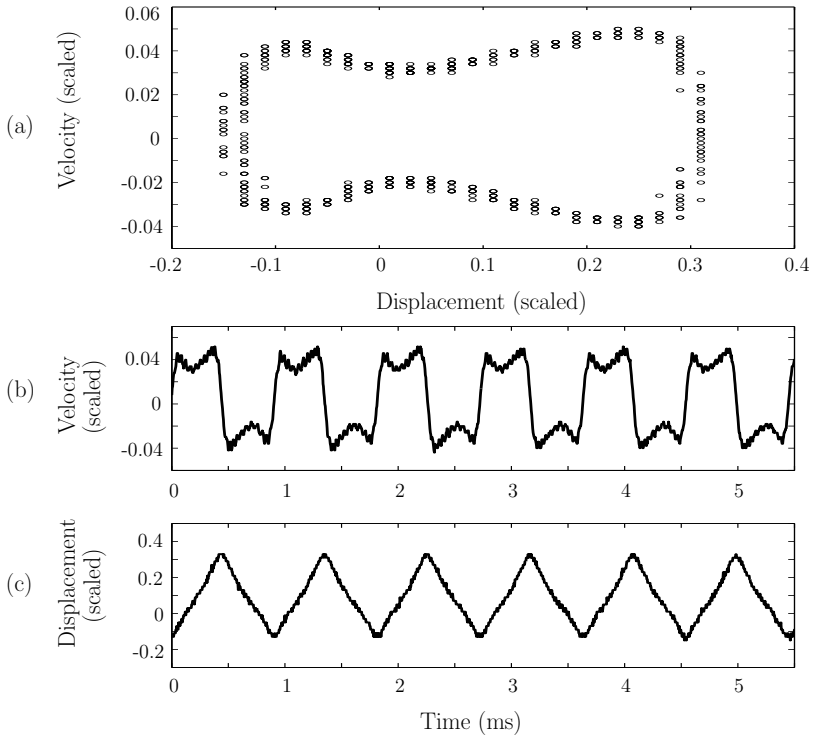

Figure 3.10: A periodic attractor for the experimental device for $V_0 = 37.1\,V$, $V_A = 13.2\,V$, $\omega/2\pi = 1100\,Hz$ (1 Velocity (scaled) unit = $125\,mm/s$ and 1 Displacement (scaled) unit = $8\,\mu m$).

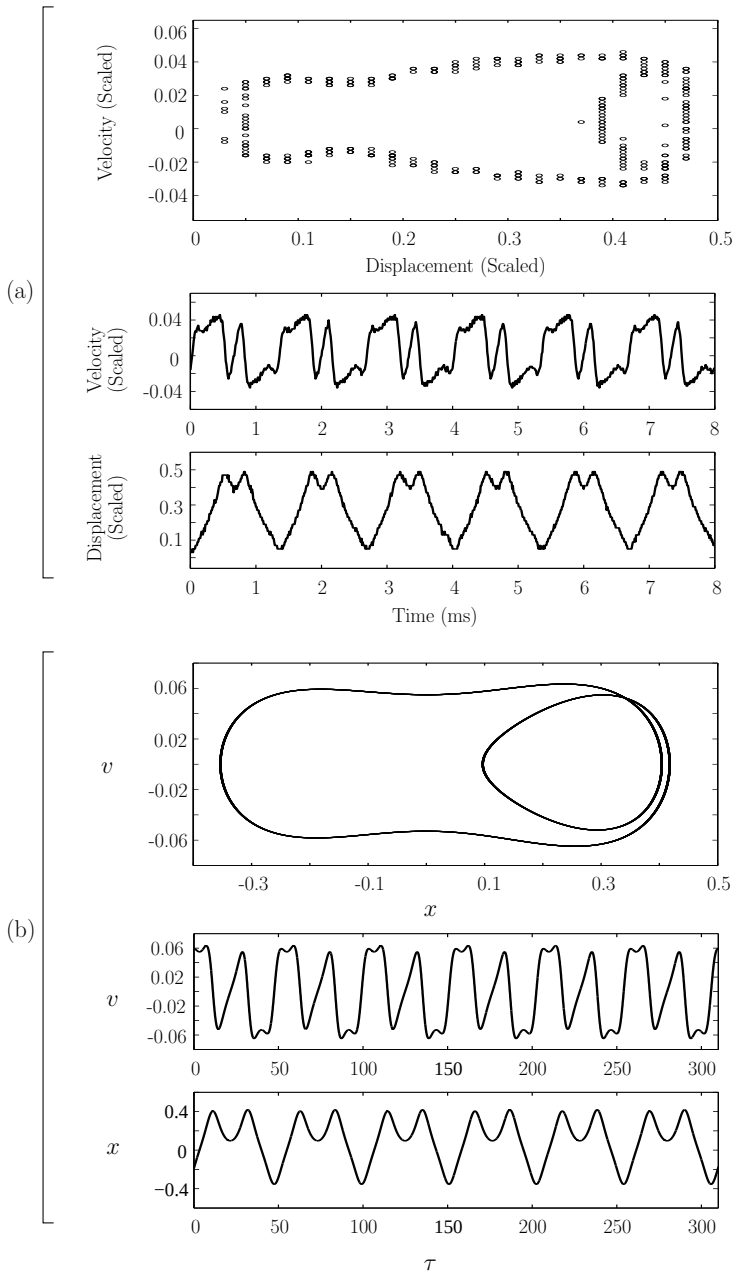

Figure 3.11: Comparison of a periodic attractor obtain in (a) experiment for $V_0 = 37.1\,V$, $V_A = 14.8\,V$, $\omega/2\pi = 1500\,Hz$ (1 Velocity (scaled) unit = $125\,mm/s$ and 1 Displacement (scaled) unit = $8\,\mu m$) and (b) numerical simulation for $V_0 = 47.0\,V$, $V_A = 15.9\,V$, $\omega/2\pi = 1500\,Hz$.

as shown in Figure 3.12(b). To verify that the chaos is sustained, the equations were integrated for 10^6 time units. We note that here the experimental device was tested at $V_0 = 37.1\,V$, which is slightly above its critical DC tuning voltage. Since the predicted parameters in Table 3.3 are not expected to be exactly the same as those for the device due to fabrication issues, the critical DC tuning voltage for homoclinic orbits to occur is different. The transition voltage for the parameters in Table 3.3 is $V_{0,crit}^{\beta} = 45.2\,V$. To be consistent with the experiment, a value of $V_0 = 46.5\,V$, slightly above this theoretical prediction, was chosen for the simulation shown in Figure 3.12(b).

Spectral analysis of an oscillator's time series is a good indicator of whether or not it is chaotic [81]. This was done here by taking the Fourier transform of the time series obtained experimentally and numerically with the same V_A, V_0, and ω as in Figure 3.12. The power spectrum was found by taking the modulus of the Fourier transform, and determines the relative strength of each periodic component in the time series. In general, systems whose time series are chaotic will have a broad power spectrum. Figure 3.13(a) shows such a broad power spectrum for the actual device, suggesting chaotic oscillations for these parameters. Figure 3.13(b) shows a similarly broad power spectrum from numerical simulations. The peak of the experimental power spectrum is apparently at half the driving frequency (although there is also substantial power at the driving frequency), while

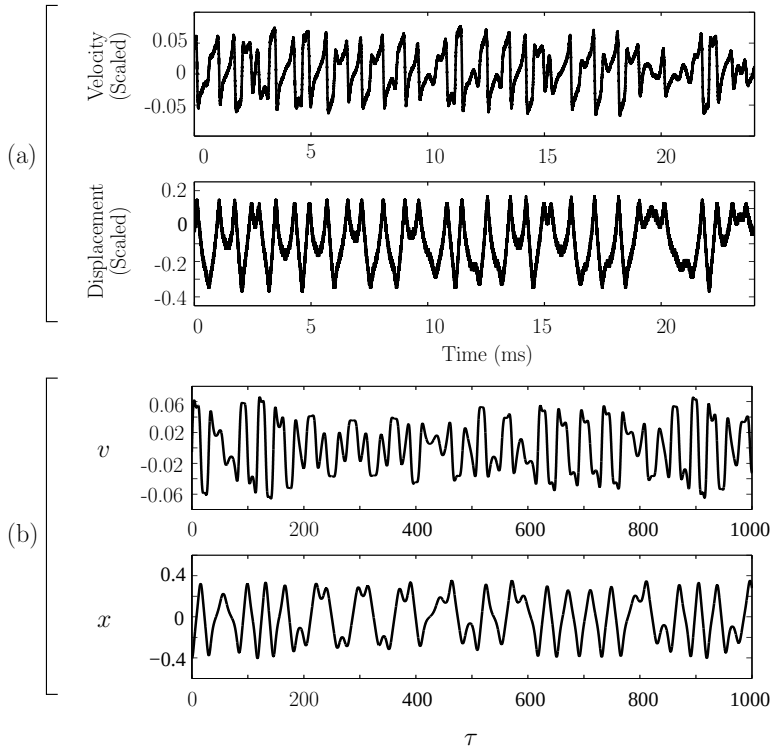

Figure 3.12: Comparison of a chaotic time series obtained in (a) experiment for $V_0 = 37.1\,V$, $V_A = 13.8\,V$, $\omega/2\pi = 2000\,Hz$ (1 Velocity (scaled) unit = $125 mm/s$ and 1 Displacement (scaled) unit = $8\,\mu m$) and (b) numerical simulation for $V_0 = 46.5\,V$, $V_A = 15.0\,V$, $\omega/2\pi = 2010\,Hz$.

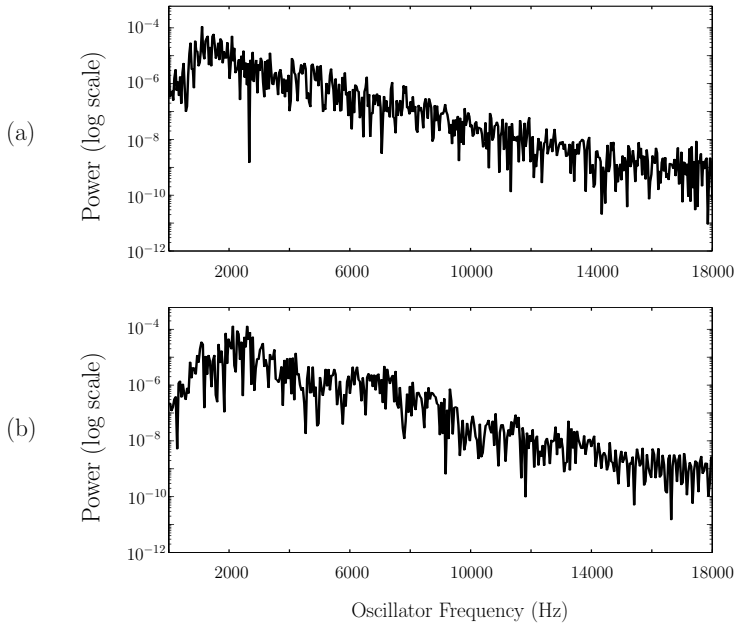

Figure 3.13: Power spectra calculated by taking the Fourier transform of a chaotic velocity time series from (a) experiment ($V_0 = 37.1V$, $V_A = 13.8V$, $\omega/2\pi = 2000\,Hz$) and (b) numerical analysis ($V_0 = 46.5\,V$, $V_A = 15.0\,V$, $\omega/2\pi = 2010\,Hz$) showing the broadband nature of the chaotic attractor (the scaled velocity units prior to taking the Fourier transform are identical to Figure 3.12 for (a) and (b)).

the peak of the numerical power spectrum is apparently at the driving frequency (although there is also substantial power at half the driving frequency). This suggests that the experimental and numerical chaotic oscillations are quite similar, but differ somewhat in their details.

For the estimated parameter set in Table 3.3 and fixed V_0 a boundary was derived from Equation (3.16) in $\omega - V_A$ space which predicts where chaos occurs (above the curves). For comparison purposes, this boundary was also tested experimentally. This was done by fixing $V_0 = 37.0\,V$, increasing V_A until attracting chaotic behavior was observed, and recording this V_A every $50\,Hz$. For this experiment, the device was only tested for V_A below $25.0\,V$, since similar devices failed for voltages slightly above this value. No chaos was observed for frequencies past $3300\,Hz$ since the drive voltage necessary to achieve chaotic behavior becomes too large. The boundary for attracting chaotic behavior found in the experiment lies above the theoretical boundaries for the existence of a chaotic set predicted by Melnikov's method, shown in Figure 3.14. The gap between the theoretical and experimental curves could be due to the fact that the chaos predicted by Melnikov's method could be transient or attracting, and we only show the experimental boundary for attracting chaos.

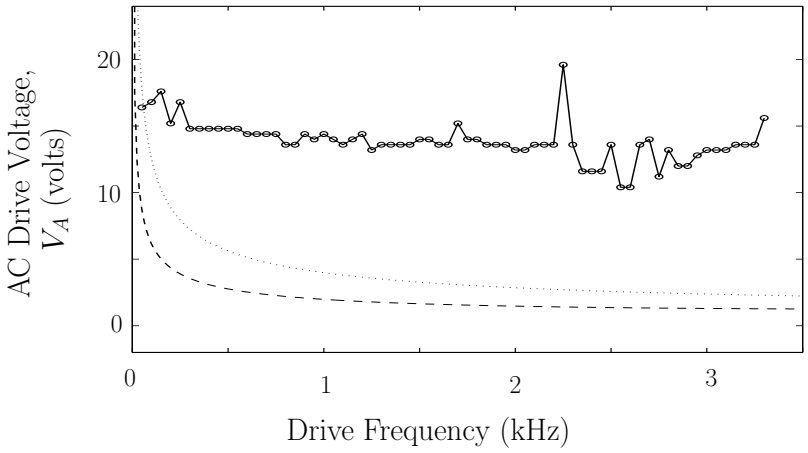

Figure 3.14: Boundaries for chaotic motion in AC Drive Voltage versus Drive Frequency space. Above the experimental curve (solid curve) attracting chaos exists ($V_0 = 37.0\,V$), and above the curves predicted by Melnikov's Method (dashed curve: $V_0 = 47.0\,V$ and dotted curve: $V_0 = 37.0\,V$) chaotic motion, which could be transient or attracting, is possible.

Chapter 4

Conclusions and Future Work: Nonlinear MEMS

4.1 Linear and Nonlinear Tuning

To utilize parametric resonance in a wide variety of applications, methods for predicting and manipulating the dynamics of such devices are necessary. An accurate model for the dynamics of a class of oscillators exhibiting both linear and nonlinear time varying stiffness terms has been developed and verified in [105], along with a system identification procedure in [36]. In order to implement this technology into applications such as filtering, additional tuning techniques, proposed in [104], are required. In the experimental study detailed in Chapter 2 the

linear and nonlinear tuning concepts from [104] have been proved. The parametric region of instability has been rotated counterclockwise and clockwise for two devices (referred to as Devices 1 and 2), by applying proportional AC and DC voltages to independent sets of noninterdigitated comb drives. It has also been shown that choosing $\rho \approx -1/2$ for Device 1 rotates the right stability boundary roughly to the vertical position since $r_{1A} > 0$ and choosing $\rho \approx -1/2$ for Device 2 rotates the left stability boundary roughly to the vertical position since $r_{1A} < 0$. In this work proof of concept was more important than obtaining perfect verticality and frequency independence of the stability boundary in each device, however more precise tuning can be used to obtain frequency independent boundaries for filtering applications. These same two oscillators have also been designed to exhibit specific nonlinear behavior, to prove the concept of nonlinear tuning. Specifically, the geometry of the noninterdigitated comb drives and flexures was chosen so the system's two effective nonlinearities, η_1 and η_2, are tuned either to be both positive or both negative, creating either a hardening or softening response, respectively, for a range of applied AC voltage. Device 1 was designed so that the system's effective nonlinearities become negative at relatively low applied voltages. This device's experimental response showed softening behavior at AC drive voltages as low as $4.2\,V$, indicating that the nonlinear tuning scheme worked and that both effective nonlinearities were negative above this voltage. The nonlinear tuning

scheme was also proved in the experimental results of Device 2, but for the case of two positive effective nonlinearities yielding pure hardening behavior. In conclusion, methods for tuning the dynamic behavior of parametrically excited MEMS have been proved through experiment. These methods will help such oscillators become more applicable to a wide range of technologies.

4.2 Chaotic Behavior

In Chapter 3, the existence of chaos in the tunable parametrically excited MEMS oscillator discussed in Chapter 2 was investigated using Melnikov's method. The result of this analysis was an inequality describing the set of parameters where chaos occurs. This is a useful design tool for tailoring the oscillator's parameters so that homoclinic chaos either occurs or does not occur as desired. For instance, this expression can be used to help avoid chaos in mass sensing and filtering applications. For a representative parameter set, numerical simulations showed that chaos does occur in regions of parameter space satisfying the criterion from Melnikov's method, and helped to better understand the complicated dynamics of the oscillator. A MEM oscillator with two sets of noninterdigitated comb drives (one for AC actuation and one for DC tuning) was designed and fabricated so that it satisfies Melnikov's criterion for a region of parameter space. By tuning the

device with the DC comb drives, the effective linear and nonlinear stiffnesses are made to be negative and positive respectively, which means that the unperturbed system contains a homoclinic orbit. This was verified experimentally by observing the oscillator buckle to a new equilibrium position after the critical DC voltage was reached; this was where the system's linear stiffness became negative. By actuating the device with the second set of electrodes, many interesting attractors were found, including periodic orbits and chaos. Time series and broadband spectra observed experimentally show both that the MEM device is chaotic for appropriate parameters and that the criterion from Melnikov's method is valid for predicting chaotic behavior. Boundaries in parameter spaced defined by the Melnikov criteria were compared to experimental boundaries and show that Melnikov's criteria provides a conservative estimate of the region of parameter space where chaos occurs.

4.3 Future Work

Methods for predicting and manipulating the dynamics of nonlinear parametrically excited MEM devices have been detailed in the first two chapters. Future work is aimed at using the linear and nonlinear tuning techniques from Chapter 2 to create high pass and low pass filters with optimized parameters. The

tuned devices can then be combined with the hardware scheme presented in [104] to create highly effective band pass filters. Experiments will involve quantifying important metrics such as stopband rejection, insertion loss, and the flatness of the passband response, which have not yet been quantified for this type of filter. These metrics will help evaluate the filter's overall performance and ultimately make valuable comparisons will conventional linear devices. In addition these tuning methods can also be utilized in mass sensing applications (see [148]) where certain frequency response characteristics are desired.

As detailed in Chapter 3 homoclinic chaos can occur in tunable parametrically excited MEMS resonators for certain parameters that are predicted by Melnikov's method. Initial experiments have involved studying the time series, phase space, and power spectrum of the periodic and chaotic attractors. In the future it would be interesting to experimentally investigate the Poincaré maps of the system and map out bifurcation diagrams similar to Figure 3.7 to determine the regions of parameter space where chaos and other interesting attractors live. A thorough system identification procedure, similar to [36], can also be carried out to compare experimental and numerical results.

An interesting path for this research would be to create oscillators for specific applications where chaotic behavior is beneficial. There are many possible applications areas where the complex behavior of these tunable nonlinear devices can

be utilized, however, to date, very few have been considered. For instance, sophisticated signal encryption devices can be created for secure communications [141]. This type of oscillator would be ideal for such applications since chaos occurs for such a broad range of parameters. These oscillators could also be used in microfluidic mixing for lab-on-a-chip applications. In this case the chaotic oscillator would be used as an actuator and placed in a microfluidic channel or chamber to chaotically force the fluid, which could lead to an increase in mixing efficiency.

Another interesting architecture where chaotic behavior is expected to occur is a microbeam buckled by a compressive end load. In the device shown in Figure 4.1 a DC current I_{DC} is applied to a conductive loop on the microbeam's top surface and a magnetic field is supplied by an external magnet to generate a Lorentz force F_b to axially compress the microbeam. The compressive load at the end of the microbeam, will cause the microbeam to buckle to a new equilibrium position when a critical load is reached. This is due to the double-well nature of the potential energy, a consequence of the effective linear stiffness being negative. For a more thorough treatment of this device see Appendix A. Devices can be fabricated using standard micromachining techniques, similar to [102, 103]. Melnikov analysis can be used to predict the existence of chaos for the system and the dynamics of the device can be studied numerically and experimentally.

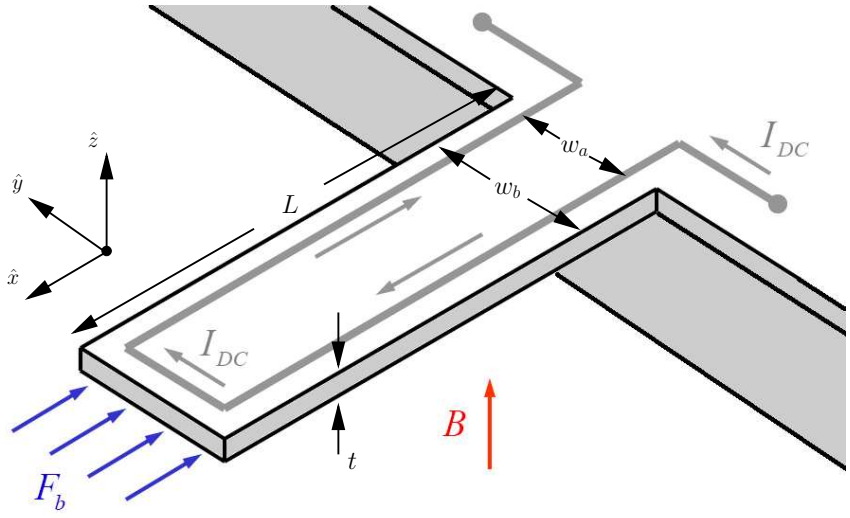

Figure 4.1: Concept for a chaotic oscillator based on a microbeam buckled by an end load.

Chapter 5

SISO, Multi-Analyte Sensor - Theory

In this chapter, the theory for a novel mass sensor platform that allows for multiple analytes to be detected with a single sensor input and single sensor output is presented. The sensor is composed of an array of frequency mistuned resonators that are commonly coupled to a comparatively larger shuttle mass. In a practical implementation, each resonator in the array would be functionalized with different coatings that are either specific or partially specific to different analytes. The unique sensor design utilizes vibration localization in the set of coupled resonators to embed all requisite resonance frequency information in the response of the shuttle mass. As a result, mass additions occurring on any or all of the resonator's

surfaces can be detected with a single output signal using solely the response of the shuttle mass.

This chapter begins with a detailed description of the mathematical model used to capture the dynamic behavior of this novel architecture. Next, the frequency response of the device used for sensing is analyzed and design issues are thoroughly addressed. The mass responsivity matrix for the coupled system is analyzed and compared to the mass responsivity of an uncoupled system. It is shown that for sufficiently localized resonant modes, the responsivity for the coupled system is less than, but close to, the mass responsivity for an uncoupled system. A derivation for the frequency resolution of isolated mass sensors, which can be adopted to evaluate the frequency resolution of the coupled system, is detailed. It is shown that the reduction in amplitude inherent to the coupled architecture leads to a reduction in frequency resolution. The effectiveness of a transducer to convert the mechanical motion into a measurable signal, which is often referred to as detectability, is also an important metric to consider. In the final section, using capacitive transduction as an example, the product of the detectability and sensitivity is shown to scale favorably for the coupled architecture.

5.1 Mathematical Model

The single input-single output (SISO) multi-functional mass sensor is composed of an array of frequency mistuned oscillators that are commonly coupled to comparatively larger shuttle mass oscillator, which is used for both actuation and sensing. The dynamics of this system, assuming that nonlinearities can be neglected, can be described by the lumped-mass model shown in Figure 5.1(a). In Chapters 6, 7, and 8 this model is used to develop micro-structures that exhibit qualitatively similar dynamics. Figure 5.1(b) shows a first generation device, which is detailed later in Chapter 6, where the microbeams labeled M correspond to the oscillator array, and the large mass labeled SM, which is suspended by four flexures labeled S, corresponds to the shuttle mass in Figure 5.1(a). As a result, throughout this chapter the oscillators in the lumped mass model will be referred to as microbeams.

The model is composed of a shuttle mass that has mass m and stiffness k, and an array of comparatively smaller microbeam oscillators with m_1, m_2, etc. denoting the masses and k_1, k_2, etc. denoting the stiffnesses. Intrinsic and extrinsic dissipation, arising primarily from aerodynamic and material dissipation effects, are described by linear dashpot elements c for the shuttle mass and c_1, c_2, etc. for the microbeams. The generalized driving force that is applied to the shuttle mass

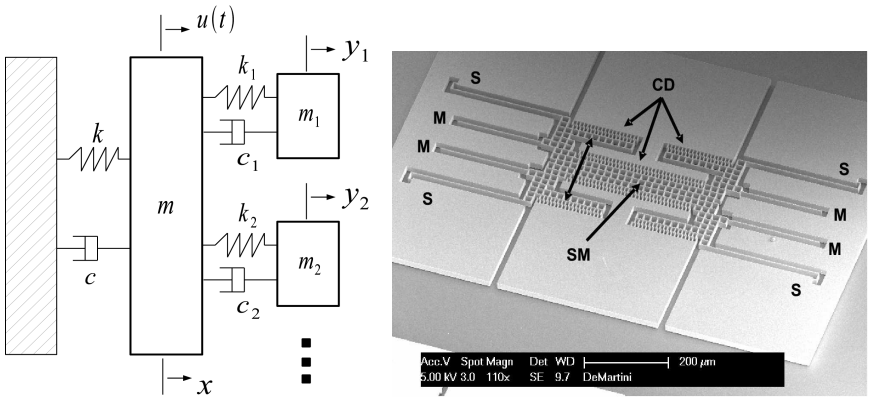

(a) (b)

Figure 5.1: (a) A mass-spring-dashpot description of the SISO microresonator array, where the larger mass m represents the sensors shuttle mass and the comparatively smaller masses m_1, m_2, etc., represent the microbeam oscillators. (b) A scanning electron micrograph of a SISO microresonator array detailed in Chapter 6, composed of microbeams M, a shuttle mass SM, and suspending flexure S.

is denoted $u(t)$. The equations of motion for this system are

$$\begin{aligned} m\ddot{x} + c\dot{x} + kx + \sum_{i=1}^{N} c_i(\dot{x} - \dot{y_i}) + \sum_{i=1}^{N} k_i(x - y_i) &= \frac{1}{m}u(t) \\ m_i\ddot{y_i} + c_i(\dot{y_i} - \dot{x}) + k_i(y_i - x) &= 0, \end{aligned} \tag{5.1}$$

where $i = 1, 2, ..., N$, N represents the number of microbeam sensors in the array, and x and y_i are the absolute displacements of the shuttle mass and the i^{th} microbeam sensor respectively. Equation (5.1) can also be written as

$$\begin{aligned} \ddot{x} + \frac{\omega_b}{Q_b}\dot{x} + \omega_b^2 x &= \frac{1}{m}u(t) - \sum_{i=1}^{N}\left(\epsilon_i\frac{\omega_i}{Q_i}(\dot{x} - \dot{y_i}) + \epsilon_i\omega_i^2(x - y_i)\right) \\ \ddot{y_i} + \frac{\omega_i}{Q_i}(\dot{y_i} - \dot{x}) + \omega_i^2(y_i - x) &= 0, \end{aligned} \tag{5.2}$$

where ω_b, ω_i, Q_b, Q_i, and ϵ_i are defined in Table 5.1. The system of $N + 1$

Table 5.1: Model Parameters.

Parameter	Description
$\omega_b = \sqrt{k/m}$	Shuttle mass resonance frequency
$\omega_i = \sqrt{k_i/m_i}$	Isolated resonance frequency of the i^{th} microbeam
$Q_b = m\omega_b/c$	Shuttle mass quality factor
$Q_i = m_i\omega_i/c_i$	Isolated quality factor of the i^{th} microbeam
$\epsilon_i = m_i/m$	Inertia ratio of the i^{th} microbeam

equations can be assembled into matrix form, which is given by

$$M\ddot{X} + C\dot{X} + KX = \Phi(t), \tag{5.3}$$

where M is the mass matrix, K is the stiffness matrix, C is the damping matrix, X is the state space vector, and $\Phi(t)$ is the forcing vector.

The time dependent forcing $u(t)$ is kept general and varies depending on the actuation method being modeled. For example if a the shuttle mass is excited electrostatically by an interdigitated comb drive actuator, assuming minimal fringing field effects and ample device thickness, the driving force will be

$$u_{es}(t) = \frac{\epsilon_0 nhV^2(t)}{g}, \tag{5.4}$$

where ϵ_0 is the free space permittivity, n the total number of comb fingers in the comb dirve, h the device thickness, g the gap between adjacent comb fingers, and $V(t)$ the time varying voltage applied to the comb drive. In most cases the time varying voltage is a sinusoidal function $V(t) = V_A \sin(\omega t)$, where V_A is the voltage

amplitude and ω the drive frequency. This is the actuation method adopted for the device discussed in Chapter 6 and in [37]. In Chapter 7, rather than directly actuating the shuttle mass, the device is base excited using an external piezoelectric stack actuator. When the device is base excited the equations of motion will still take the same form as Equations (5.1), however the state variable x will represent the displacement of the shuttle mass relative to the base instead of the absolute displacement and the driving force will be

$$u_{base}(t) = m\omega^2 W_0 \sin(\omega t), \tag{5.5}$$

where W_0 is the amplitude of the base motion.

5.2 Frequency Response

The response of the sensor can be determined by applying any one of the common linear systems techniques to Equation (5.3). For example, one method involves writing Equations (5.2) in state space form, applying the Laplace transform, and determining the resulting transfer function [28]. Another method involves using the mode-superposition method to uncouple the set of coupled equations, assuming a steady state solution, and solving for the complex frequency response [31]. Due to the large number of free parameters present in these equations (ϵ_i, ω_i, Q_i, ω_b, Q_b, ω, and $1/m$), specifically $(3N + 4)$ parameters, a large number of

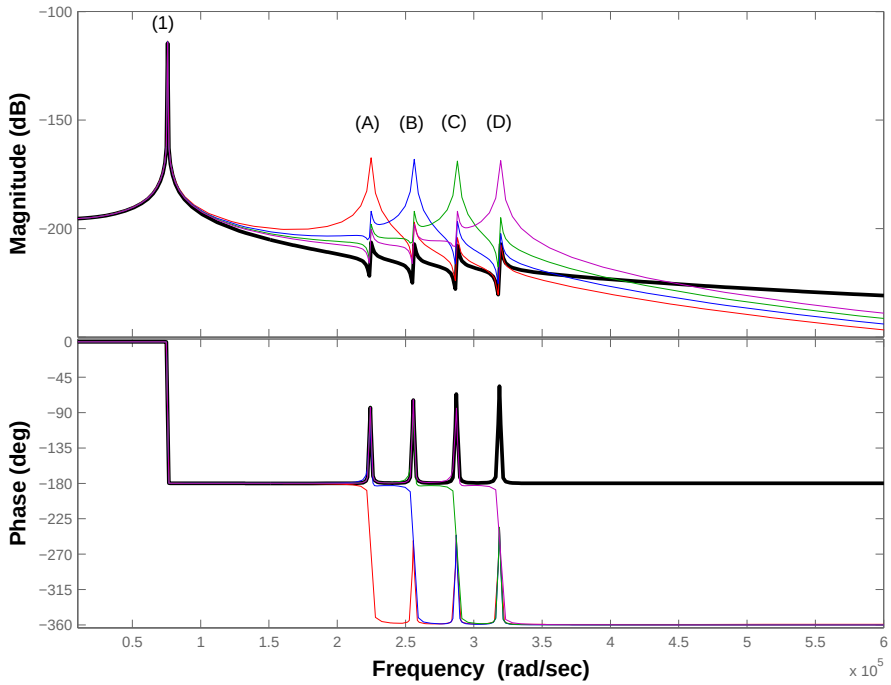

Figure 5.2: Bode plot for the SISO transducer with a low frequency rigid body mode (peak labeled (1)) and four higher frequency localized modes (peaks labeled (A)-(D)). The Black curve represents the response of the shuttle mass and the four colored curves represent the response of each microbeam oscillator.

qualitatively distinct responses are readily obtainable. For mass sensing applications, however, most of these responses are not suitable. This work utilizes one particular form of the frequency response that is amendable to sensing. This form of the frequency response is discussed here and is depicted in Figure 5.2.

Figure 5.2 depicts the frequency response for an array of four coupled microbeam oscillators, which contains five important features. The first feature, labeled (1), is a low-frequency resonance that corresponds to a bulk mode where

the shuttle mass and the microbeam oscillators move essentially together as a rigid body. The resonance frequency of this mode is approximately

$$\omega_{low} \approx \sqrt{\frac{k}{m + \sum_{i=1}^{N} m_i}}. \tag{5.6}$$

The response also contains four higher frequency resonances, labeled (A)-(D). These resonances correspond to localized modes where the vibration energy of the structure is largely confined to a single microbeam. This behavior is evident in Figure 5.2 where only a single microbeam experiences appreciable displacement at each resonance (A)-(D). For the simulated device the localized resonances occur at slightly higher frequencies than the respective isolated resonance frequencies of the four microbeam oscillators ω_1 through ω_4. A key feature of these localized modes is that they induce measurable resonances in the shuttle mass' response (black curve). As a result, using only the response of the shuttle mass, resonance shifts caused by chemomechanical processes on any, or all, of the microbeams can be detected. By functionalizing each of the N microbeam oscillators differently N distinct analytes can be detected using a single input and single output signal.

5.2.1 Design

Designing the device so that the shuttle mass' frequency response has the features depicted in Figure 5.2 involves careful selection of the system parameters.

The most important design parameters are the inertia ratios (ϵ_i) and the resonant frequency ratios (ω_i/ω_{low}), which are used to control the extent of mode localization [92, 7, 6] and the device's overall performance as a mass sensor. In order to achieve mode localization, the inertia ratios (ϵ_i), which dictate the coupling strength, must be small ($\ll 1$) and system resonance frequencies (ω_i's, ω_{low}, and other resonances not captured in the lumped-mass model) must be well spaced. For the coupled system mass and/or stiffness changes in a single microbeam lead to shifts in all of the system's resonance frequencies. However, if the frequency response is tailored to have strongly localized modes, then these mass and/or stiffness changes will result in distinctly larger shifts in the resonance associated with the altered oscillator. An example of behavior is shown in Figure 5.3, where the highest frequency microbeam is mass loaded and the corresponding resonance in the shuttle mass response shifts about two orders of magnitude more than the other resonances associated with the unloaded microbeams, which are induced solely through coupling. Therefore, the sensing principle presented herein allows for the identification of a given resonance shift's source and can be used for rapid analyte detection and identification.

The resonance frequency ratios (ω_i/ω_{low}) must be chosen carefully in the design process. The following criteria must be considered during design:

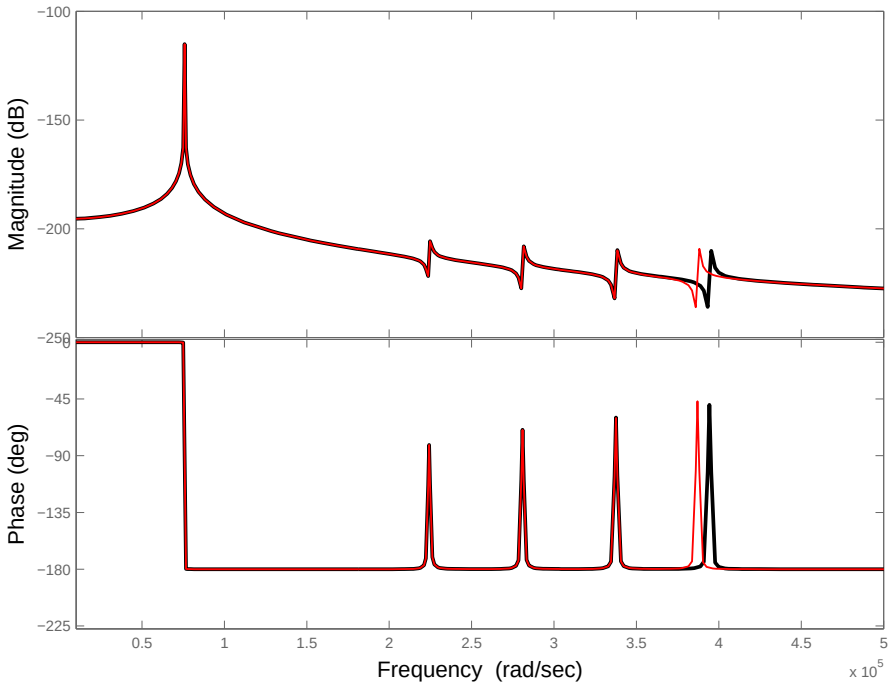

Figure 5.3: Bode plot for the SISO transducer showing the response of the shuttle mass before (black curve) and after (red curve) mass is added to the highest frequency microbeam oscillator.

- The coupled system's resonance frequency ratios must be greater than one, ($\omega_i/\omega_{low} > 1$). If they are close to or equal to one, then the localized modes (labeled (A)-(D)) are too close to the the low frequency mode (labeled(1)) and therefore can be contaminated, which can ultimately hinder the successful detection of analytes.

- Each frequency ratio (ω_i/ω_{low}) must be distinct and well separated from all other frequency ratios. If the frequency ratios are too closely spaced, then a multiresonance passband with indistinct resonances can occur, which can ultimately prevent multi-analyte detection.

- The resonance frequencies of the localized microbeam modes ($\approx \omega_i$) must also be well separated from other vibration modes that are not captured by the lumped-mass model. As in the first case, failure to meet this criteria could lead to contamination of the localization microbeam modes. In order to capture higher order modes of an actual micro-structure finite element analysis is used in the design process.

Another important parameter to consider, which directly influences the frequency response, is the damping. The quality factors of the system's resonances directly impact how closely they can be to one another and the number of microbeams that can be integrated into the system. For example, if the system is

to operate in a low damping environment, then the system's resonances can be closer spaced than they can be in a high damping environment. A reasonable approximation for the smallest practical frequency spacing between each localized microbeam mode is

$$\Delta\omega_i^{min} \approx \Delta\omega_{nom} = \frac{\omega_{nom}}{Q_{nom}}, \tag{5.7}$$

where $\Delta\omega_{nom}$ is the average bandwidth of the isolated microbeam resonance curves at half the maximum amplitude, ω_{nom} is the mean resonant frequency of the localized microbeam modes, and Q_{nom} is the mean quality factor of the localized microbeam modes. For a given non-resonant frequency window with bandwidth B, the maximum number of microbeam resonances (and thus number of microbeams) that can fit into this frequency band can be approximated as

$$N_{max} \approx \frac{BQ_{nom}}{\omega_{nom}}. \tag{5.8}$$

For an actual device the bandwidth B is set by the low frequency resonance (ω_{low}) and the first resonance not captured by the lumped mass model (ω_{high}); in other words $B = \omega_{high} - \omega_{low}$. For applications requiring large arrays, N_{max} may be insufficient and it may possible to exploit multiple non-resonant pass bands.

The excitation amplitude is also important, but will depend on the actuation method used and can be tuned during operation. For mass sensing the oscillator amplitude directly affects the frequency resolution (this will be discussed later

in this chapter) and ultimately the performance of the device as a sensor (i.e. larger amplitudes lead to better frequency resolution). It is therefore desirable to drive the device with the largest possible excitation amplitude. However, practical limitations on the maximum excitation amplitude are set by nonlinearities and critical device failure, which typically occur at large excitation amplitudes.

5.3 Sensor Metrics

In the process of developing a mass sensor platform it is important to determine pertinent metrics, both analytically and experimentally, that help evaluate its performance and compare its performance to other mass sensor platforms. For mass sensors this metric is mass sensitivity, which is a measure of the smallest added mass that can be detected with a given platform. For mass sensors operating in resonant mode, this metric turns out to be the product of two important metrics, mass responsivity and frequency resolution. The mass responsivity of a system is a deterministic quantity that dictates how much the resonant frequency changes for a given added mass. The frequency resolution, on the other hand, takes into account the stochastic nature of the frequency measurement and represents the smallest frequency shift that can be accurately measured in the presence of noise and uncertainty.

As shown in [42], the mass sensitivity for a single-degree-of-freedom (SDOF) resonator is

$$\delta m \approx R^{-1}\delta\omega_0, \tag{5.9}$$

where δm is the smallest detectable mass (or mass sensitivity), R is the mass responsivity, and $\delta\omega_0$ is the smallest resolvable frequency shift (or frequency resolution). Equation (5.9) assumes that δm is small compared to the effective mass of the resonator M_{eff} and that the effective stiffness and quality factor are not affected by the accreted analyte. Equation (5.9) can be extended for the multiple-degree-of-freedom (MDOF) sensor studied here. In this case the mass sensitivity becomes a vector, $\mathbf{\Delta m}$,

$$\mathbf{\Delta m} \approx \mathbf{S}^{-1}\mathbf{\Delta w}, \tag{5.10}$$

where the responsivity $\mathbf{S}$ is a square matrix that accounts for $N+1$ resonance shifts that can be induced by up to $N+1$ mass changes and $\mathbf{\Delta w}$ is a vector whose elements are the frequency resolutions that correspond to each of the system's resonance frequencies.

In Sections 5.4 and 5.5 the mass responsivity and frequency resolution, respectively, are determined for the MDOF, SISO mass sensor and compared to the conventional SDOF mass sensor.

5.4 Mass Responsivity

As discussed above, the mass responsivity is an important metric that tells how sensitive the resonant frequency of a device is to mass change. In this section it will be shown that the resonances of the MDOF sensor have resoponsivities very close to those of their SDOF counterparts provided that the modes are well localized.

First consider the SDOF case where the device has resonant frequency $\omega_0 = \sqrt{k_{eff}/m_{eff}}$. In this case the responsivity is determined by taking the derivative of the resonant frequency with respect to the effective mass, $\delta\omega_0/\delta m_{eff}$. The resulting mass responsivity is

$$R = -\frac{\omega_0}{2m_{eff}}. \tag{5.11}$$

In other words, a small resonator with small mass and high frequency will exhibit a large mass responsivity. As a result, micro and nano-scale beams are promising platforms for sensing due to their small size, high frequencies, and correspondingly high responsivities.

Next consider the more complicated MDOF case, where the coupled system has $N+1$ resonance frequencies, which are determined by solving for the eigenvalues of the matrix equation (5.3). This is accomplished by considering the eigenvalue

problem for the unforced, undamped system

$$(K - \Omega_r^2 M)V_r = 0, \tag{5.12}$$

where Ω_r^2 is the r^{th} eigenvalue, V_r is the corresponding r^{th} eigenvector, and $r = 1, 2, ..., N+1$. In order for Equation (5.12) to have nontrivial solutions, the following condition must be met

$$\det(K - \Omega^2 M) = 0. \tag{5.13}$$

Expanding Equation (5.13), yields a characteristic polynomial whose roots are the squared resonance frequencies (Ω_r^2) of the system. For the coupled system, if mass is added to one of the microbeams all resonances in the system will shift. Accordingly, the responsivity is a square $r \times j$ matrix ($j = 1, 2, ..., N+1$), $\mathbf{S}$ in Equation (5.10), which accounts for $N+1$ frequency shifts caused by $N+1$ mass additions. The elements of $\mathbf{S}$ are $S_{rj} = \delta\Omega_r/\delta m_j$, which quantify the shift of the r^{th} system resonance due to mass addition at the j^{th} resonator (i.e. the shuttle mass or any of the microbeam sensors).

If the response of the MDOF sensor is tailored to have strong mode localization, as discussed in Section 5.2, then the resulting responsivity matrix will be diagonally dominant. This is due to the drastically larger shifts in the resonances of the localized modes that occur when the associated microbeams are mass loaded (as compared to those shifts induced solely through coupling). The shifts due to

coupling are accounted for in the off diagonal elements (S_{12}, S_{12}, S_{23}, etc) and will be smaller for more localized systems.

5.4.1 Numerical Investigation

Here, the responsivity matrix (**S**) is demonstrated numerically and compared for two example systems. Both example systems consist of an array of four frequency mistuned microbeams that are commonly coupled to a comparatively larger microbeam that acts as the shuttle mass (this architecture is discussed later in Chapter 7). In both cases the mass of the shuttle ($m \approx 7.6 \times 10^{-11}\, kg$) is much larger than that of the microbeams ($m_1 \approx m_2 \approx m_3 \approx m_4 \approx 2.5 \times 10^{-12}\, kg$) and the resulting inertia ratios are small ($\epsilon_i \approx 0.030$). In the first case (a), all resonance frequencies are well spaced and the microbeam modes are highly localized. In the second case (b), the spacing between each resonance frequency is reduced to an order of magnitude and the modes are much less localized. The isolated resonance frequencies and frequency spacing for each case are listed below.

- **Case (a)** *well spaced resonances*:

  $\omega_b = 55\, kHz$, $[\omega_1, \omega_2, \omega_3, \omega_4] = [70\, kHz, 80\, kHz, 90\, kHz, 100\, kHz]$, the frequency spacing between the shuttle mass resonance and the first microbeam resonance is $15\, kHz$ and the frequency spacing between microbeam modes is $10\, kHz$.

- **Case (b)** *closely spaced resonances*:

  $\omega_b = 55\,kHz$, $[\omega_1, \omega_2, \omega_3, \omega_4] = [57\,kHz, 58.5\,kHz, 60\,kHz, 61.5\,kHz]$, the frequency spacing between the shuttle mass resonance and the first microbeam resonance is $1.5 kHz$, and frequency spacing between microbeams is $1.5 kHz$.

The responsivity matrix is determined by compiling the stiffness matrix (K) and mass matrix (M) for Equation (5.1), finding the eigenvalues (Ω_r^2) using Equation (5.13), and determining each element of the responsivity matrix $S_{rj} = \delta\Omega_r/\delta m_j$. Evaluating the resulting responsivity matrix using the parameters of case (a) gives

$$S^a = \begin{pmatrix} 0.2534 & 1.1502 & 0.7188 & 0.5496 & 0.4628 \\ 0.0282 & 13.7162 & 0.7080 & 0.2088 & 0.1186 \\ 0.0286 & 0.2205 & 16.6807 & 0.9120 & 0.2573 \\ 0.0318 & 0.0615 & 0.3180 & 19.8636 & 1.2807 \\ 0.0510 & 0.0396 & 0.1266 & 0.5996 & 23.8003 \end{pmatrix}, \qquad (5.14)$$

where the elements of S^a are in units $[Hz/pg]$. Element S^a_{11} of Equation (5.14) represents the responsivity of the low frequency rigid body mode due to mass loading of the shuttle and elements S^a_{22}, S^a_{33}, S^a_{44}, and S^a_{55} represent the responsivities of the localized microbeam modes due to mass loading of the corresponding microbeams. An important attribute of S^a is that the diagonal elements are much larger than the off diagonal elements (diagonally dominant). This means that if

mass binds to the lowest frequency microbeam, the corresponding localized resonance will shift significantly more than other resonances corresponding to the unloaded microbeams.

Evaluating the responsivity matrix using the parameters of case (b) gives

$$S^b = \begin{pmatrix} 0.1469 & 1.4941 & 1.2933 & 1.1379 & 1.0147 \\ 0.0013 & 7.8427 & 2.8146 & 0.4437 & 0.1793 \\ 0.0015 & 0.5493 & 5.4920 & 4.9544 & 0.6086 \\ 0.0014 & 0.1630 & 0.4542 & 3.4213 & 7.9034 \\ 0.2322 & 1.1150 & 1.4048 & 1.7988 & 2.3498 \end{pmatrix}, \tag{5.15}$$

where the elements of S^b are in units $[Hz/pg]$. In contrast to S^a, the diagonal elements of S^b are significantly reduced and the off diagonal terms have become larger. In fact, there are two instances where the off diagonal element is larger than the diagonal element, specifically $S^b_{34} > S^b_{44}$ and $S^b_{45} > S^b_{55}$, which ultimately render this system unfit for sensing. For example, if a $1\ pg$ mass binds to the highest frequency microbeam (Sensor 4), then the corresponding localized mode will shift $2.3498\ Hz$, but the next lowest frequency mode corresponding to an unloaded microbeam (Sensor 3) will shift $7.9034\ Hz$. As a result, even though mass has been added to Sensor 4, the shift pattern wrongly suggests that it has been added to Sensor 3 and therefore gives a false reading. This shows that the microbeam modes must be strongly localized for this system to be a viable mass sensor.

Table 5.2: Numerical comparison of responsivities for the MDOF sensor and the SDOF sensor.

Case (a)			
Sensor	$\frac{\omega_i}{\omega_b}$	$S_{rr}\left[\frac{Hz}{pg}\right]$	$R\left[\frac{Hz}{pg}\right]$
1	1.2613	13.7162	15.2535
2	1.4414	16.6807	18.6363
3	1.6216	19.8636	22.2376
4	1.8018	23.8003	26.0450
Case (b)			
Sensor	$\frac{\omega_i}{\omega_b}$	$S_{rr}\left[\frac{Hz}{pg}\right]$	$R\left[\frac{Hz}{pg}\right]$
1	1.0270	7.8427	11.2082
2	1.0450	5.4920	11.5044
3	1.0631	3.4213	11.8033
4	1.0811	2.3498	12.1046

Consider two sets of uncoupled microbeam sensor arrays that are identical to the two sets of coupled microbeam sensor arrays in case (a) and (b). Table 5.2 shows the responsivities for each sensor of the coupled system (the diagonal elements of the responsivity matrix S_{rr}) as well as the responsivities of the corresponding sensors of the uncoupled system. In case (a) the responsivities for the coupled system are close to the corresponding responsivities of the uncoupled system. This is attributed to strong localization of the microbeam modes. In case (b), however, the coupled system's responsivities are significantly less than the uncoupled system responsivities since the resonance frequencies are much more closely spaced and resulting modes, of the coupled system, are less localized. It is important to note that, due to the nature of the coupling, the coupled system

will always have responsivities that are less than the uncoupled system. However, by tailoring the frequency response to have strongly localized modes, the responsivities of the coupled system will be close to those of the uncoupled system.

5.5 Frequency Resolution

The detection of small frequency shifts is limited by noise in an actual measurement. Thermal-mechanical noise has been suggested to be the ultimate limit of detection for micro- and nano- mechanical resonators [29, 43, 120], under the assumption that other frequency sources can be made small. The effect of thermal-mechanical noise on the minimum detectable frequency shift (frequency resolution) for a single-degree-of-freedom (SDOF) oscillator has been previously quantified in [42] using spectral density methods. Here, the frequency resolution due to thermal-mechanical noise is derived using two useful statistical techniques, the maximum likelihood function and the Cramer-Rao inequality. This figure of merit is first derived for a single microresonator and then used to approximate the frequency resolution for the SISO microresonator array for comparison purposes. Finally, the framework for the full derivation for the frequency resolution of the SISO microresonator array is presented and subsequently left for future work.

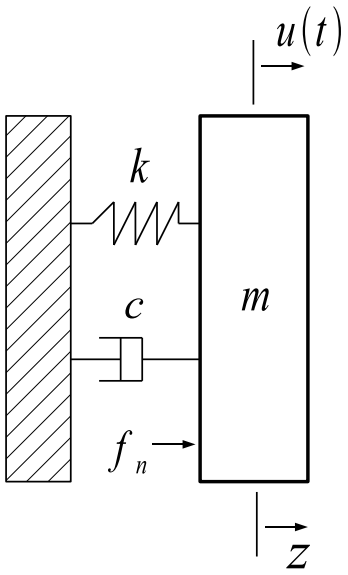

Figure 5.4: Schematic of a forced SDOF harmonic oscillator with a random force f_n, which is due to thermal-mechanical noise.

5.5.1 Uncoupled Microresonators

A harmonically forced SDOF oscillator having mass m, damping coefficient c, spring constant k, and driving force $u(t) = U_0 \cos \omega t$ is shown in Figure 5.4. By the Fluctuation-Dissipation Theorem [27, 48], since there is a dissipative force, $c\dot{z}$, it follows that a corresponding fluctuating force is present, f_n. In the case of microresonator based sensors, this random force is due to nonzero temperature in the surrounding environment, which results in thermal agitation (i.e. Brownian motion). The equation of motion for this system is

$$\ddot{z} + \frac{c}{m}\dot{z} + \frac{k}{m}z = \frac{1}{m}(u(t) + f_n). \tag{5.16}$$

This mechanical system can store energy in the form of kinetic energy, $\frac{1}{2}m\dot{z}^2$, and potential energy, $\frac{1}{2}kz^2$. Assuming that these energy storage modes are in thermal equilibrium, then by the Equipartitian Theorem [115], each energy storage mode has a mean energy of $\frac{1}{2}k_BT$, where $k_B = 1.38 \times 10^{-23} J/K$ is Boltzmann's constant and T is the temperature of the surrounding environment. In other words,

$$\frac{1}{2}kEz^2 = \frac{1}{2}k_BT$$
$$\frac{1}{2}mE\dot{z}^2 = \frac{1}{2}k_BT,$$

where Ez^2 and $E\dot{z}^2$ represent the mean squared displacement and velocity fluctuations, respectively. So, in the unforced case, $u(t) = 0$, the thermal noise will induce displacement and velocity fluctuations that will peak very close to the oscillator's resonance frequency. The covariance of the random force is $r = 2k_BTc$ [48], where the units of r are $[N^2/Hz]$.

In the following derivation we will need an expression for the likelihood function [66, 11] of a continuous time estimation problem with a stochastic differential equation of the form

$$dy = \theta\varphi dt + dv \tag{5.17}$$

where v is a Wiener process with incrimental covariance $Edv^2 = rdt$, φ a regression variable, and θ the unknown parameter. To obtain the likelihood function we first

consider the discretized version of Equation (5.17)

$$\Delta y_i = \theta \varphi_i \Delta t + e_i \tag{5.18}$$

where e_i are Gaussian $N(0, \sigma^2)$ random variables. The logarithm of the likelihood function is

$$-\log L = \frac{1}{2\sigma^2} \sum_{i=1}^{N} \left(\Delta y_i - \theta \varphi_i \Delta t\right)^2 . \tag{5.19}$$

Assuming that $\sigma^2 = r\Delta t$, we get

$$-\log L = \frac{1}{2r\Delta t} \sum_{i=1}^{N} \left(\Delta y_i - \theta \varphi_i \Delta t\right)^2 . \tag{5.20}$$

Taking the limit as Δt goes to zero gives Equation (5.17). In the limit the log likelihood function becomes

$$-\log L = \frac{1}{2rdt} \int \left(dy - \theta \varphi dt\right)^2 . \tag{5.21}$$

We now apply the maximum likelihood method to the harmonically driven oscillator and assume that z, $\dot{z}$, and $u(t)$ are measurable quantities. Equation (5.16) can be expressed as a stochastic differential equation similar to Equation (5.17)

$$dy = \theta_1 x_1 dt + \theta_2 x_2 dt + \theta_3 x_3 dt + de \tag{5.22}$$

where $\theta_1 = -k/m$, $\theta_2 = -c/m$, $\theta_3 = 1/m$, $x_1 = z$, $x_2 = \dot{z}$, $x_3 = u$, $dy/dt = dx_2/dt$, and e is a Wiener process with incremental covariance $Ede^2 = r/(m^2)dt$ and mean $Ede = 0$. The maximum likelihood method is applied to estimate the above

parameters. By assuming that the random variable de has a gaussian distribution and that parameters θ_1, θ_2, and θ_3 are known, the maximum likelihood function L can be expressed as

$$-\log L = \frac{1}{2\sigma^2}\int_0^{T_m} de^2 = \frac{m^2}{2rdt}\int_0^{T_m}(dy - \theta_1 x_1 dt - \theta_2 x_2 dt - \theta_3 x_3 dt)^2 \qquad (5.23)$$

where T_m is the measurement time and σ is the standard deviation. The maximum likelihood estimates of parameters θ_1, θ_2, and θ_3 are the values of these parameters that maximize the likelihood function L, therefore minimizing $\log L$ (5.23). Here the maximum likelihood estimate of θ_1 is of specific interest. In 1946, Cramer [32] showed that there is a lower bound to the variance (precision) of an unbiased estimator which is given by

$$cov(\hat{\theta}) = E(\hat{\theta} - \theta_0)(\hat{\theta} - \theta_0)^T \geq J^{-1} \qquad (5.24)$$

where $\hat{\theta}$ is a matrix composed of the estimated parameters, θ_0 is a matrix composed of the mean of each of the parameters, and J is Fisher's information matrix. Equation (5.24) is known as the Cramer-Rao inequality. The Fisher information matrix J is the gradient of the likelihood function

$$J = E(\log L)_\theta (\log L)_\theta^T = -E(\log L)_{\theta\theta}. \qquad (5.25)$$

In matrix form, Equation (5.25) is

$$J = E\begin{pmatrix} \frac{d^2}{d\theta_1^2}\log L & \frac{d^2}{d\theta_1 d\theta_2}\log L & \frac{d^2}{d\theta_1 d\theta_3}\log L \\ \frac{d^2}{d\theta_1 d\theta_2}\log L & \frac{d^2}{d\theta_2^2}\log L & \frac{d^2}{d\theta_2 d\theta_3}\log L \\ \frac{d^2}{d\theta_1 d\theta_3}\log L & \frac{d^2}{d\theta_2 d\theta_3}\log L & \frac{d^2}{d\theta_3^3}\log L \end{pmatrix} . \tag{5.26}$$

Plugging Equation (5.23) into Equation (5.26), the Fisher information matrix becomes

$$J = \frac{m^2}{r}\int_0^{T_m}\begin{pmatrix} x_1 \\ x_2 \\ x_3 \end{pmatrix}\begin{pmatrix} x_1 & x_2 & x_3 \end{pmatrix} dt = \frac{m^2 T_m}{r} E\begin{pmatrix} x_1 \\ x_2 \\ x_3 \end{pmatrix}\begin{pmatrix} x_1 & x_2 & x_3 \end{pmatrix} . \tag{5.27}$$

To determine J the superposition principle is used to analyze the deterministic and stochastic part of Equation (5.22) separately. This is valid because Equation (5.22) is linear.

The deterministic part of x_1, x_2, and x_3 can be described in vector form as

$$\begin{pmatrix} x_1 \\ x_2 \\ x_3 \end{pmatrix} = \begin{pmatrix} G(i\omega) \\ i\omega G(i\omega) \\ 1 \end{pmatrix} U_0 \tag{5.28}$$

where U_0 is the forcing amplitude and $G(i\omega)$ is the transfer function at driving frequency ω. The variance of Equation (5.28) is

$$E\begin{pmatrix} x_1 \\ x_2 \\ x_3 \end{pmatrix}\begin{pmatrix} x_1 & x_2 & x_3 \end{pmatrix} = \frac{U_0^2}{2}\begin{pmatrix} |G(i\omega)|^2 & 0 & Re[G(i\omega)] \\ 0 & \omega^2|G(i\omega)|^2 & Re[i\omega G(i\omega)] \\ Re[G(i\omega)] & Re[i\omega G(i\omega)] & 1 \end{pmatrix} . \tag{5.29}$$

The transfer function for the system is

$$G(i\omega) = \frac{(k - m\omega^2) - ic\omega}{(k - m\omega^2)^2 + \omega^2 c^2}. \tag{5.30}$$

Assuming that the oscillator is driven at its natural frequency, $\omega_0 = \sqrt{k/m}$, Equation (5.29) becomes

$$E \begin{pmatrix} x_1 \\ x_2 \\ x_3 \end{pmatrix} \begin{pmatrix} x_1 & x_2 & x_3 \end{pmatrix} = \frac{U_0^2}{2} \begin{pmatrix} \frac{m}{kc^2} & 0 & 0 \\ 0 & \frac{1}{c^2} & \frac{1}{c} \\ 0 & \frac{1}{c} & 1 \end{pmatrix} . \tag{5.31}$$

The equation of motion for the stochastic portion of Equation (5.22) is

$$\begin{pmatrix} dx_1 \\ dx_2 \end{pmatrix} = \begin{pmatrix} 0 & 1 \\ -\frac{k}{m} & -\frac{c}{m} \end{pmatrix} \begin{pmatrix} x_1 \\ x_2 \end{pmatrix} dt + \begin{pmatrix} 0 \\ de \end{pmatrix} , \tag{5.32}$$

where the vector $X = (x_1, x_2)$ has covariance $P(t) = EX(t)X(t)^T$. In steady state the covariance equation for this system is given by

$$AP + PA^T + R = 0 \tag{5.33}$$

where

$$A = \begin{pmatrix} 0 & 1 \\ -\frac{k}{m} & -\frac{c}{m} \end{pmatrix} ,$$

and

$$R = \begin{pmatrix} 0 & 0 \\ 0 & \frac{r}{m^2} \end{pmatrix} .$$

Solving for P in Equation (5.33) gives the variance due to the thermal fluctuations

$$E\begin{pmatrix} x_1 \\ \\ x_2 \end{pmatrix}\begin{pmatrix} x_1 & x_2 \end{pmatrix} = \begin{pmatrix} \frac{k_BT}{k} & 0 \\ \\ 0 & \frac{k_bT}{m} \end{pmatrix} . \tag{5.34}$$

Combining Equations (5.31) and (5.34) by superposition and plugging the result into Equation (5.27), the Fisher information matrix becomes

$$J = \frac{m^2T_m}{r}\begin{pmatrix} \left(\frac{k_BT}{k} + \frac{U_0^2m}{2kc^2}\right) & 0 & 0 \\ \\ 0 & \frac{k_BT}{m}\frac{U_0^2}{2c^2} & \frac{U_0^2}{2c} \\ \\ 0 & \frac{U_0^2}{2c} & \frac{U_0^2}{2} \end{pmatrix} . \tag{5.35}$$

It is important to note that Equation (5.35) is in block diagonal form, which greatly simplifies the inverse of the matrix. Taking the inverse of Equation (5.35) gives a lower bound to the variance of θ_1, θ_2, and θ_3, by the Cramer-Rao inequality (5.24). In this analysis the variance of θ_1 (which equals k/m) is of specific interest since it is directly related to the resonance frequency. The lower bound variance of k/m is

$$\sigma_{k/m}^2 = \frac{2k_BTc}{m^2T_m}\left(\frac{k_BT}{k} + \frac{U_0^2m}{2kc^2}\right)^{-1} \tag{5.36}$$

where $\sigma_{k/m}$ is the standard deviation of the parameter k/m. The smallest measurable frequency shift or frequency resolution of a harmonically driven oscillator in the presence of thermal-mechanical noise is thus

$$\sigma_{\omega_0} = \left(\frac{\omega_0}{T_mQ}\right)^{\frac{1}{2}}\left(\frac{k_BT}{2k_BT + kx_c^2}\right)^{\frac{1}{2}} \tag{5.37}$$

where it is assumed that the cantilever is driven at its resonance frequency ω_0, that the drive amplitude is $U_0 = x_c\omega_0 c$, and that x_c is the critical oscillation amplitude just below the onset of nonlinearity. (Note that $x_c \approx 0.53t$ for a fixed-fixed microbeam [42].) Notice that the frequency fluctuations decrease as Q increases and T_m increases as expected. Also, there is a term in Equation (5.37) that represents the ratio of thermal energy $E_t = k_B T$ to carrier energy $E_c = kx_c^2$. This term is essentially the inverse of the signal to noise. A more convenient way to write Equation (5.37) is

$$\frac{\sigma_{\omega_0}}{\omega_0} = \left(\frac{1}{\pi N Q}\right)^{\frac{1}{2}} \left(\frac{E_{th}}{2E_{th} + E_c}\right)^{\frac{1}{2}} \tag{5.38}$$

where $N = w_0 T_m/2\pi$ represents the number of periods in the frequency measurements. The carrier energy can also be expressed as $E_c = m\omega_0^2 x_c^2$. Equation (5.38) can be simplified by assuming that the thickness of small cantilevers is nanometer scale or even sub-nanometer scale (i.e. $E_{th} \ll E_c$)

$$\frac{\sigma_{\omega_0}}{\omega_0} \approx \left(\frac{1}{\pi N Q}\right)^{\frac{1}{2}} \left(\frac{E_{th}}{E_c}\right)^{\frac{1}{2}} \tag{5.39}$$

which turns out to be the same expression derived for a frequency measurement by a phase locked loop in [42]. In their derivation, however, they use a spectral density method to derive the frequency resolution, which differs from the approach used herein.

5.5.2 Coupled Microresonators

Equation (5.39) can be adopted to gain an initial understanding of how the frequency resolution of the coupled system compares to the uncoupled system. Consider a localized microbeam mode in the response of the shuttle mass of the coupled system with effective quality factor Q_{eff}, effective mass m_{eff}, resonance frequency Ω_{sm}, and shuttle mass vibration amplitude x_{sm}. Equation (5.39) can be rewritten as

$$\frac{\sigma_{\Omega_{sm}}}{\Omega_{sm}} \approx \left(\frac{1}{\pi N Q_{eff}}\right)^{\frac{1}{2}} \left(\frac{k_B T}{m_{eff}\Omega_0^2 x_{sm}^2}\right)^{\frac{1}{2}}. \tag{5.40}$$

One of the main limitations of the SISO multi-analyte sensor is the inherently small amplitude of the resonance peaks in the shuttle mass response, which is a result of the large size of the shuttle mass relative the the size of the microbeams. This is evident in Figure 5.2, where the response of the each localized microbeam at resonance is larger than the corresponding resonance in the shuttle mass response. Due to the small resonant amplitudes in the shuttle mass response, the coupled system is expected to have lower frequency resolution than the uncoupled system since Equation (5.40) is inversely proportional to the amplitude at resonance. This Expression gives a good initial understanding of how the amplitude of the coupled system limits the frequency resolution and is helpful for designing the response the SISO coupled array to achieve optimum sensitivity.

It is important to note that this expression assumes that the coupled system's resonance is Lorentzian. The coupling in the system, however, causes a frequency null near each localized resonance as seen in Figure 5.2. While this is believed to be a reasonable approximation, a more thorough treatment is necessary to fully understand how the system parameters effect the frequency resolution of the coupled system.

5.5.3 On Going Work

Current efforts are aimed at deriving a frequency resolution metric for the SISO coupled microresonator array using the above techniques. Here the framework is for the derivation is detailed for a system compose a shuttle mass an a single microbeam sensor.

A MDOF oscillator consisting of a large mass m with stiffness k and viscous damping c attached to a smaller mass m_1 with stiffness k_1 and viscous damping c_1 is shown in Figure 5.5. The large mass is driven by a force $u(t) = U_0 \cos \omega t$ and the response of the shuttle mass is used to measure the resonance frequency of the localized mode of the smaller mass m_1. Since there are two dissipative mechanisms in this system, c and c_1, there are two corresponding fluctuating forces, f_n and

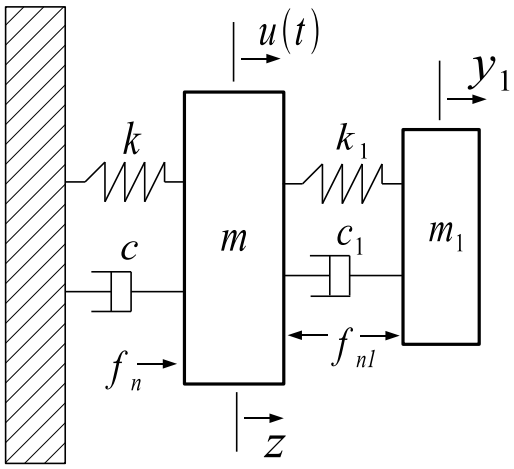

Figure 5.5: Schematic of a forced SDOF harmonic oscillator with a random forces f_n and f_{n1}, which are due to thermal-mechanical noise

f_{n1}. The coupled equations of motion for this system are

$$\ddot{z}+\frac{\omega_b}{Q_b}\dot{z}+\omega_b^2 z+\frac{m_1}{m}\frac{w_1}{Q_1}(\dot{z}-\dot{y_1})+\frac{m_1}{m}\omega_1^2(z-y_1)=\frac{1}{m}(u(t)+f_n-f_{n1})$$
$$\ddot{y_1}+\frac{\omega_1}{Q_1}(\dot{y_1}-\dot{z})+\omega_1^2(y_1-z)=\frac{1}{m_1}f_{n1}, \tag{5.41}$$

where $\omega_b = k/m$, $Q_b = m\omega_b/c$, $\omega_b = k_1/m_1$, and $Q_1 = m\omega_1/c_1$. Equation (5.41) can be expressed as

$$dx_2=(\theta_1+\frac{m_1}{m}\theta_4)x_1dt+(\theta_2+\frac{m_1}{m}\theta_5)x_2dt+\theta_3x_3dt-\frac{m_1}{m}\theta_6x_4dt-\frac{m_1}{m}\theta_7x_5dt+de_1-de_2$$
$$dx_5=-\theta_4x_1dt-\theta_5x_2dt+\theta_6x_4dt+\theta_7x_5dt+de_3 \tag{5.42}$$

where $\theta_1 = -\omega_b^2$, $\theta_2 = -\omega_b/Q_b$, $\theta_3 = 1/m$, $\theta_4 = \theta_6 = -\omega_1^2$, $\theta_5 = \theta_7 = -\omega_1/Q_1$, $x_1 = z$, $x_2 = \dot{z}$, $x_3 = u(t)$, $x_4 = y_1$, and $x_5 = \dot{y_1}$. The Wiener Processes e_1, e_2, and e_3 have incremental covariances $Ede_1^2 = r_1/m^2dt$, $Ede_2^2 = r_2/m^2dt$, and

$Ede_3^2 = r_2/m_1^2 dt$, respectively, where $r_1 = 2k_BTc$ and $r_2 = 2k_BTc_1$, and all have zero mean ($Ede_1 = Ede_2 = Ede_3 = 0$). Also note that de_2 is related to de_3, specifically $de_2 = (m1/m)de_3$. The random forces can be written in vector form as

$$d\epsilon = \begin{pmatrix} de_1 - de_2 \\ \\ de_3 \end{pmatrix} \tag{5.43}$$

which has incremental covariance $E(d\epsilon d\epsilon^T) = \Gamma dt$ and zero mean, where the covariance matrix Γ is

$$\Gamma = \begin{pmatrix} \frac{r_1+r_2}{m^2} & -\frac{r_2}{m_1 m} \\ \\ -\frac{r_2}{m_1 m} & \frac{r_2}{m_1^2} \end{pmatrix} \quad . \tag{5.44}$$

The Logarithm of the Likelihood function is

$$-\log L = \frac{1}{2}\int_0^{T_m} d\epsilon^T \Gamma^{-1} d\epsilon. \tag{5.45}$$

By using the Fisher information matrix and the Cramer-Rao inequality, the frequency resolution of resonance corresponding to the localized microbeam mode can be determined. More microbeams can be incorporated into this derivation, and numerical methods can be used to investigate the effects of the parameters on the system's frequency resolutions.

5.6 Scaling

As previously discussed the mass sensitivity of a resonant sensor depends on the inverse of the mass responsivity. In order to increase the mass sensitivity the

mass responsivity can be increased by decreasing the dimensions of the resonator. Not surprisingly, nanomechanical resonators have shown unprecedented sensitivities due to their ultra small masses and high resonance frequencies [143]. Reducing the resonator dimensions, however, also leads to a reduction in detectability. A metric can be defined that takes into account the detectability, which will be referred to as the detectability product [2]

$$\mathcal{D} = R\mathcal{R}^{-1}, \tag{5.46}$$

where R is the mass responsivity and $\mathcal{R}^{-1}$ is the detectability, which will depend on the transduction method of the sensor.

Consider, for example, the case where the resonator's mechanical motion is transduced into an electrical signal using a standard optical interferometric detection technique (i.e. Michelson interferometry). When the width of the resonator becomes smaller than wavelength of the laser (He-Ne laser $\lambda \approx 632nm$) there is a significant reduction in signal strength [69, 80], which reduces the signal-to-noise ratio. This ultimately leads to a reduction in the detectability. In many cases, it is therefore desirable to have a larger sensor surface. There is a trade-off, however, in that larger sensor dimensions generally increase the effective mass and therefore decrease the mass responsivity of the sensor. In this section the sensor topology discussed previously is shown to have unique scaling benefits in terms sensitivity and detectability.

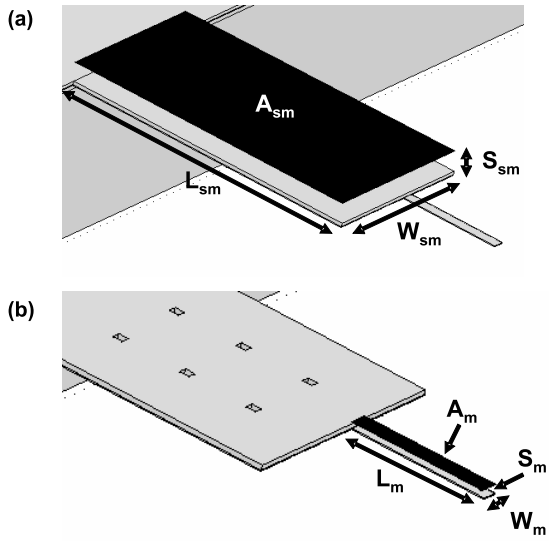

Figure 5.6: Schematics of a microbeam coupled to a large shuttle mass depicting (a) a capacitive plate with area A_{sm} for sensing the motion of the shuttle and (b) a capacitive plate with area A_m for sensing the motion of the microbeam.

In this section the capacitive transduction case is considered for a device analogous to the the coupled architecture previously discussed in Section 5.1. Two transduction methods are shown in Figure 5.6 for the device which is composed of a resonator with width W_m and length L_m (smaller cantilever) and a shuttle mass with width W_{sm} and length L_{sm}(larger cantilever). In the first case (Figure 5.6a), the larger shuttle mass is used for transduction, with effective capacitor plate area $A_{sm} = l_{sm}w_{sm}$, to indirectly sense the resonance of the smaller cantilever. In the second case (Figure 5.6b), with effective capacitor plate area $A_m = l_m w_m$, the smaller cantilever is used for transduction to directly sense its own resonance. In

both of these cases the coupled system is driven near the localized mode where energy is largely confined to the resonator.

For capacitive transduction, the detectability can be quantified by the inverse of the motional resistance [13, 96, 97]. The motional resistance relates the voltage at the input of the transducer v_i to the current at the output of the transducer i_o by $\mathcal{R} = v_i/i_o$. Assuming that the sensor is driven near the localized resonance of the resonator, ω_m, the motional resistances for the two cases in Figure 5.6 are

$$\mathcal{R}_{sm}^{-1} \approx \frac{\epsilon_0^2 V_{DC}^2}{c}\left(\frac{A_{sm}^2}{S_{sm}^4}\right), \tag{5.47}$$

$$\mathcal{R}_{m}^{-1} \approx \frac{\epsilon_0^2 V_{DC}^2}{c}\left(\frac{A_{m}^2}{S_{m}^4}\right), \tag{5.48}$$

where ϵ_0 is the permittivity of free space, c is the damping coefficient, V_{DC} is the DC voltage offset applied across the capacitor, and S_{sm} and S_m are the gaps between the top capacitor plate and the shuttle mass and microbeam, respectively. Here, for simplicity, the capacitors are assumed to act approximately as parallel plates and the damping coefficient is assumed to be approximately the same for each case. It is evident that the motional resistance strongly depends on the gap between the capacitive plates and the effective area of the capacitive plates.

Since the system is driven at a resonance frequency where the energy is localized in the smaller cantilever, the mass responsivity is assumed to be approximately equal to that of an identical isolated small cantilever. So, the mass re-

sponsivity for the device is approximately $R = \beta \frac{1}{L_m^3 W_m}$, where β is a constant that depends on the material properties and boundary conditions of the beam. This assumption is validated by the work detailed in Section 5.4. The ratio of the detectability products scale as

$$\mathcal{D}_{sm} \propto \left(\frac{1}{S_{sm}^4}\right)\left(\frac{l_{sm}^2 w_{Sm}^2}{L_m^3 W_m}\right), \tag{5.49}$$

$$\mathcal{D}_m \propto \left(\frac{1}{S_m^4}\right)\left(\frac{l_m^2 w_m^2}{L_m^3 W_m}\right). \tag{5.50}$$

Taking the ratio of Equations (5.49) and (5.50) gives

$$\frac{\mathcal{D}_{sm}}{\mathcal{D}_m} \propto \left(\frac{S_m^4}{S_{sm}^4}\right)\left(\frac{l_{sm}^2 w_{sm}^2}{l_m^2 w_m^2}\right). \tag{5.51}$$

or

$$\frac{\mathcal{D}_{sm}}{\mathcal{D}_m} \propto \left(\frac{S_m^4}{S_{sm}^4}\right)\left(\frac{A_{sm}^2}{A_m^2}.\right). \tag{5.52}$$

This ratio shows that the detectability product increases drastically when the resonant motion of a smaller cantilever is transduced through a larger intermediate shuttle mass. A detectability ratio greater than 1 implies that the case where the shuttle mass is the transducer will perform better in terms of responsivity and detectability than the case where the smaller resonator is the transducer. Due the to extremely small size scale of nanomechanical resonators the detectability product is drastically reduced due to ultra-small motional resistance. Therefore, the coupled architecture is an attractive platform for sensing nano-scale resonators

since it allows for increased motional resistance without significant reduction of mass responsivity.

Since the most pertinent metric for a mass sensor is the mass sensitivity, Equation (5.52) should be modified to include the frequency resolution, which was derived for a sensor limited by thermomechanical noise in the previous section. If the resonator shown in Figure 5.6 is driven at resonance, Equation (5.40) can be used as an estimate for the frequency resolution for each case in Figure 5.6. Assuming that the effective quality factor, effective mass, and measurement time (or number of periods in the measurement) are the same for both cases, the ratio of the frequency resolutions is $\sigma_{\Omega_{sm}}/\sigma_{\Omega_m} = x_m/x_{sm}$, where x_m and x_{sm} are the displacements of the resonator and shuttle mass, respectively. Accounting for the frequency resolutions, the modified detectability ratio is

$$\frac{\mathcal{D}_{sm}\sigma_{\Omega_{sm}}}{\mathcal{D}_m\sigma_{\Omega_m}} \propto \left(\frac{S_m^4}{S_{sm}^4}\right)\left(\frac{A_{sm}^2}{A_m^2}\right)\left(\frac{x_m}{x_{sm}}\right). \tag{5.53}$$

When the coupled sensor platform is driven at a localized mode the amplitude of the shuttle mass will inherently be less than the amplitude of the smaller resonator, $x_m > x_{sm}$. However, Equation (5.53) can still be made greater that 1 by scaling the shuttle mass appropriately.

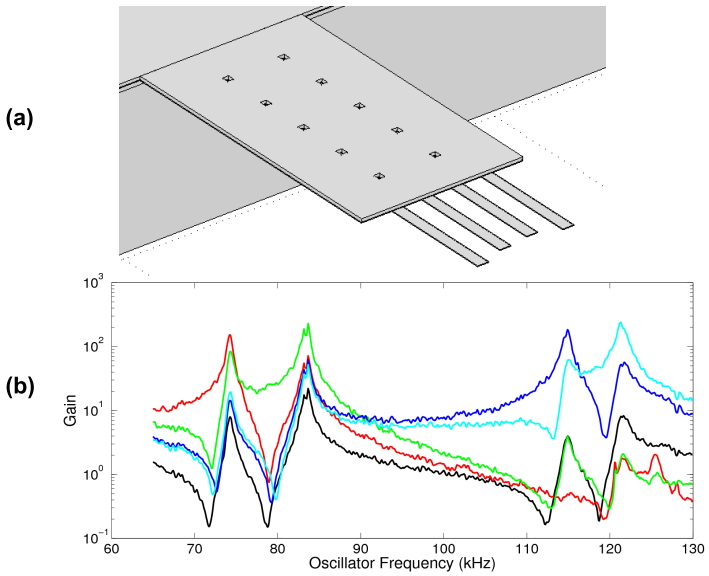

Figure 5.7: (a) CAD drawing of a device composed of a large shuttle mass and four frequency mistuned microbeams. (b) The response of the shuttle mass (black curve) and microbeams (colored curves), which was recorded experimentally using the technique discussed in Chapter 7. Notice the reduced amplitude of the four resonances in the shuttle mass response.

5.6.1 Example

As an example, consider the device, which will be revisited in Chapter 7, composed of a shuttle mass and four frequency mistuned microbeams shown in Figure 5.7a. The shuttle mass is approximately 334 μm long, 310 μm wide, and 5μm thick. The microbeams are 20μm wide, 1.3μm thick and they have mistuned lengths of 129.4μm, 123.4μm, 118.2μm, and 113.5μm. If the last half of the shuttle mass area is used for capacitive transduction, then the effective area squared is $A_{sm}^2 = 2.68 \times 10^{-15}\ m^4$. In the other case where each microbeam is used for

transduction, the effective areas squared would range from $A_m^2 = 1.29 \times 10^{-18}\, m^4$ to $A_m^2 = 1.67 \times 10^{-18}\, m^4$. In Figure 5.7(b), the response of the shuttle mass (black curve) and each of the microbeams (colored curves), obtained experimentally, are shown. Notice that at each of the four resonances, which correspond to localized modes where energy is largely confined to a single microbeam, the shuttle mass response is between 10 and 50 times smaller than the response of the corresponding microbeam. If the transducer gaps are assumed to be the same for each case $S_{sm} = S_m$, then the detectability product ratio from Equation (5.53) will be range between 32 and 200. Since the detectability ratios in this case are well above 1, the conclusion can be drawn that using the larger shuttle mass for transduction increases the performance of the sensor, even though there is inherent reduction in oscillator amplitude.

Chapter 6

SISO, Multi-Analyte Sensor - Proof-of-Concept

This chapter details a novel MEMS mass sensor that was developed using the theoretical framework presented in the previous chapter. Four frequency mistuned microbeams are commonly attached to a comparatively larger shuttle mass to allow for multiple chemical and/or biological analytes to be detected using a single input channel and a single output channel. This unique coupled architecture exploits vibration localization in the microbeam array to embed all requisite resonance frequency information in the response of the shuttle mass. As a result, the shuttle mass response can be used to measure resonant frequency shifts in each

of the microbeams. The prototype device in this section is used to experimentally study and prove the concept of the SISO multi-analyte mass sensor.

In Section 6.1 the unique SISO multi-analyte sensor design is presented. In the Section 6.2 the procedures used to fabricate and experimentally test the device are discussed. In Section 6.3 the unique response and mode shapes of this device are investigated experimentally and computationally (FEA). The results from a mass detection experiment, which verify this novel sensing concept, are presented in Section 6.4. Finally, the results from this experimental study and the sensor metrics are discussed in Section 6.5.

6.1 Sensor Design

Though a variety of geometries can be developed based on the sensor topology described in section 5.1, the translational design depicted in Figure 6.1 was selected for examination here due to its relative simplicity. The device shown in Figure 6.1 is analogous to the lumped mass model shown in Figure 5.1 and consists of a shuttle mass (SM) that is suspended above the substrate by four-folded beam flexures (S), four microbeam sensors labeled (M) that are attached to the shuttle mass, and a bank of interdigitated comb drives (CD) used for electrostatically actuating the device.

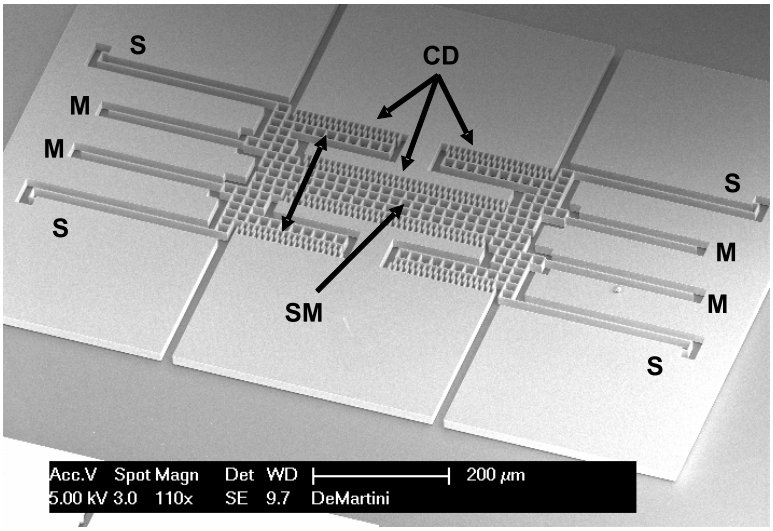

Figure 6.1: Scanning electron micrograph of the translational, SISO, multi-analyte sensor composed of a shuttle mass labeled SM, four individual microbeam sensors labeled M, four folded beam flexures labeled S, and electrostatic comb drives labeled CD. Note that the principle direction of motion is illustrated by the double-pointed arrow.

While there are two sets of comb drives, only one is utilized for actuating the device. The second set of comb drives, not utilized here, can be used for capacitively sensing the motion of the shuttle mass. Figure 6.2 depicts the comb drives and their dimensions. The comb fingers are approximately 2 μm wide, 15 μm long and are spaced approximately 2.5 μm apart with an overlap of 4 μm. In each comb drive set there are 70 comb finger interactions. The driving force $u(t)$ provided by these comb drives is described by Equation (5.4) in Section 5.1. The geometry and number of comb fingers were chosen to achieve a reasonable

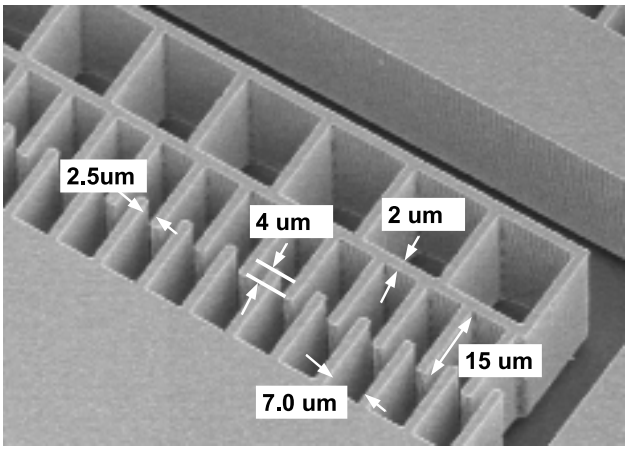

Figure 6.2: Interdigitated comb drives used for actuating the device, with labeled dimensions.

electrostatic force magnitude, approximately $5\,nN/V^2$, which ultimately allowed the device to be driven with relatively small voltages.

The folded beam flexures (see Figure 6.3) are designed in such a way that in-plane unidirectional motion is dominant. The primary direction of motion is labeled with the double ended arrow in Figure 6.1. The flexures are $280\,\mu m$ long, $2\,\mu m$ wide and have a $22\,\mu m$ fold and a $11\,\mu m$ fold, which effectively reduce cubic nonlinearities arising from spring hardening. As shown in [148] and in Table 2.2 of Section 2.2.1 the cubic nonlinearity of a flexure can be reduced by more than two orders of magnitude by including a single fold (crab-leg beam). Having a double fold is desirable in this application because the concept is based on linear principles. The combine linear stiffness of these four flexures is approximately

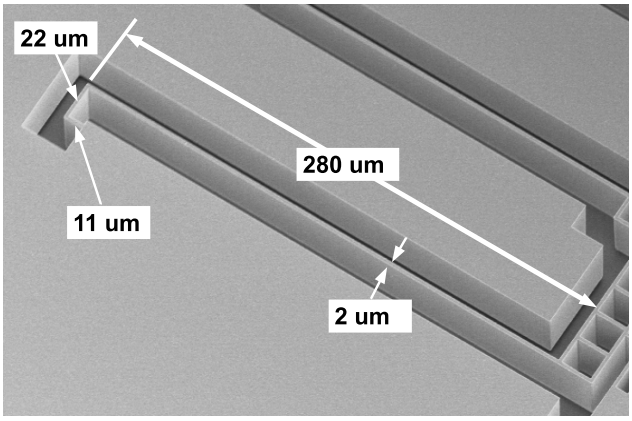

Figure 6.3: Double folded suspending flexure with labeled dimensions.

$4\,\mu N/\mu m$ and the cubic nonlinear stiffness is less than $0.01\,\mu N/\mu m^3$. Also note that the geometry of the flexures and shuttle mass, which has an approximate mass of $1.5 \times 10^{-9}\,kg$, were chosen so that the in-plane resonance frequency of the shuttle mass is well below the resonance frequencies of the microbeams. The resonance of the bulk in-plane translational mode can be approximated by

$$\Omega_{low} \approx \sqrt{\frac{k_s}{m_{sm}}},$$

where k_s is the in-plane stiffness of the flexures and m_{sm} is the mass of the shuttle mass. Note that this expression ignores the mass of the microbeams, which is a valid approximation for this design since the microbeams have much smaller masses than the shuttle mass. Also note that out of plane motion is suppressed by a large aspect ratio of flexure depth ($20\,\mu m$) to width ($2\,\mu m$).

The dimensions of the four microbeam sensors were chosen by using iterative finite element analysis (FEA) to ensure that their corresponding localized resonances were well separated from other resonant modes of the structure (FEA results are discussed later in this chapter). The four microbeam sensors are all $2\,\mu m$ wide and have mistuned lengths ($202.0\,\mu m$, $210.0\,\mu m$, $219.5\,\mu m$, and $230.2\,\mu m$). This provides a frequency spacing of approximately 4 kHz to ensure that the coupled system's resonant frequencies have ample separation and that the resulting modes are sufficiently localized. Since damping coefficients were difficult to estimate prior to experiment, the frequency spacing between microbeam resonances was chosen by using Equation (5.8) and assuming a conservative average Q-value of 10. If these microbeams are assumed to be isolated, their effective masses are approximately $5 \times 10^{-12}\,kg$, which correspond to their first resonant mode. The ratios of the microbeam masses to the mass of the shuttle, the inertia ratios, are less then 0.01. As shown in Chapter 5, small inertia ratios are also necessary to ensure sufficiently localized modes.

It should also be noted that in practice different active sensing surfaces would be deposited on each of the microbeam oscillators. This sensor was designed conservatively for proof-of-concept and therefore only incorporates four microbeams, however, this number could be easily expanded in future devices to facilitate the detection of a larger number of analytes.

6.2 Device Fabrication and Experimental Setup

The device in Figure 6.1 was fabricated on a silicon-on-insulator (SOI) wafer with a 20 μm device layer using standard micro-machining techniques [152]. The process flow included a lithographic step for pattern definition, a deep anisotropic silicon etch using a deep reactive ion etcher (DRIE), an O_2 reactive ion etch (RIE) for polymer removal, and finally a hydrofluoric acid wet etch to remove the silicon dioxide beneath the oscillator.

For this experiment one set of the interdigitated comb drives was used for electrostatic actuation. The substrate and device were grounded and a swept sine wave was applied to the drive electrode. The response of the shuttle mass was measured using a single beam laser vibrometer (Polytec) [133]. Since the vibrations of interest occurred in-plane (perpendicular to the laser beam), a 45^o mirror was cut into the silicon next to the shuttle mass using a focused ion beam (FEI 235FIB). The output from the vibrometer, which is directly proportional to velocity, was sent to a vector signal analyzer (Hewlett Packard 89410A) to obtain the frequency response of the shuttle mass. In the following experiments, the device was operated at a pressure of 275 $mTorr$ because poor quality factors were experienced at higher pressures, which severely reduced sensitivity and overall performance.

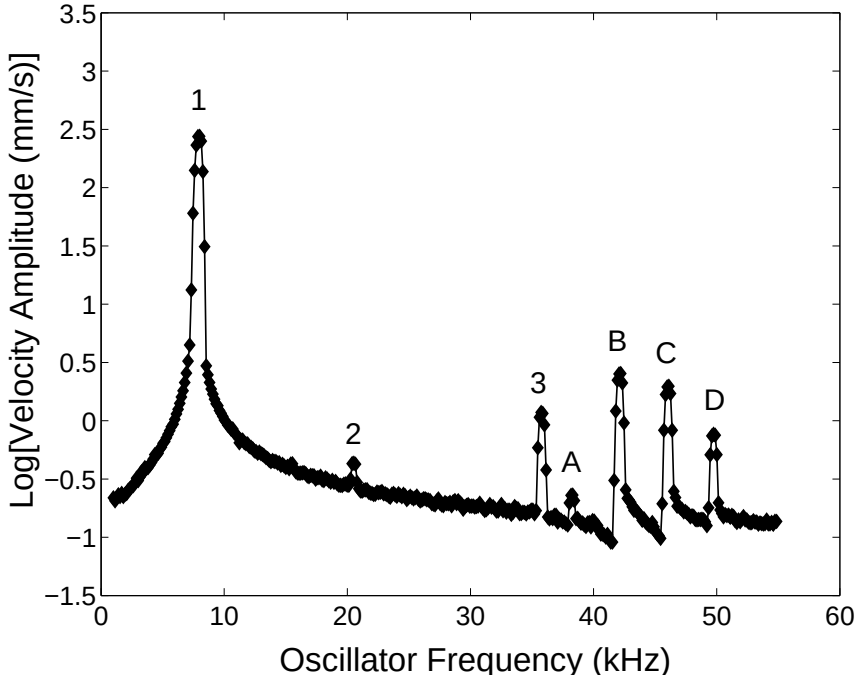

Figure 6.4: Experimentally obtained frequency response for the sensor depicted in Figure 6.1. The device was actuated with a 6.2 V swept sine signal in a 275 $mTorr$ envirnoment. Note that the labeled resonances correspond to the following modes: (1) bulk in-plane mode, (2 and 3) out-of-plane modes, and (A−D) modes where energy is localized in the sensors microbeams. The resonant frequencies associated with each of these modes are tabulated in Table 6.1.

6.3 Device Response and Mode Shapes

The response of the shuttle mass shown in Figure 6.4 was obtained experimentally by actuating the device with a 6.2V swept sine signal and sweeping frequency. The response contains the desired spectral features shown in Figure 5.2 (namely the resonances labeled (1) and (A) through (D)), as well as some that were not predicted with the lumped-mass model. The experimental resonance

labeled (1) occurs at approximately $8\,kHz$ and corresponds to the bulk in-plane mode where the entire device moves essentially together as a lumped mass. The mode shape at this resonance was predicted by FEA and the results are shown in Figure 6.5a. Higher frequency experimental resonances labeled (A)−(D) occur between approximately $38\,kHz$ and $50\,kHz$ (with a spacing of approximately $4\,kHz$) and correspond to the localized microbeam modes where the vibration energy is largely confined to a single microbeam. Figure 6.5b depicts the mode shape of one of these localized modes, specifically (D), predicted using FEA. All of these in-plane modes were verified using stroboscopic imaging equipment from Polytec and compared to the predicted modes from FEA. Two modes labeled (2) and (3) in Figure 6.4, which are not predicted by the lumped-mass model in Section 5.1, occur at approximately $20\,kHz$ and $36\,kHz$, respecively. These modes correspond to out-of-plane modes and are predicted and verified by FEA. Figure 6.5c depicts the characteristic shape of mode (3). Note that the frequency data for each of the system's resonances is tabulated in Table 6.1 for both the FEA and experimental results.

Another important observation to make is that resonance (3) occurs close to resonance (A), which results in a reduction of the resonant amplitude of (A). Due to the inherently small nature of the localized mode amplitudes, any further reduction in amplitude could be detrimental to the signal to noise ratio and therefore

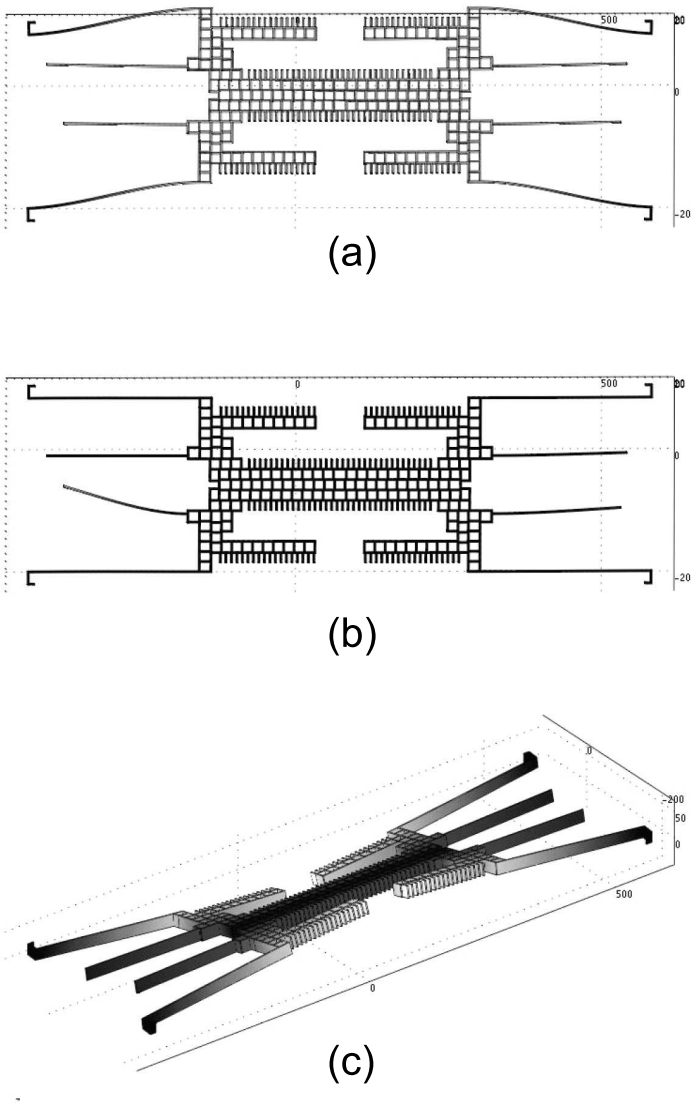

Figure 6.5: Three important mode shapes of the sensor determined using finite element software. (a) The first mode of the sensor: a bulk in-plane mode where the shuttle mass and microbeam oscillators move essentially as a lumped mass. (b) The seventh mode of the sensor: an in-plane, localized mode where energy is largely confined in a single microbeam. The fourth, fifth, and sixth modes show similar localized behavior but for different microbeams. (c) The third mode of the sensor: an out-of-plane torsional mode. The resonant frequencies corresponding to each of these modes are detailed in Table 6.1.

Table 6.1: Resonance frequencies determined through experiment and FEA for the device shown in Figure 6.1.

Mode	**Description**	**Experiment (kHz)**	**FEA (kHz)**	**Percent Error%**
1	Bulk translational mode	8.002	8.478	5.9
2	First out-of-plane mode	20.660	22.893	10.8
3	Second out-of-plane mode	35.877	40.335	12.4
4	First localized mode	38.301	41.435	8.2
5	Second localized mode	42.206	45.608	8.1
6	Third localized mode	46.112	49.594	7.6
7	Fourth localized mode	49.882	53.808	7.9
8	Third out-of-plane mode	–	59.226	–

the performance of the sensor in practical implementation. Future sensors should be carefully designed such that all unwanted modes are sufficiently separated from the modes of interest. When the device was operated in air (the response in air is shown in Figure 6.6) the localized resonance (A) completely disappeared and the other localized resonances exhibited poor quality. The response of this device is therefore unfit for operation in ambient conditions. The device's poor performance at ambient pressure is largely due to the increased damping caused by fluid pumping between the microbeam oscillators and the sidewalls of the device's substrate. In the second-generation device, discussed in Section 7, the device's performance in air is drastically improved by removing excess substrate material around the device and modifying the geometric configuration.

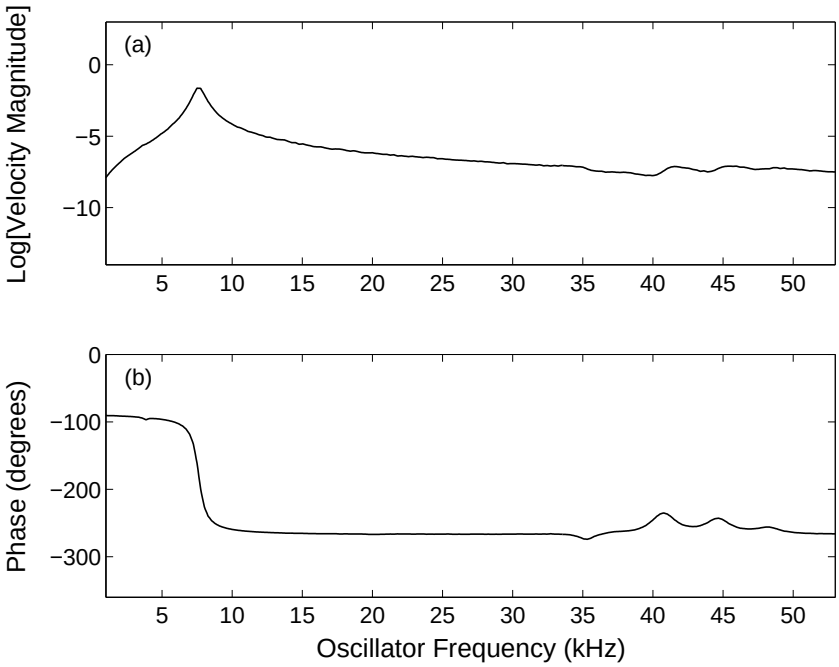

Figure 6.6: Experimentally obtained amplitude and phase response, measured using a laser vibrometer, of the translational SISO multi-analyte sensor when operated in air. Note that resonance (A) completely disappears.

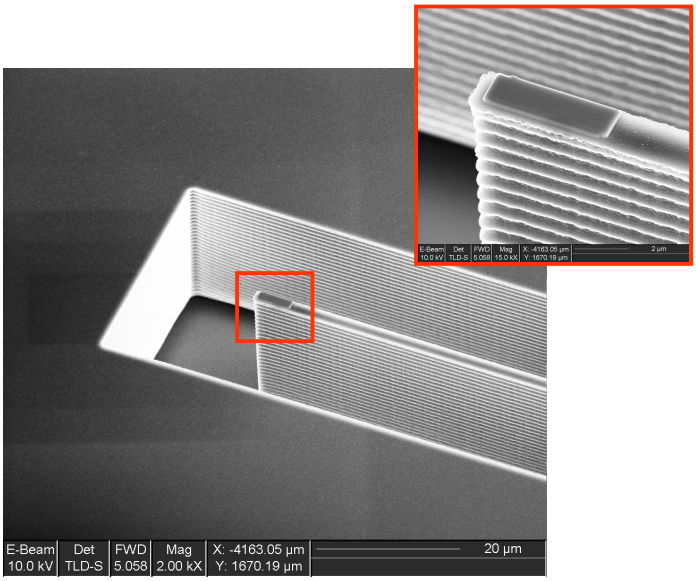

Figure 6.7: A scanning electron micrograph of the platinum patch added to the shortest, highest frequency microbeam to simulate mass detection. The patch measures approximately $1.57\,\mu m \times 5.10\,\mu m \times 0.22\,\mu m$ in size and has a mass of approximately $38\,pg$, which was computed volumetrically. The inset, which was used for measurement purposes, shows a zoomed in view of the patch.

6.4 Mass Detection Experiment

To simulate mass detection the frequency response of the shuttle mass was recorded before and after the deposition of a small patch of platinum onto the highest frequency microbeam. The platinum patch (shown in Figure 6.7) was deposited using a focused ion beam (FEI 235FIB). The patch dimensions were measured to be approximately $1.57\,\mu m \times 5.10\,\mu m \times 0.22\,\mu m$ using a scanning electron microscope. This yielded an approximate mass of $38\,pg$, which was esti-

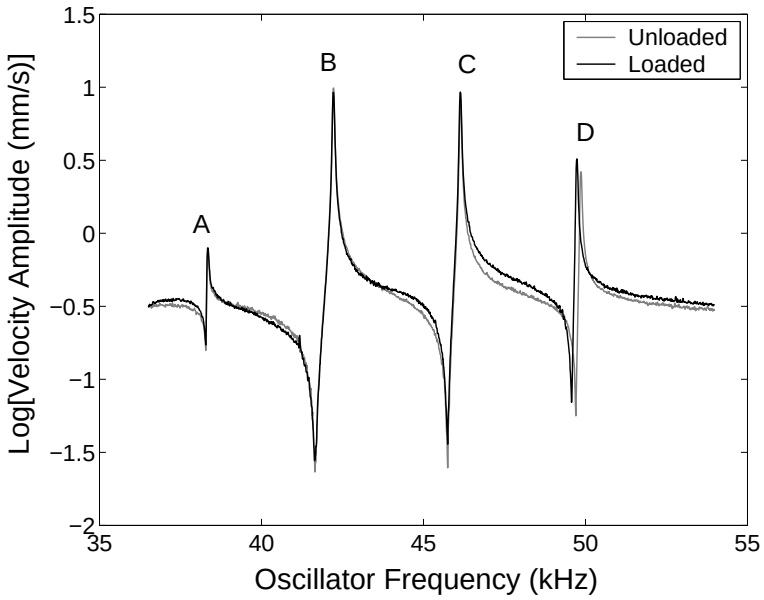

Figure 6.8: Experimentally obtained frequency response curves for the sensor depicted in Figure 6.1 for the unloaded device (grey curve) and for the device when the shortest beam was loaded by the platinum patch (black curve). The device was actuated with a $12.2\,V$ swept sine signal in a $275\,mTorr$ environment. Note that the added-mass loading introduces shifts in each of the systems resonances, the largest of which occurs in resonance (D), which corresponds to the localized mode of the loaded beam.

mated volumetrically. Note, this patch was added to the tip of the microbeam so that the effective stiffness was unaffected.

The responses of the shuttle mass measured before and after deposition (zoomed in on the four resonances corresponding to the localized microbeam modes) are shown in Figure 6.8. The device was actuated by a $12.2\,V$ swept sine signal in $275\,mTorr$ vacuum. It is apparent that resonance (D), the localized mode of the highest frequency (mass-added) microbeam, has been altered much more than

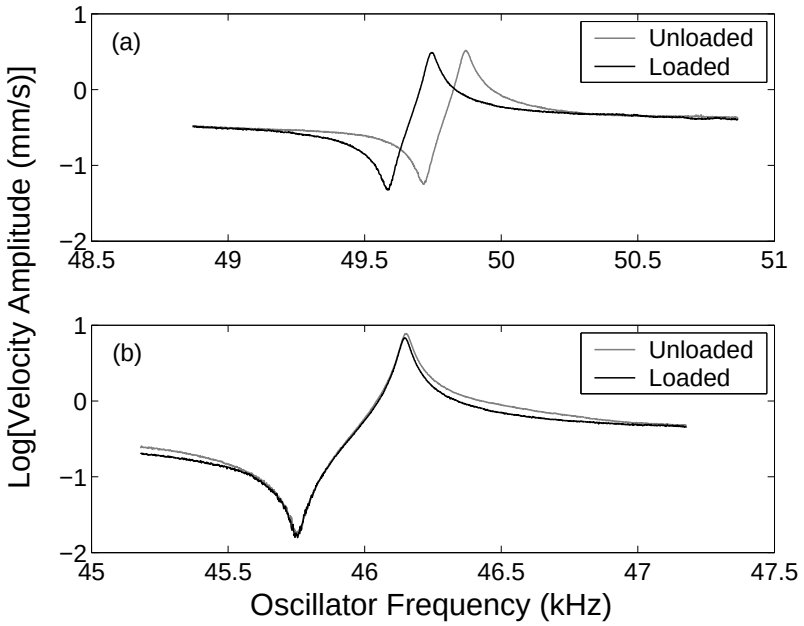

Figure 6.9: Experimentally obtained frequency responses for the sensor depicted in Figure 6.1 actuated with a 12.2 V swept sine signal in 275 $mTorr$ pressure depicting resonance shifts of approximately (a) 124 Hz near resonance D and (b) 3 Hz near resonance C. Note that the grey curves represent the response before mass loading and the black curves the response after mass loading the the shortest microbeam.

resonances (A) through (C). A higher resolution sweep near resonance (D), shown in Figure 6.9a, reveals a shift of 124 Hz. Performing the same high resolution sweep near resonance (C), shown in Figure 6.9b, reveals a much smaller shift of $3Hz$, which is 40 times smaller than that of the loaded microbeam. The markedly larger shift in the mass loaded microbeam resonance as compared to the unloaded microbeam resonances is a direct result of strong mode localization.

6.5 Discussion

Through this experiment, where mass detection was simulated by FIB depositing a small patch of platinum onto the tip of the shortest microbeam, the novel concept described in Chapter 5 was successfully proved. The structure of the prototype device shown in Figure 6.1 was designed in such a way that localized modes, where energy is largely confined to a single microbeam, occur in the device's response. Due to the localized nature of these modes, the added platinum on the shortest microbeam led to a frequency shift in the corresponding localized mode (highest frequency localized mode) that was much larger than the localized modes correponding to the unloaded microbeams, which are induced solely through coupling. These results verify that this device is capable of not only detecting mass addition, but also detecting the source of the mass addition.

The mass responsivity matrix **S** (discussed in Section 5.4) associated with the device shown in Figure 6.1 can be partially compiled using the experimental results detailed in the previous section. For example, the $(5, 5)$ element of the matrix, corresponding to the mass responsivity of resonance (D) in Figure 6.4 with respect to a mass addition to the highest frequency microbeam, can be computed to be $3.3\,Hz/pg$. The $(4, 5)$ element of the matrix, which is the mass responsivity associated with resonance (C) in Figure 6.4 computed with respect to a mass addition on the highest frequency microbeam, can be computed to be approximately $0.1\,Hz/pg$. Extending this procedure through further experimentation will reveal a diagonally dominant mass responsivity matrix, which is characteristic of a system with localized modes as discussed in Section 5.4.

The experimentally determined mass responsivity of the mass loaded microbeam is comparable to other reported values for resonant multi-analyte sensors. It is important to note, however, that these values are significantly lower than those reported for sensors based on isolated microresonators [62, 71, 143], mainly because of the larger scale of the devices considered here. While this can largely be rectified by device scaling in future devices, mass sensor arrays based on coupled system architectures will always be slightly inferior to arrays based on isolated mass sensors due to inter-oscillator coupling, which manifests itself in the off-diagonal terms of the responsivity matrix. Current design studies, the

results of which will be incorporated into next generation devices, are aimed at minimizing these off-diagonal terms while still allowing for the measurement of the response of a common shuttle mass that supports the individual sensor elements.

Many factors such as thermomechanical noise, absorption desorption noise, temperature fluctuations, and other sources of noise are known to affect the systems frequency resolution. In previous efforts, these factors have been studied in the context of single-degree-of-freedom resonant mass sensors [42]. To the author's knowledge, the effect of these noise contributions have not yet been studied for this type of coupled oscillator systems and ongoing and future efforts are aimed at resolving this important issue. For the current sensor system the frequency resolution is believed to be limited by the resolution of the spectrum analyzer and laser vibrometer system detailed in Section 6.2. As a result, a conservative frequency resolution estimate of $1.5Hz$, which is significantly larger than the smallest frequency shift measurable with the experimental setup, is assumed for each of the systems resonances. In its current experimental configuration this results in sub-picogram mass sensitivities for the sensor system. In final device implementations, however, additional improvements in hardware components, such as phase locked loops, may appreciably alter this resolution.

Chapter 7

SISO, Multi-Analyte Chemical Sensor

In the following section a device composed of four microbeam sensors commonly coupled to a comparatively larger microbeam that acts as the shuttle mass oscillator is presented. This device is designed to primarily operate out-of-plane with respect to the substrate and has been backside etched to remove the underlying substrate and eliminate squeeze film damping effects, which inhibited the device presented in Section 6 from operating successfully in air. The prototype device in this section represents the next step in the development of the SISO multi-analyte mass sensor. A functionalization apparatus was built to functionalize each of the four cantilevers with a different polymer coating, which

readily absorb volatile organic vapors. Toluene and methanol vapors, as well as toluene/methanol mixtures, are detected and identified using a single input signal and single output signal. This work is believed to represent the first experimental demonstration of SISO, multi-chemical detection and identification using a coupled array of microresonators. In addition, the localized microbeam modes are self-excited using positive feedback. This provides a means for tracking the localized microbeam resonances in real-time, while amplifying their effective quality factors. A mass sensitivity of 59 fg is demonstrated in air.

7.1 Sensor Design

A prototype sensor (Figure 7.1), composed of four microcantilever sensors S_1, S_2, S_3, and S_4, each attached to a common shuttle mass resonator SM (resembling a larger microcantilever), has been designed and fabricated for the detection of multiple organic vapors. A critical component in the design of the coupled system is that the frequency response contains tailored localized modes wherein the vibration energy is largely confined to a single microbeam sensor. The system was designed such that the resonances corresponding to these localized modes can be tracked through the shuttle mass using a single output signal. In practice, this was achieved by mistuning the lengths of the microbeam sensors and making their

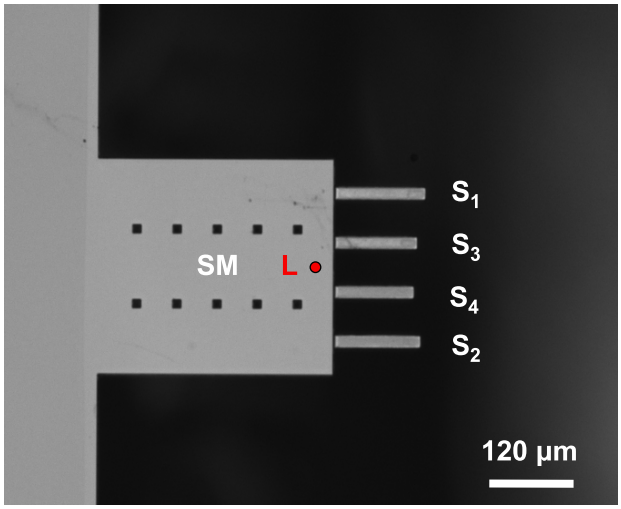

Figure 7.1: Microscope image depicting the sensor with labeled shuttle mass SM, microbeam sensors S_1, S_2, S_3, and S_4, and detection laser location L.

effective masses ($\approx 10^{-9}\ g$) small relative to that of the shuttle mass ($\approx 10^{-7}\ g$). The shuttle mass is approximately 334 μm long, 310 μm wide, and 5 μm thick. The microbeam sensors are approximately 20 μm wide and 1.3 μm thick and they have mistuned lengths of 129.4 μm, 123.4 μm, 118.2 μm, and 113.5 μm (S_1, S_2, S_3, and S_4, respectively).

The dimensions of this sensor where primarily chosen based on limitations placed by the procedure used to functionalize each microbeam. The method involved dipping the cantilever tips into 80 μm diameter capillary tubes containing polymer solutions (discussed further below). The diameter of the capillary tube placed limit on the center to center spacing between microbeams. The width of the microbeams and the width of the shuttle mass were chosen based on the

limit. The length of the microbeams were made long enough so that the last 25% of each beam (this ensured that the stiffness of the microbeams was largely unaffected by the coatings, which induce stress) could be accurately dipped into the tube with the positioning system, but small enough to achieve reasonably high mass responsivities. Further design considerations for this structure are provided in Appendix D.

Finite element analysis in conjunction with the model and design criteria discussed in Section 5.2 were used to tailor the device geometry and resulting frequency response so that the microbeam modes are sufficiently localized. In addition, finite element analysis helped to predict higher order modes not captured by the lumped-mass model and to make sure that there was ample frequency spacing to prevent contamination of the the localized microbeam modes. Figure 7.2 depicts the first seven modes predicted for the structure shown in Figure 7.1 using an eigenfrequency finite element analysis (COMSOL software [1]). This device is predicted to have a low frequency bulk out-of-plane mode (Figure 7.2a), four highly localized modes where the vibration energy is largely confined to a single microbeam (Figures 7.2b through 7.2e), a torsional mode (Figures 7.2f) occurring after the localized modes, and finally a (Figures 7.2g) second out-of-plane mode. The highly localized nature of the modes shown in Figures 7.2b through 7.2e verify that this structure is acceptable for SISO sensing. The resonance frequencies cor-

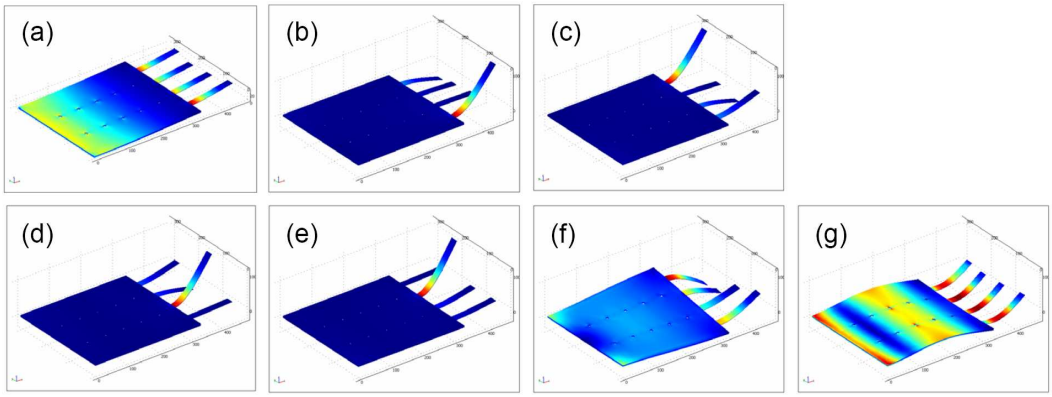

Figure 7.2: The first seven mode shapes of the sensor determined using finite element software. (a) The first mode of the sensor: a bulk out-of-plane mode where the shuttle mass and microbeam oscillators move essentially as a lumped mass. (b)−(e) The second through the fifth mode of the sensor: out-of-plane localized modes where energy is largely confined in a single microbeam. (f) The sixth mode of the sensor: an out-of-plane torsional mode. (g) The seventh mode of the sensor: a second bulk out-of-plane mode. The resonant frequencies corresponding to each of these modes are detailed in Table 7.1.

responding to each mode shown in Figure 7.2 are listed in Table 7.1. Note, there is ample spacing between each neighboring localized mode ($\approx 11\,kHz$ spacing), the first localized microbeam mode is well spaced from the first bulk out-of-plane mode ($48.4 kHz$ spacing), and the fourth localized microbeam mode is well spaced from the torsional mode ($27.7\,kHz$ spacing).

7.2 Device Fabrication

The device was fabricated on a silicon-on-insulator (SOI) wafer with a $5\,\mu m$ device layer, $1\mu m$ buried oxide layer, and $500\mu m$ handle. The process flow used to

Table 7.1: Resonance frequencies determined through experiment (see Section 7.6 for the experimental response used to determine these frequencies) and FEA for the device shown in Figure 7.1.

Mode	**Experimental Value (kHz)**	**FEA Value (kHz)**	**Percent Error%**
first bulk out-of-plane mode	54.3	55.8	2.3
localized microbeam mode (S_1)	102.3	104.2	1.9
localized microbeam mode (S_2)	114.3	115.6	1.1
localized microbeam mode (S_3)	126.4	126.6	0.2
localized microbeam mode (S_4)	136.7	137.0	0.2
first torsional mode	–	164.7	–
second bulk out-of-plane mode	–	372.5	–

fabricate the device is depicted in Figure 7.3. First, $500nm$ of silicon dioxide (SiO_2) is grown on the front and backside of the SOI wafer by wet thermal oxidation (Figure 7.3a). A 300 nm layer of silicon nitride (SiN_x) is deposited onto the backside of the wafer using plasma enhanced chemical vapor deposition (PECVD) to further protect the underlying Si during backside processing (Figure 7.3d). The frontside SiO_2 is patterned with positive photoresist and ICP reactive ion etched using CHF_3 plasma (Figure 7.3c). The frontside is patterned a second time with positive photoresist (Figure 7.3d). Next, a deep reactive ion etch (DRIE), using SF_6 as the etchant and C_4F_8 as the polymer passivation, was used to define the device (Figure 7.3e). The photoresist mask was then removed and a second DRIE step defined the thickness of the microbeam array (Figure 7.3f).

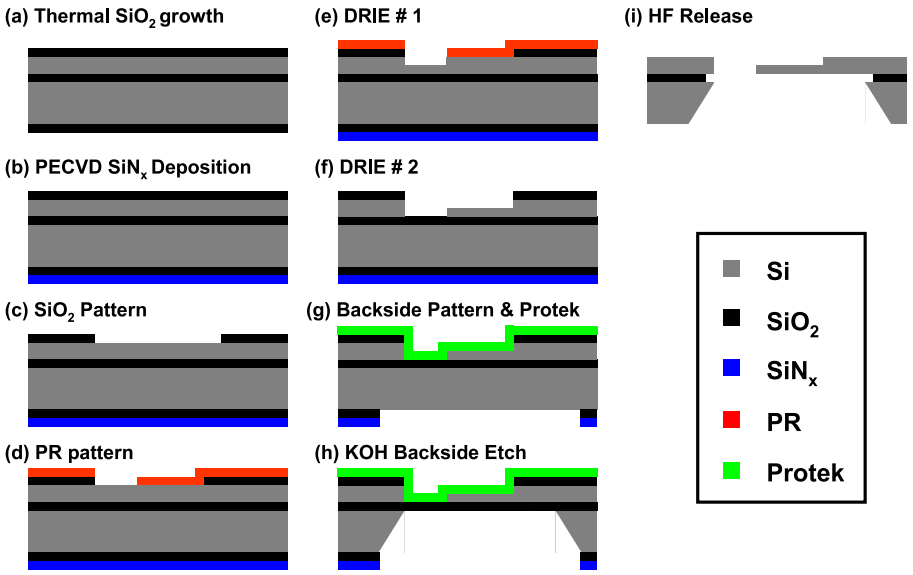

Figure 7.3: Process flow used to fabricate the device shown in Figure 7.1.

After processing the frontside, the backside was processed to remove the Si and SiO_2 layers beneath the device to eliminate squeeze film damping and effectively increase the system's quality factors. The backside vias were patterned with positive photoresist and the SiN_x and SiO_2 were reactive ion etched using CF_4 and CHF_3 plasmas, respectively (Figure 7.3(g)). To protect the frontside of the wafer during backside etching, a polymeric coating (Protek-B3 from Brewer Science) is spin-applied. The backside etch was carried out by placing the device into potassium hydroxide (KOH) at 80^oC until the buried oxide was reached (Figure 7.3(h)). Next, the Protek coating was removed by dipping the device into isopropanol, acetone, and finally deionized water baths. Lastly, a wet hydrofluo-

ric acid (HF) etch was used to remove the SiO_2 beneath the device layer (Figure 7.3(I)).

7.3 Polymers as functional Coatings

Standard polymers were used to functionalize each microbeam for detection and identification of chemical vapors. Polymers are known to readily absorb volatile organic compounds (VOCs) such as solvents, alcohols, fragrances, and nutrition-related compounds [12, 15, 72]. These analyte molecules, when present in the surrounding environment, will be absorbed into the polymers causing them to swell and the effective mass of the corresponding micrbeams to change. Analyte molecules will diffuse into the polymer layers until the absorption process reaches dynamic equilibrium, which will depend on the temperature and pressure of the surrounding environment. It is important to note that this process is reversible, in that when the analyte concentration in the surrounding environment is reduced the analyte residing inside the polymer will desorb.

Polymer coatings are not typically specific to a single organic vapor, however they are partially specific, in that the amount of vapor that a given polymer absorbs largely depends on the chemical makeup of the vapor (i.e. solubility properties and the saturation vapor pressure). As a result, an array of cantilevers

having different polymer coatings can be used to detect and identify previously measured analytes and analyte mixtures using pattern recognition techniques [72]. Due to the partial specificity, however, identifying the composition of analyte mixtures is difficult.

The partition coefficient is a measure of the amount of analyte molecules distributed between the vapor phase and the polymer phase [51, 55] at thermodynamic equilibrium. This constant is given by

$$K = \frac{c_v}{c_s}, \tag{7.1}$$

where c_v is the volume concentration of analyte in the vapor phase and c_s is the volume concentration of analyte in the polymer. It is important to note that the partition coefficient strongly depends on the chemistry of both the polymer and the analyte. The partition coefficient will also strongly depend on the vapor pressure of the analyte and the temperature T, which is given by the Gibbs free energy equation $\Delta G = -RT \ln K$, where R is the molar gas constant [51].

The resonance frequency shifts $\Delta\mathbf{f}$ in the coupled system for a given mass addition vector $\Delta\mathbf{m}$ (see Equation 5.10) are given by

$$\Delta\mathbf{f} \approx \mathbf{S}\Delta\mathbf{m},$$

where S is the mass responsivity matrix. For an N microbeam system, where each microbeam is coated with a different polymer coating, the elements in the mass

addition matrix $\Delta\mathbf{m}$ are given by

$$\Delta m_j = V_j M K_j c_v,$$

where $j = 1, 2, ..., N$, V_j is the volume of the polymer on the j^{th} microbeam, K_j is the partition coefficient of the polymer on the j^{th} microbeam for a given analyte, M is the molar mass of the analyte, and c_v is the the concentration of the analyte in the vapor phase. The frequency shift of the r^{th} (where $r = 1, 2, ..., N$) resonance is affected by absorption of a gaseous analyte vapor in each of the polymer coated microbeams (j)

$$\Delta f_r \approx \sum_{j=1}^{N} S_{rj} V_j M K_j c_v, \tag{7.2}$$

which are the elements of the frequency shift matrix $\Delta\mathbf{f}$. In other words, the frequency shift of one of the localized microbeam resonances will depend on the responsivity and the affinity of the polymer for a given analyte. For an array of isolated microbeams the resonance frequency shift due to absorption of a gaseous analyte vapor in the polymer layer is

$$\Delta f = -\frac{\omega_0}{2m_{eff}} V M K c_v. \tag{7.3}$$

It is important to note that in Equation (7.3), the polymer mass affects the the effective mass m_{eff} and therefore the sensitivity of the microbeam. The same holds for the effective masses of the microbeams in the coupled system, which directly affect the responsivity term S_{rj} in Equation (7.2). Prior to coating the microbeams

with polymers, it is therefore important to take into consideration the density of the polymer and the volume of polymer, V, in order to obtain optimum sensitivity and maintain ample frequency separation between the localized microbeam modes for the coupled system.

7.4 Sensor Functionalization

There are variety of methods for individually functionalizing the microbeam sensors. For instance, the microbeams could be coated by dipping them into capillary tubes with appropriate dimensions [71, 16], they could be spray coated using an ink-jet printer [55, 88, 16], or they could be coated using various lithography techniques, such as dip-pen lithography [50, 138]. While the later two methods allow for more precise volume control of functional coatings, the capillary tube method is adopted here due to its low cost and relative simplicity. This method proved to be sufficient for the experiments in this work.

To functionalize the microbeams for the detection of organic vapors, different polymer coatings (from Sigma Aldrich) were used. Table 7.2 shows the polymer solutions used to functionalize each microbeam. Polymer solutions with appropriate concentrations were prepared by mixing the polymers with solvents. Figure 7.4a shows the functionalizion apparatus that was built for dip coating the microbeam

Table 7.2: Polymers and solvents used for microbeam functionalization. Solution concentrations shown as mg polymer per mL solvent.

	Polymer	**Solvent**	**Concentration** ($\frac{mg}{mL}$)
S_1	Polymethylmethacylate	Toluene	1.5
S_2	Polystyrene	Toluene	1.2
S_3	Polyurethane	Dichloromethane	0.6
S_4	Poly(4-vinylpyridine)	Ethanol	5.0

tips into the polymer solutions. The functionalization procedure involved using a precision three axis (X,Y,Z) stage to accurately position the microbeam sensors and dip their tips into micro-capillary tubes ($80\mu m$ outer diameter) containing the corresponding polymer solutions. One end of the capillary tube is placed in a reservoir containing a polymer solution and capillary forces deliver the fluid to the free end where the microbeam is dip coated.

After dip coating each microcantilever into the corresponding polymer, the resonance frequency of each localized microbeam mode was recorded to determine the amount of polymer added and ensure that the modes remain well spaced. Figure 7.5 shows the resonance of each localized microbeam mode when all microbeams are unloaded (a), S_1 is functionalized with polymethylmethacylate (PMMA) (b), S_2 is functionalized with polystyrene (PS) (c), S_3 is functionalized with polyurethane (PU) (d), and S_4 is functionalized with poly(4-vinylpyridine) (PVP) (e). Note, when each microbeam is functionalized only the corresponding resonance shifts appreciably, this is evidence that these modes are strongly local-

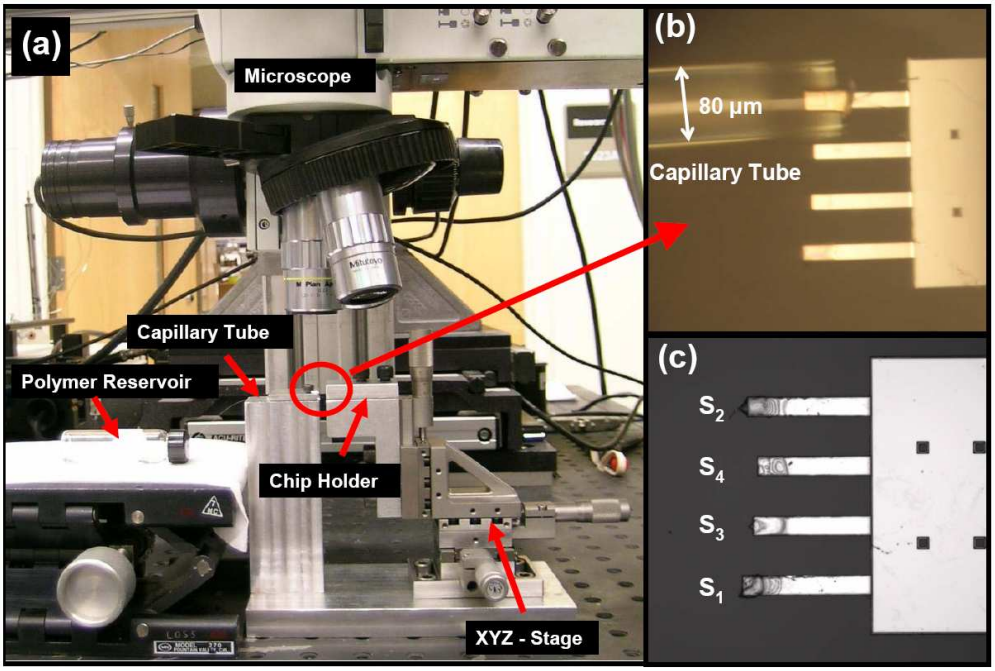

Figure 7.4: (a) The capillary tube apparatus used to functionalize the microbeam tips, (b) a close-up of a microbeam being dipped into a capillary tube containing a polymer solution, and (c) microscope image showing the four functionalized microbeams (note the polymers corresponding to each beam are listed in Table 7.2.

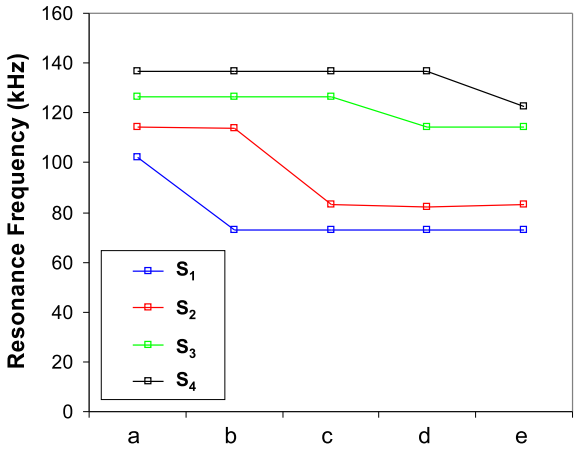

Figure 7.5: Resonance frequency of each localized mibrobeam mode when (a) all microbeams are unloaded, (b) S_1 is functionalized with PMMA, (c) S_2 is functionalized with PS, (d) S_3 is functionalized with PU, and (e) S_4 is functionalized with PVP.

ized. The polymer mass added to each microbeam was estimated (see Table 7.3) by using the frequency shift of each localized microbeam mode and the approximate effective masses of the microbeams. Also, it was assumed that the stiffness of each microbeam was largely unaffected by the polymer coatings, which was a reasonable assumption since the nearly stress free end portion of each microbeam was coated. The approximate added polymer mass to microbeam mass ratios are also shown in Table 7.3.

Table 7.3: Added polymer mass on each microbeam after functionalization procedure.

	Polymer	**Added Mass (ng)**	**Added Mass/Microbeam Mass (ng/ng)**
S_1	PMMA	1.2	0.65
S_2	PS	1.1	0.59
S_3	PU	0.25	0.15
S_4	PVP	0.27	0.16

7.5 Experimental Setup

The sensor shown in Figure 7.1 was tested experimentally using the setup shown schematically in the Figure 7.6. After each microbeam was functionalized, the device was base excited by a piezoelectric actuator. The off chip piezoelement was excited by either a band-limited white noise signal that simultaneously excited all modes or by a swept sine signal, which were both supplied using a programmable function generator (HP 33120A). The motion of the device was sensed using a Polytec laser vibrometer. Specifically, using only one laser, which was pointed at shuttle mass (the red dot Labeled L in the lower right inset of Figure 7.6), the resonance frequency information for each of the microbeams was measured. The scanning feature of the laser vibrometer was used to determine and verify the mode shapes at each of the resonance frequencies of the device. A vector signal analyzer (HP 89410A) and computer were used to analyze the signal output from the vibrometer. During operation the the pressure in the chamber

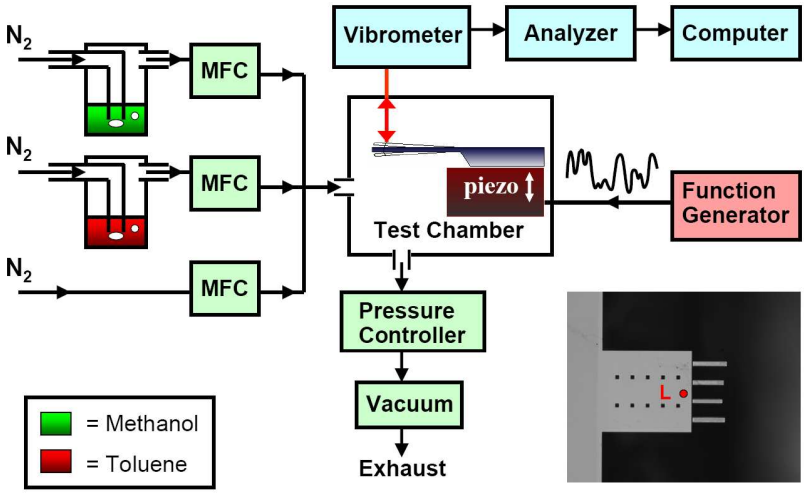

Figure 7.6: Setup used for the chemical detection and identification experiments.

was held constant using a pressure controller and a vacuum pump. Two mass flow controllers connected to bubblers containing toluene and methanol (nitrogen was used as the carrier gas) and a third mass flow controller connected to house nitrogen were used to deliver analyte mixtures with predetermined concentrations to the test chamber.

The analyte vapor concentration delivered from the bubbler is given by

$$C_v = \frac{P_v}{P_c},$$

where P_v and P_c are the partial pressure of the vapor in the head space of the bubbler and pressure of the carrier gas (nitrogen) at the inlet of the bubbler and the concentration C_v is in units moles analyte per moles mixture. To estimate the analyte concentration it is assumed that the vapor in the head space is in

equilibrium with the liquid, that the temperature of the liquid in the bubbler is constant, that the system is in steady state, that only vapor leaves the system, and that the air in the head space is 100% saturated with analyte vapor (100% humidity). The temperature dependent saturation vapor pressure of an organic compound is given by [106]

$$LogP_v = A - \frac{B}{T + C},$$

where A, B, and C are constants that are specific the particular organic compound, T is the temperature of the organic compound in ^{o}C, and P_v is the saturation vapor pressure in Torr. The constants for toluene and methanol are ($A = 6.95464$, $B = 1344.8$, $C = 219.482$) and ($A = 7.89750$, $B = 1474.08$, $C = 229.13$), respectively.

7.6 Device Response

Using a band-limited white noise signal, all modes were simultaneously excited and the resulting frequency response was recorded. Figure 7.7 depicts the frequency response of the shuttle mass after applying polymers to the microbeams, when the chamber pressure was held at $200\,Torr$ in a pure nitrogen environment. Note that the response of the shuttle mass was divided by the response of the

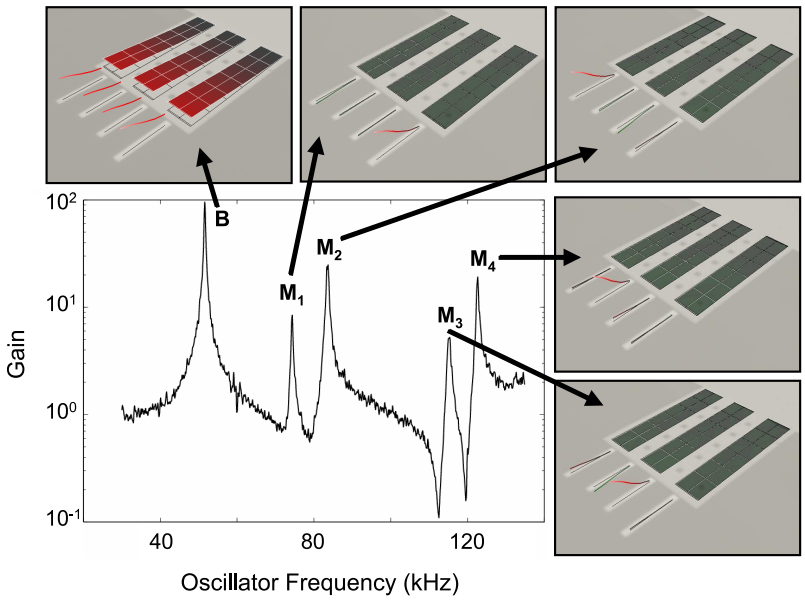

Figure 7.7: The frequency response of the device obtained experimentally by base exciting it with band-limited white noise and sensing the shuttle mass motion with the laser vibrometer in 200 $Torr$ vacuum. The mode shapes, obtained experimentally using a Polytec scanning laser vibrometer, at resonances B, M_1, M_2, M_3, and M_4, are also depicted.

piezo-element (the laser pointed at the base of the oscillator) to recover the gain of the shuttle mass, which is nondimensional.

Using the scanning laser vibrometer, the mode shape at each of the five resonances in the response shown in Figure 7.7 were measured. The device has a bulk out-of-plane mode labeled B and four higher frequency localized microbeam modes M_1 through M_4, which are used for sensing (see Figure 7.7 for experimental mode shapes). These mode shapes are in good agreement with the mode shapes predicted by FEA in Section 7.1 and verify that the four microbeam modes are well localized. Also, note that due to the localized nature of these modes, the mass responsivities (i.e. resonance frequency shifts per unit mass addition) associated with the resonances corresponding to M_1 through M_4 are slightly less than, but close to, the responsivities of an identical array of isolated, uncoupled microbeams. For the system of interest here, the mass responsivities are approximated to be 11 Hz/pg, 14 Hz/pg, 28 Hz/pg,and 31 Hz/pg for localized modes M_1 through M_4, respectively. This, provided a frequency resolution of approximately 1 Hz, a metric which is easily obtained with the current setup, renders sub-picogram mass sensitivities.

The device also operates reasonably well in air, which is a significant improvement over the first generation device. The response of the shuttle mass near each of the localized modes when the device is operated in air and in 200 $Torr$ vacuum

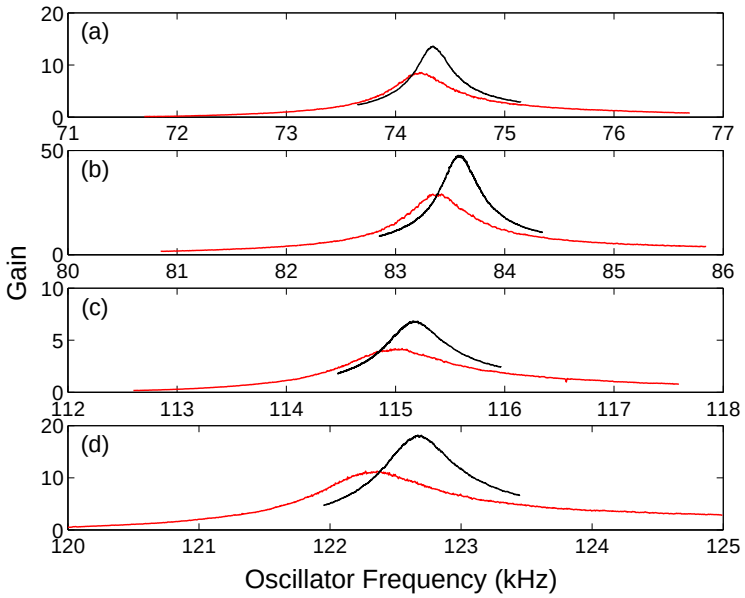

Figure 7.8: Experimentally obtained frequency response curves near localized modes (a) M_1, (b) M_2, (c) M_3, and (d) M_4 when the sensor is driven by a piezoelectric actuator in a chamber held at $200\,Torr$ (black curves) and atmospheric pressure (red curves).

is compared in Figure 7.8. As expected, the resonances show a reduction in the quality factor when operated in air. However, each resonance peak remains distinguishable at ambient pressure, which is a significant improvement over the first generation device. This improvement is attributed to the absence of a substrate surrounding the device. Estimated quality factors for each localized microbeam resonance in air and in $200\,Torr$ vacuum are provide in Table 7.4.

Table 7.4: Comparison of quality factor for each localized resonance in 200 $Torr$ vacuum and in air.

Resonance	Q in 200 $Torr$	Q in Air
M_1	244	174
M_2	263	167
M_3	227	151
M_4	242	147

7.7 Chemical Detection and Identification

Toluene and methanol vapors, as well as toluene/methanol mixtures, were delivered to the chamber while the device was in operation. The chemical detection experiments involved measuring the resonance frequencies M_1 through M_4 (using solely the response of the shuttle mass) in pure nitrogen gas, introducing an analyte and waiting for the absorption to reach steady state, measuring the resonance frequencies again, and determining the resulting frequency shifts. In this manner the frequency shift of each localized microbeam mode was determined for various analyte concentrations. Note, after introducing analyte mixtures, the absorption process was reversed by purging the chamber with nitrogen, thereby resetting the microbeam sensors.

Absorption of the analyte vapor into each polymer altered the effective masses of each microbeam, which caused the localized microbeam resonances, M_1 through M_4, to shift. For example, the resonance frequency shift of each localized mi-

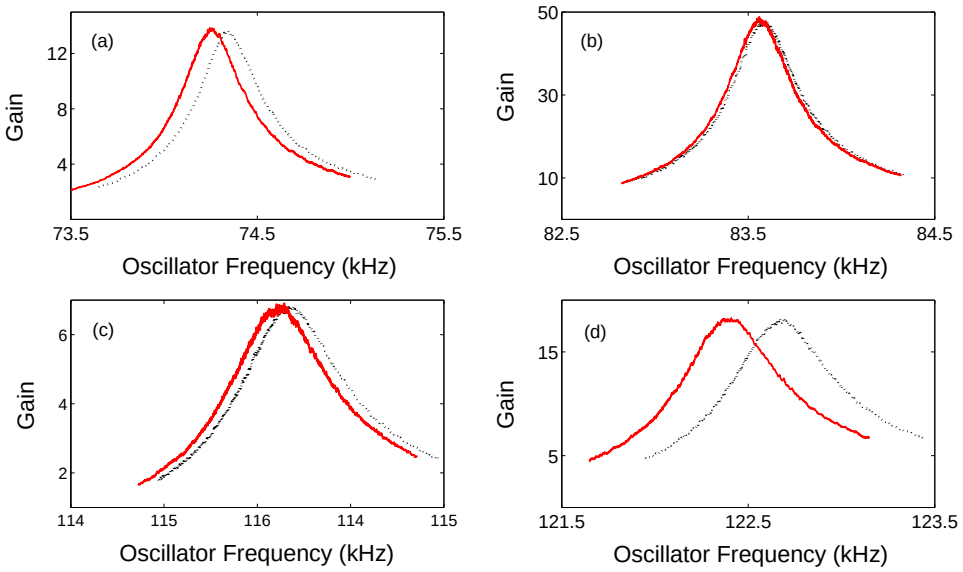

Figure 7.9: Experimentally obtained frequency response curves near localized modes (a) M_1, (b) M_2, (c) M_3, and (d) M_4 when the sensor driven by a piezoelectric actuator with a swept sine signal in 200 $Torr$ vacuum with pure nitrogen gas (black dotted curves) and 5.8% methanol vapor (red solid curves) flowing into the chamber. (Note that the blue curves were recorded after allowing the methanol to flow for 30 minutes.)

crobeam mode when the device is operated in a 5.8% methanol environment at 200 $Torr$, is shown in Figure 7.9. Note that in this figure, and in Figures 7.10 and 7.11, the device is excited with a swept sine wave. Band-limited white noise excitation yielded similar results, see Figure B.3 of Appendix B. It is also important to note that the lowest and highest resonance frequencies in Figure 7.9a and 7.9d, corresponding to the PMMA coated microbeam S_1 and the PVP coated microbeam S_4, respectively, exhibit the largest shifts and therefore the highest affinities for Methanol.

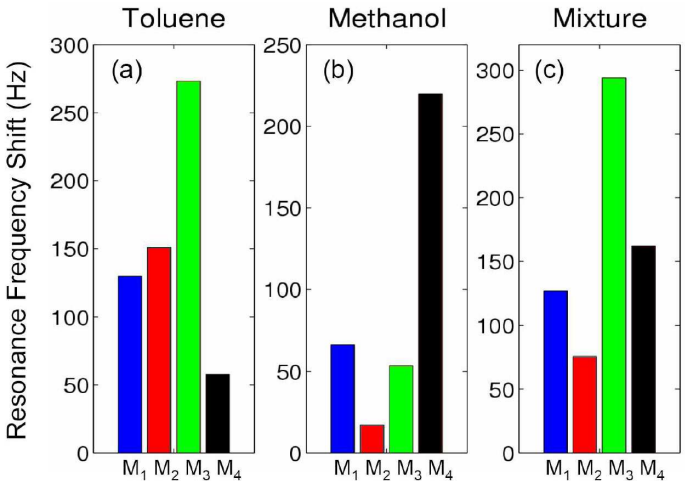

Figure 7.10: The resonance frequency shift of the localized microbeam modes (M_1-M_4) due to the presence of (a) 2.9% toluene, (b) 3.9% methanol, and (c) a mixture of 2.3% methanol and 2.3% toluene.

The polymers exhibit different sensitivities to different VOCs depending on their chemical makeup. Therefore, different frequency shift patterns in the four localized microbeam modes should be observed for different VOC's and VOC mixtures. Evidence of this is shown in Figure 7.10, which shows the frequency shift pattern of the resonances M_1 through M_4 when 2.9% toluene, 3.9% methanol, and a mixture of 2.3% methanol and 2.3% toluene are present in the chamber. The substantial difference in the frequency shift patterns verifies the sensors ability to detect and identify chemical vapors. The sensitivity of each microbeam to toluene and methanol, expressed as resonance frequency shift per unit analyte concentration, was determined by measuring the resonant frequency shifts in the coupled array for different analyte concentrations. Figure 7.11 shows the experimentally

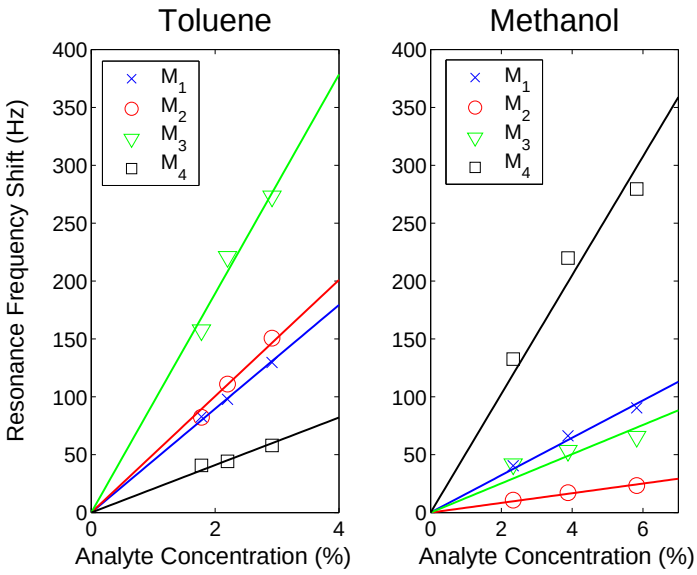

Figure 7.11: The resonance frequency shift of the localized microbeam modes (M_1-M_4) versus concentration of toluene (left) and methanol (right). Note, the analyte concentration is a percentage in moles of analyte per moles of mixture.

obtained sensitivities of M_1 through M_4 to toluene and methanol. The sensitivities were estimated by performing a linear fit to the experimental data for each mode, which are shown by the solid lines in figure 7.11. Using the shifts of the two most sensitive microbeam modes M_3 and M_4 in Figure 7.10c and their sensitivities from Figure 7.11, the concentration of methanol and toluene are calculated to be 2.8% and 2.0% respectively, which are in good agreement with the actual concentrations of 2.3% methanol and 2.3% toluene. The difference in the calculated and actual analyte concentrations of the mixture is likely due to orthogonality issues with the polymer coatings. Toluene and methanol show very different signatures, based on the frequency shift patterns shown in Figures 7.11 and 7.10,

and therefore are identifiable with the sensor. Similar to previous chemical nose work [12, 15, 49, 72] fingerprints based on the resonance frequency shift pattern in conjunction with statistical methods such as principal component analysis (PCA) can be used to identify more complex mixtures.

7.8 Q-Control and Frequency Tracking

In the previous section mass detection was carried by sweeping the driving frequency over a range near each of the localized microbeam modes and recording each of their resonance frequencies. This method, however, is very slow and is therefore not viable for practical implementations. In order to quickly determine the presence of added mass on each microbeam's surface, a method for tracking the localized microbeam resonances in real-time is necessary. One method for achieving this is to drive the device with band-limited white noise to simultaneously excite each localized microbeam mode and using signal processing software to peak track each of the resulting resonances. Another method, which is more promising, is to use positive feedback (or Q-control) to self-excite [5, 57, 79, 114, 127, 137] the device at each of its localized microbeam modes. One important aspect of this technique is that no external function generator is required and that thermal-mechanical noise and noise from the electronics drive the device. The output from

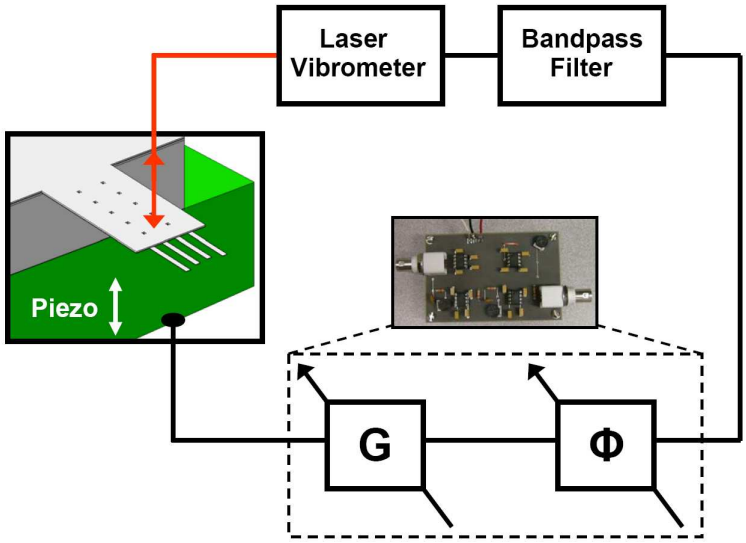

Figure 7.12: Schematic of the positive feedback technique used to self-excite the localized microbeam modes. The oscillator circuit is composed of a laser vibrometer, an adjustable bandpass filter, a variable gain amplifier, a variable phase shifter, and a piezoelectric actuator.

the transducer is fed into a bandpass filter, a variable gain amplifier and variable phase shifter, and finally back into the input of the device's actuator. A schematic of the self-excited approach is shown in Figure 7.12. In this system the coupled array of micro-cantilevers serves as the frequency determining element in the oscillator circuit. The adjustable bandpass filter is used to filter out frequencies that could excite unwanted modes of vibration. The filter is also adjusted so that only a single microbeam mode is excited at a time. The variable gain amplifier is adjusted to optimize the quality factor, minimized frequency fluctuations, and to maintain a constant vibration amplitude. The variable phase shifter is adjusted

to obtain maximum positive feedback at resonance. For an SDOF system a displacement signal output from the transducer would be phase shifted by 90^o to achieve maximum positive feedback at resonance (See Appendix C for theory). For the SISO microbeam array, the phase shift will be slightly different due to the coupling.

Using a piezoelectric actuator to excite the device and laser vibrometer to transduce the mechanical motion of the shuttle mass into an electrical signal, a device similar to the device shown in Figure 7.1 (the only difference is that this device has thinner microbeams, with approximate thicknesses of $0.7\,\mu m$) was driven by a swept sine and self-excited at atmospheric pressure. Figure 7.13a shows the response of the device, near the four localized microbeam modes, when driven by a swept sine wave. By adjusting the gain, phase, and bandpass filter, each of the localized microbeam modes are self-excited using the scheme shown in Figure 7.12. The self-excited localized microbeam modes M_1 through M_4 are shown in Figures 7.12b through 7.12e, respectively. Notice that self-excitation yields a considerable increase in the effective quality factors of the four resonance. The increased quality factor is directly related to the gain of the feedback amplifier. As a result, this method of self excitation is also called Q-control [127].

The device in Figure 7.1 was also operated in self-excitation mode at atmospheric pressure. A comparison between the localized microbeam resonance M_2

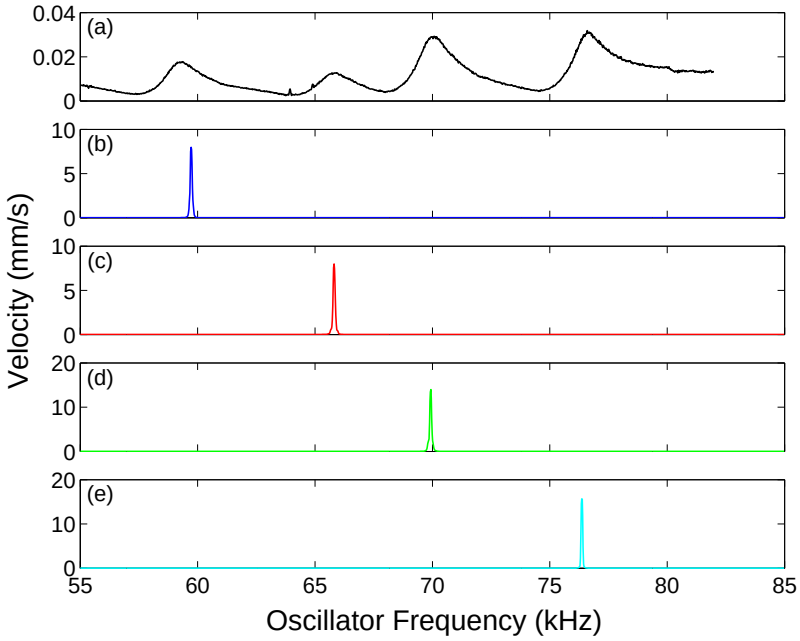

Figure 7.13: Frequency response of a SISO coupled microbeam sensor operated in air using (a) a swept sine wave to drive the device and (b)−(e) the positive feedback technique depicted in Figure 7.12 to individually excite each localized microbeam mode.

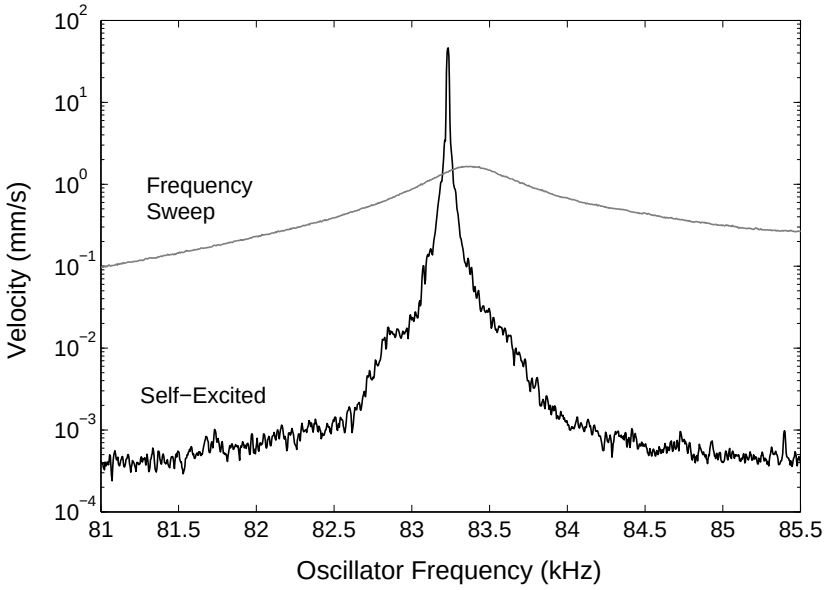

Figure 7.14: The frequency response of the device shown in Figure 7.1 near localized microbeam mode M_2, when the device is driven with a swept sine (grey curve) and self-excited (black curve). The plot clearly depicts an increase in the effective quality factor for the self-excited case.

when the device is driven in open loop with a swept sine and when the device is self-excited is shown in Figure 7.14. The effective quality factor of resonance M_2 increased by approximately two orders of magnitude ($Q \approx 165$ for the frequency sweep and $Q \approx 16380$ for self-excitation). The extremely narrow line-width suggests that high sensitivity detection can be achieved in air by tracking the location of this resonance peak. This can be achieved in practice by using a phase locked loop (PLL), frequency counter, a gated timer, or various other frequency demodulator circuits [5, 67, 79, 114, 127, 137].

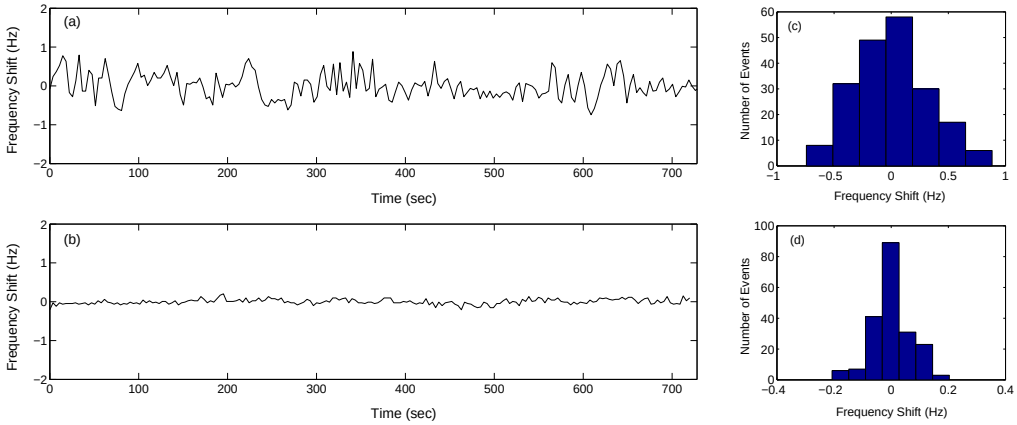

Figure 7.15: The frequency shift, subtracted from the mean, with respect to time of the localized microbeam mode of S_2 measured from (a) the response of the shuttle mass (laser pointed near the end of the shuttle mass) and (b) the response of microbeam S_2 (laser pointed at near the end of S_2). Histograms of the resonance frequency time series in (a) and (b) are shown in (c) and (d), respectively, and show normal distributions.

In this experiment a vector signal analyzer was used to track the frequency of the self-excited resonance peaks. Figures 7.15(a) and 7.15(b) show the time evolution of resonance frequency of S_2, which is subtracted from the mean of the frequency fluctuations, when the laser is pointed at the shuttle mass and directly at the microbeam S_2, respectively. Notice that better frequency stability is achieved when the resonance frequency is measured directly from S_2. Figures 7.15(c) and 7.15(d) are the histograms of the time series data shown in Figures 7.15(a) and 7.15(b), respectively. The histograms show that the population of all frequency measurements in each case have a normal (or gaussian) distribution. When the localized resonance of S_2 is measured from the shuttle mass, the standard deviation

of the frequency fluctuations is 0.32 Hz. Assuming a normal distribution, 99% of the resonance frequency population falls within 0.82 Hz of the mean, which is 83.362 kHz. In other words, this method achieves approximately 10 parts per million (ppm) frequency resolution. As stated in Section 7.6 the mass responsivity of the localized microbeam mode for S_2 is approximately 14 Hz/pg, which leads to an approximate mass sensitivity of 59 fg in air.

In comparison, smaller standard deviation (or higher frequency resolution) is obtained when the resonance frequency is measured directly from the response of S_2, specifically 0.068 Hz. In this case 99% of the resonance frequency population falls within 0.17 Hz of the mean, which is 83.556 kHz. In other words, the frequency resolution is approximately 2 ppm. Again, assuming an approximate responsivity of 14 Hz/pg, the mass sensitivity is approximately 12 fg.

A 5$\times$ increase in frequency resolution is observed when the localized resonance is measured directly from the response of microbeam S_2. One of the shortcomings of the SISO coupled microbeam array architecture is that there is an inherent reduction in the vibration amplitude when the coupled resonance frequencies are sensed through the response of an intermediate oscillator (the shuttle mass). This reduction in amplitude, and therefore reduction in signal to noise ratio, is believed to play a large role in the reduced frequency resolution. A 10$\times$ reduction in amplitude at this resonance is observed, when driving the device in open loop with

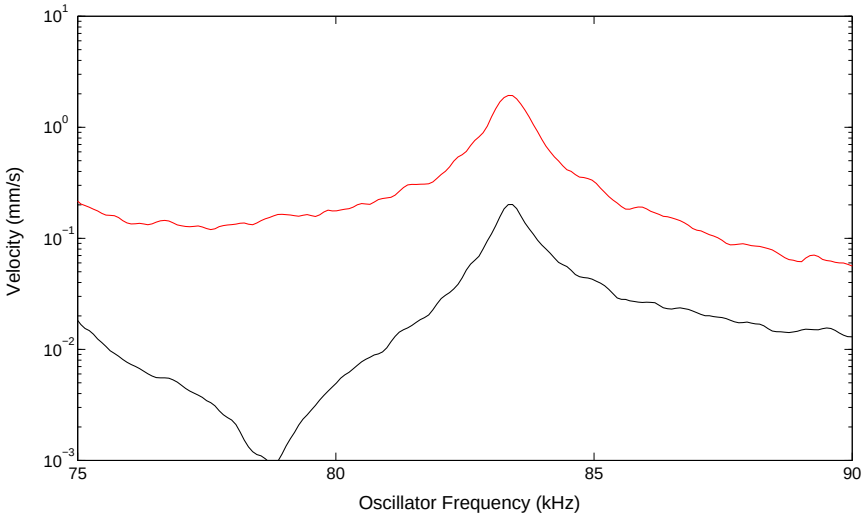

Figure 7.16: The frequency response of the shuttle mass (black curve) and microbeam S_2 (red curve) near localized microbeam mode M_2, when the device is driven with band-limited white noise in air.

a band-limited white noise signal, in the response of the shuttle mass compared to the response of microbeam S_2 (see Figure 7.16). It is important to note, however, that a mass sensitivity of $59\,fg$ in air shows significant improvement over the first generation device presented in Section 6, which showed poor performance in air. This relatively high sensitivity, is believed to be sufficient for some applications, however, can be drastically improved through device scaling in future generation devices. Also, the electronics used to track the resonance frequencies are believed to be the dominant source of noise in these measurements. Sensitivity metrics can also be increased in the future by implementing low noise amplifiers for the the variable gain and phase portions of the oscillator circuit. In addition, future

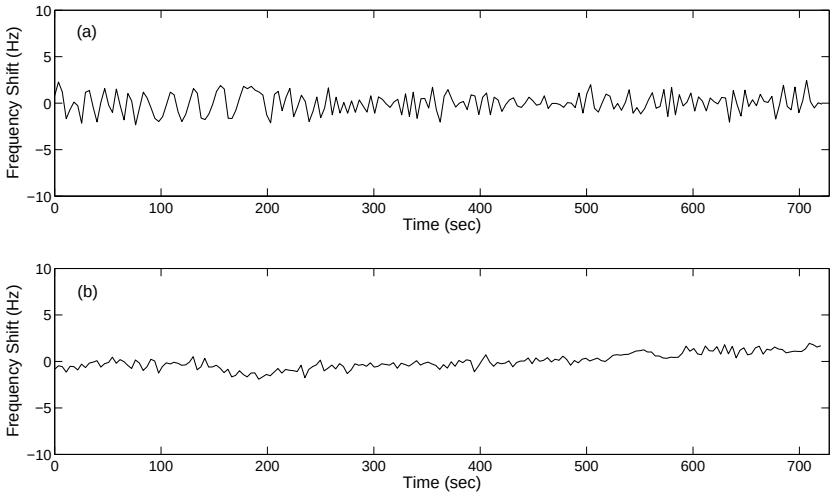

Figure 7.17: The frequency shift, subtracted from the mean, with respect to time of the localized microbeam mode of S_1 measured from (a) the response of the shuttle mass (laser pointed near the end of the shuttle mass) and (b) the response of microbeam S_2 (laser pointed at near the end of S_2).

devices could incorporate on-chip electronics with electrostatic detection to further improve sensitivity metrics [136].

The other localized modes were also tracked using the self-excitation, but showed slightly worse frequency resolution due to their smaller open-loop amplitudes. Figure 7.17 shows time evolution of the frequency fluctuations for the localized microbeam resonance corresponding to S_1, when the laser is pointed at the shuttle mass (Figure 7.17a) and when the laser is pointed directly at S_1 (Figure 7.17b). From these investigations it is clear that in future designs the amplitude of the localized resonances must be optimized while still maintaining ample localization for sensitive SISO arrayed mass sensing.

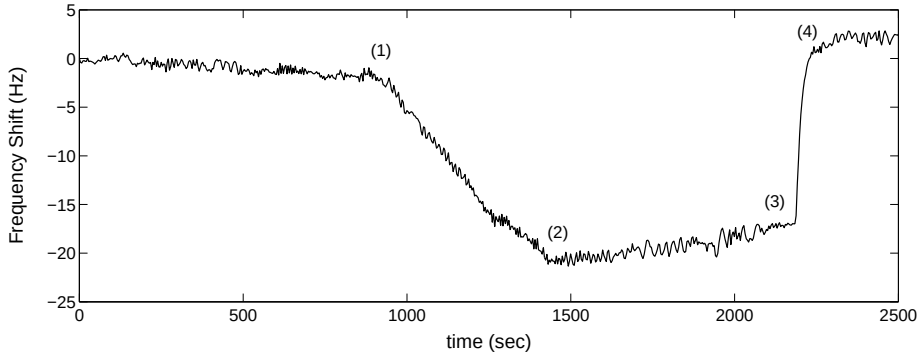

Figure 7.18: The frequency shift, subtracted from the mean, with respect to time of the localized microbeam mode of S_2 measured from the response of the shuttle mass. At location (1) 50 sccm of methanol is introduced into the chamber and the frequency shifts due to adsorption of methanol in the polystyrene. At location (2) the methanol is turned off and at location (3) the chamber is purged with nitrogen to desorb the methanol and reset the sensor. Finally, at location (4) the nitrogen is turned off and the frequency levels off again.

To investigate the kinematics of the absorbtion process the resonance frequency of the localized microbeam modes can be tracked using the self-excitation technique. The time evolution of the localized microbeam mode M_2 when methanol vapor is injected into the chamber is shown in Figure 7.18. Between 0 and 840 seconds, the chamber is filled with nitrogen gas at atmospheric pressure. The slight drift in the signal is can be due to thermal drift of the cantilever or it could also be due to changing temperature and/or pressure within the chamber. At 840 seconds, the location labeled (1), nitrogen was introduced into the chamber at a relatively slow flow rate of 50 *sccm*. Due to the adsorption of methanol into the polystyrene on the microbeam's tip, the effective mass of the microbeam increases and its coupled resonance frequency correspondingly decreases. At about

1320 seconds, location labeled (2), the methanol flow is shut off and the system is allowed to equilibrate for 840 seconds. Note, since the chamber volume is large, it takes a approximately 1 hour for the nitrogen in the chamber to be completely replaced by the methanol/nitrogen mixture from the bubbler, therefore the chamber is continually increasing in methanol concentration during the 480 seconds that the methanol mixture is flowing into the chamber. At location (3), the chamber is flushed with nitrogen and the methanol is desorbed from the polystyrene, thereby resetting the sensor. At location (4) the nitrogen flow is stopped and the chamber is held at atmospheric pressure. The resonance frequency of the localized microbeam mode after (4) is higher than it is before (1). This was likely due to the presence of a small amount of residual methanol in the first 840 seconds of the experiment (before (1)) that was left in the polymer from the previous experiment.

Chapter 8

SISO, Multi-Analyte Biosensor

The integration of micro- and nano- scale senors with lab-on-a-chip microfluidic systems allows for the detection of biomolecules in minuscule sample volumes, thereby dramatically reducing cost. By having sample preparation components on chip, these microfluidic systems also exhibit extremely high throughput. To date, a host of different transducers have been studied for biomolecular detection; electronic field effect sensors [47], optical sensors [30], static surface stress sensors [46, 8], and resonant sensors [123, 124, 63], each of which has inherent benefits and drawbacks. For these biosensing applications, the use of SISO coupled mass sensor arrays will reduce the number of input and output channels, thereby reducing hardware, signal processing requirements, and the overall size of the chip. This can ultimately lead to further reductions in cost and can also increase the amount of

real-estate on chip for microfluidic components which may be vital for applications where complex fluids, such as blood, are being analyzed. In this section the concept for a SISO multi-analyte biosensor, based on coupled microbeams with internal flow-through, is presented.

8.1 Operating in Liquids

Since biomolecular detection takes place in liquid environments, resonant based sensors suffer from increased viscous drag and reduced quality factor, which ultimately leads to low frequency resolution and mass sensitivity. Low quality factors for resonating cantilevers in liquid have been reported to be on the order of $Q \sim 1$ [127], which is approximately two orders of magnitude smaller than the quality factors obtained in air $Q \sim 100$.

If operated in a liquid environment, the peaks corresponding to the microbeam resonances in the multi-functional SISO mass sensor's shuttle mass response would likely be indistinguishable due to their inherently small amplitudes. To illustrate this the shuttle mass response of the second generation device was simulated for a variety of quality factors (see Figure 8.1). In this simulation the isolated resonances of the shuttle mass and microbeam sensors are assumed to all have equal quality factors. Notice that the four higher frequency localized microbeam modes

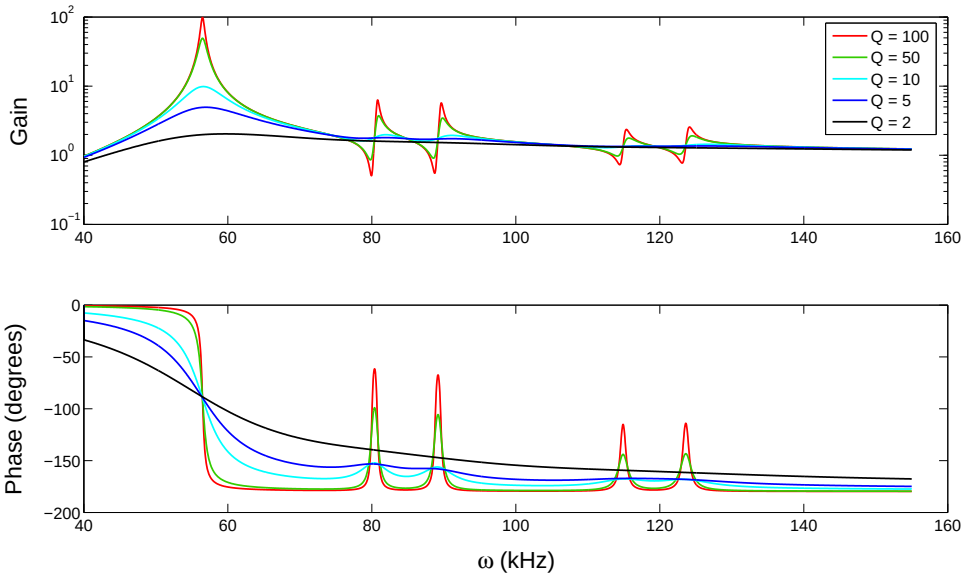

Figure 8.1: Simulated shuttle mass response for the second generation device in Section 7 for $Q = 100$ (red curve), $Q = 50$ (green curve), $Q = 10$ (light blue curve), $Q = 5$ (darker blue curve), and $Q = 2$ (black curve).

are indistinguishable for $Q = 5$ and completely disappear in the shuttle mass response for $Q = 2$. As a result the current device most-likely will not work in liquids, since Q-values below 5 are expected. The multi-functional SISO mass sensor is Q-limited, which necessitates the development of alternative approaches for liquid operation. Several approaches that have been investigated for overcoming the Q-limitation in liquids are discussed here.

One approach is to measure the resonant frequency of the oscillator before and after being submerged in the liquid sample environment [63, 123]. The problems with this method are (i) that the frequency measurement does not take place in

real time and (ii) that in removing the sensor from the liquid environment the likelihood of contamination is much greater. Another issue is that the detection process takes a long time.

Another approach is to use the Q-control method discussed in Section 7.8 to increase the effective quality factor by more than two orders of magnitude [5, 127, 57]. While this method increases Q, it has been found that it also increases noise [126]. Recent reports have shown that operating the self-excited loop in a nonlinear regime can squeeze noise and therefore increase mass sensitivity by several orders of magnitude in liquids [100]. This is a promising approach to overcoming the inherently low quality factors in liquids and it can be used in conjunction with the method discussed in the next section to create an ultra-sensitive SISO multi-analyte biosensor.

8.2 Internal Flow-Through

A very promising approach to detecting analytes in liquid is to create a sensor that utilizes sensing elements that serve as both microchannels and resonant microbeams [25, 24, 26]. By allowing fluid to flow through the inside of the hollow suspended microchannel resonator (SMR) the gaseous surrounding environment can be pumped down to low pressures, thereby increasing quality factor, frequency

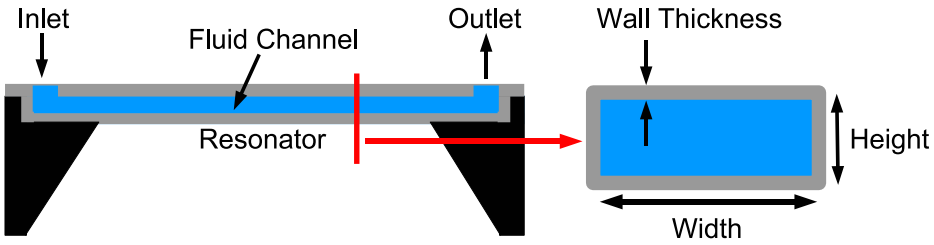

Figure 8.2: Concept for a the suspended microchannel resonator developed by Burg *et al* [26]. Also shown is the cross section of the hollow resonator with labeled dimensions.

resolution, and mass sensitivity by orders of magnitude. Burg *et al.* [23] state that no significant drop in quality factor occurs when fluid is present inside the channel and that quality factors of 15,000 are achieved when fluid is passing through the inside of the device. As a result of the high Q-value they achieve a frequency stability of approximately 10 parts per billion and a resulting mass sensitivity of 300 ag (attograms).

Figure 8.2 depicts the general SMR concept. Fluidic interfaces allow for liquids to be pumped from the inlet to the outlet of the microfluidic channel. The cross-section of the resonator is a hollow rectangle with moment inertia given by $I = (w_o h_o^3 - w_i h_i^3)/12$, where w_o and h_o are the outer width and outer height, respectively, and w_i and h_i are the inner width and inner height, respectively. The resonance frequency of the sensor is given by

$$\omega_0 = \sqrt{\frac{k}{m_{eff}}},$$

where m_{eff} is effective mass and k is the stiffness of the fixed-fixed hollow beam that is given by

$$k = \frac{192EI}{L^2},$$

where E is Young's modulus, I is the moment of inertia, and L is the length of the fixed-fixed beam. For a liquid filled resonator the total effective mass depends on the mass of the beam, the density of the liquid, and the mass of the analyte adsorbed on the inner walls of the resonator. For a detailed discussion of the design and sensitivity of SMR devices see [26]. It is important to note that the surface area to volume ratio of the channel plays an important role in the sensitivity of the device. Specifically, the sensitivity of the SMR to added mass increases as surface area to volume ratio increases, or the cross-section of the device decreases. The sensitivity will also increase as the wall thickness decreases.

In practice functionalization of the SMR inner walls, which takes place after fabrication, involves flowing a buffer solution containing a specific biomolecule through the inside of the microbeam. The biomolecule will non-specifically bind to the inner wall of the cantilever, thereby functionalizing the sensor surface. When the target biomolecules flow through channel they bind to the immobilized receptors. If the density of the bound molecules is different than the density of the buffer solution, then the effective mass of the microbeam will change, thereby shifting the resonant frequency. As an example, Burg et al [26] report that proteins

can be detected using this method because their densities are between 1.3 and $1.4\,g/cm^3$ and the density of a buffer solution is typically $1\,g/cm^3$. In recent work they have also used unfunctionalized devices to weigh individual nanoparticles and bacteria [23] with femtogram masses.

8.3 SISO Multi-Analyte Biosensor Concept

The current SMR concept can be used to detect multiple biomolecules in an array architecture, however, each would have to be monitored with an individual output signal. To reduce the number of input and output channels required, the SISO multi-analyte mass sensor array concept can be adopted. A host of different geometries and operation principles have been considered, however, the one discussed in this section is believed to be favorable for this application.

Here, some of the challenges associated with enabling this new technology are addressed. First of all, fluid needs to be passed to all of the microbeams in the coupled array, which as one could imagine, is nontrivial due to the complex geometry of the SISO multi-analyte mass sensors previously discussed. To functionalize the inside of each microbeam with a different coating, it is necessary to have an individual fluidic inlet and outlet for each microbeam. Again, this is complicated by the geometric constraints inherent to this type resonant sensor. Also,

the structure should be designed such that the localized microbeam modes are sufficiently separated from other vibration modes of the system and that there is ample spacing between each of the localized microbeam modes, while fitting into the SMR framework previously discussed. This design should also permit the implementation of a large number of frequency mistuned microbeams so that a wide variety of analytes can be detected.

A CAD drawing of the proposed device, which overcomes these design issues, is shown in Figure 8.3. The structure is composed of six functionalized microbeam sensors M, a rigid shuttle mass SM, and supporting flexures T. The arrows depict the direction of fluid flow through the fluidic channels of the resonant system. In this design all springs in the system (T and M) are hollow microfluidic channels. Shown by the black arrows, fluid will flow into the microbeams (FI) and out of the corresponding torsional springs (FO). By having the microbeams connected to mechanical ground, fluidic access to each of the microbeams can be achieved. Also, the microfluidic design allows the microbeams to be functionalized individually since there is an individual fluidic inlet and outlet for each beam.

To fabricate these devices micromachining techniques similar to those detailed in [26, 119] will be used. One of the challenges of fabricating these devices will be creating a multi-level structure where the shuttle mass is rigidly attached to the suspended microchannel network. In the current process flow, polysilicon is

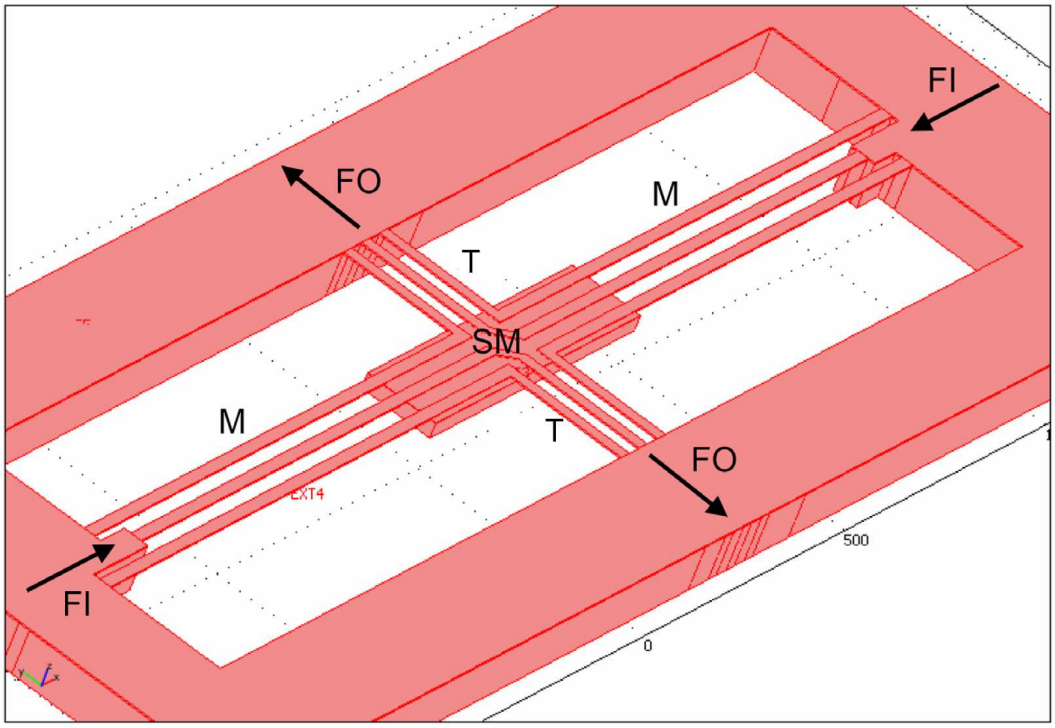

Figure 8.3: Concept for a third-generation SISO multi-analyte Biosensor that utilizes internal-flow through in a manner similar to [24, 25, 26]. The fluid inlets are labeled FI, fluid outlets FO, functionalized microbeam sensors M, shuttle mass SM, and supporting flexures T. Note that the microbeam sensors are connected to the supporting flexures in a manner that allows fluid to continuously flow into the microbeams sensors and out of the torsional springs (or visa versa).

used as a sacrificial layer and low-stress low-pressure chemical-vapor deposited (LPCVD) silicon nitride is used as the structural material. As a result, creating the shuttle mass portion of the resonator will likely involve additional deposition and patterning of polysilicon and silicon nitride layers.

8.4 Design and Finite Element Analysis

The inclusion of hollow microchannels complicates the design of the SISO multi-analyte mass sensor. The complexity of the structure shown in Figure 8.3 necessitates the use of iterative finite element analysis (FEA) techniques. In this manner the placement of the system's resonance frequencies and the shape and size of the sensor can be optimized to achieve the desired localized behavior and sensitivity metrics. The preliminary structural concept has been analyzed using finite element eigenfrequency analysis and will serve as an exemplary structure in the discussion to follow.

Figure 8.4 shows the FEA results for the deformed mode shape at various important eigenfrequencies (resonance frequencies). Note that the deformed shapes are scaled for visual purposes. Also note that there are four localized modes occurring between (C) and (D) and four between (F) and (G) that are not shown for the sake of brevity because they exhibit similar localized behavior but for different

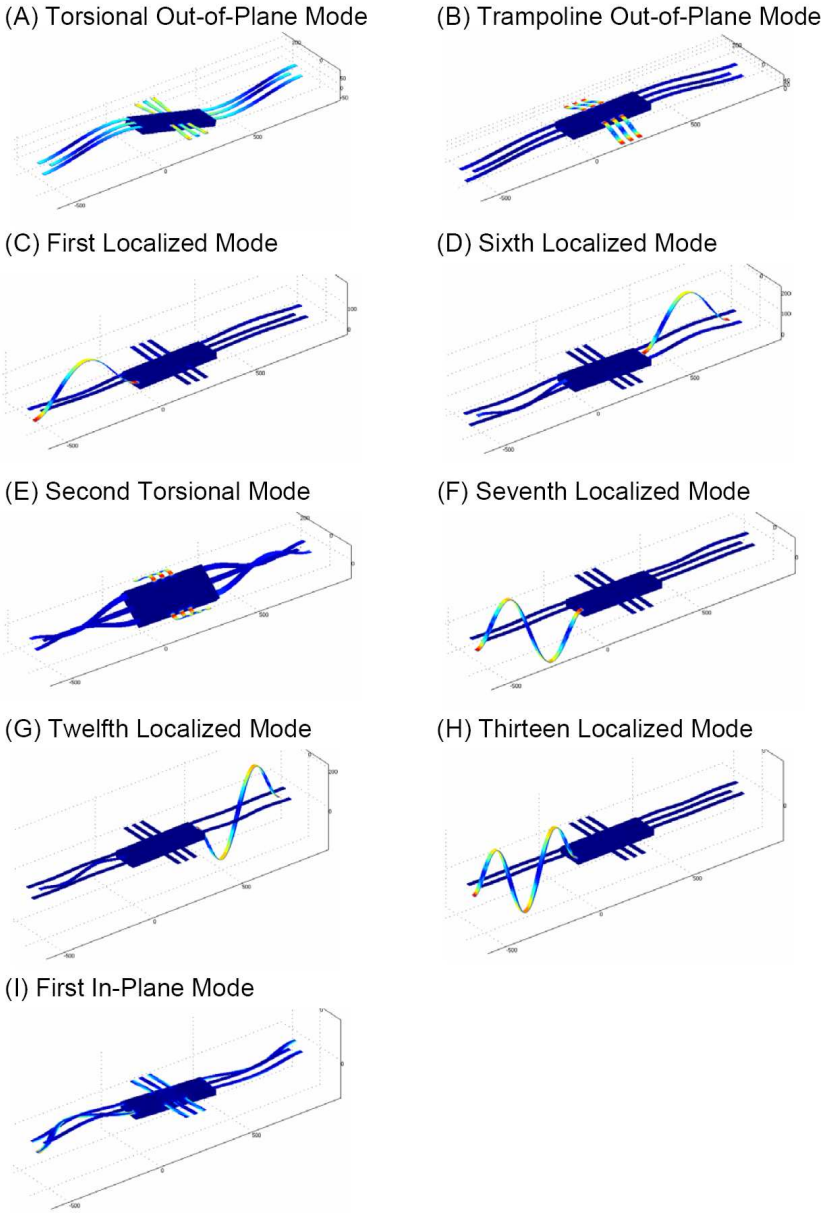

Figure 8.4: Mode Shapes for the concept device shown in Figure 8.3 obtained using finite element analysis. See Table 8.1 for corresponding resonant frequencies. Note that modes (C), (D), (F), (G), and (H) are highly Localized. Also note that four localized modes occurring between (C) and (D) and four localized modes between (F) and (G) are not shown here, but show similar behavior.

Table 8.1: Resonance frequencies determined through finite element analysis for the device shown in Figure 8.3. Mode shapes corresponding to these resonances are shown in Figure 8.4.

Mode and Label for Figure 8.4	**Resonance Freq. (kHz)**
Torsional Out-of-Plane Mode (A)	27.18
Tramploline Out-of-Plane Mode (B)	39.81
First Localized Microbeam Mode (C)	86.88
Second Localized Microbeam Mode (−)	94.93
Third Localized Microbeam Mode (−)	101.78
Fourth Localized Microbeam Mode (−)	109.73
Fifth Localized Microbeam Mode (−)	118.33
Sixth Localized Microbeam Mode (D)	124.03
Second Torsional Mode (E)	136.81
Seventh Localized Microbeam Mode (F)	240.48
Eighth Localized Microbeam Mode (−)	265.79
Ninth Localized Microbeam Mode (−)	281.17
Tenth Localized Microbeam Mode (−)	307.71
Eleventh Localized Microbeam Mode (−)	332.44
Twelfth Localized Microbeam Mode (G)	341.59
Thirteenth Localized Microbeam Mode (H)	472.60
First In-Plane Mode (I)	515.50

microbeams. The first 17 resonance frequencies and corresponding modes shapes are provided in Table 8.1.

The first mode (Figure 8.4(a)) of this system is a torsional resonance about the axis parallel to the supporting flexures T, which occurs at a relatively low frequency. By adjusting the geometry (i.e. the torsional stiffness) of these flexures and the length (in the direction perpendicular to the torsional axis) of the shuttle mass SM the frequency of this mode can be tuned to a location, in frequency space, well below the localized microbeam modes. Note that since the microbeams M

are attached to mechanical ground, their stiffnesses also affects the location of this mode.

The second mode (Figure 8.4(b)) is a 'trampoline-like' out of plane mode. The location of this mode will also be crucial in the design of these oscillators, in that it needs to occur well below the localized microbeam modes and either above or below the first torsional mode. In this case it occurs slightly above the first torsional mode. The location of this mode critically depends on the length of the springs, T, and the size of the shuttle mass, SM, and is largely unaffected by the stiffness of the microbeams since they are much longer than the springs T. Therefore the resonance frequency of this mode can be approximated by assuming that the structure is essentially a spring-mass system, where the effective mass is approximately the mass of SM and the stiffness is approximately the combined out of plane flexural stiffness of the six supporting flexures. The approximate resonance frequency is

$$\Omega_{trampoline} \approx \sqrt{\frac{k_T}{m_{sm}}},$$

where $k_T = 12nEI_T/L_T^3$, $n = 6$ since there are six flexures, I_T is the moment of inertia of the supporting flexures, L_T is the length of the supporting flexures, $m_{sm} = w_{sm}h_{sm}L_{sm}\rho$, ρ is the density of the structural material, and w_{sm}, h_{sm}, and L_{sm} are the width, height, and length of the shuttle mass, respectively.

Occurring well above the torsional and trampoline modes are the first six localized microbeam modes. The mode shapes shown in Figure 8.4(c) and (d) represent the first and sixth localized microbeam mode and indicate that energy is largely confined to the vibration of one microbeam. The four localized microbeam modes occurring between these two modes behave in a similar manner. Note that due to the boundary conditions of the microbeams, they essentially behave as fixed-fixed beams resonating at their first harmonic. As a result the resonance frequency of these modes can be approximated by the the following equation

$$\Omega_{localized} \approx \alpha_n \sqrt{\frac{EI_m}{m_m L_m^3}}, \tag{8.1}$$

where α_n is a constant that corresponds to the natural frequency of the nth mode (i.e. $\alpha_1 = 22.37$, $\alpha_2 = 61.67$, and $\alpha_3 = 120.90$), I_m is the moment of inertia of a given microbeam, m_m is the mass of a given microbeam, and L_m is the length of a given microbeam. Each localized microbeam mode causes the shuttle mass to vibrate torsionally since the vibrational energy is confined to a location far from the axis parallel to the supporting flexures T. The spacing between each localized mode is tailored by varying the length L_m of each microbeam.

The first six localized microbeam modes also occur well below the next highest frequency mode, which is a torsional mode about the axis parallel to the microbeams (see Figure 8.4(e)). This mode strongly depends on the stiffness of

the springs T, as well as the width w_{sm} (in the direction parallel to the springs T) of the shuttle mass.

The next six modes above the second torsional mode are localized microbeam modes where the microbeams behave essentially as fixed-fixed beams resonating at their second harmonic (see Figures 8.4(F) and (G)). Equation 8.1, with $\alpha_2 = 61.67$, can be used to estimate to resonance frequencies of these modes. Higher order localized modes offer several benefits for mass sensing First of all, their effective masses are lower, which leads to higher mass responsivities. Second, as demonstrated by Dohn *et al.* [39], the mass responsivity for a given mode of a microbeam strongly depends on the position of the bound analyte. For example, the first mode of a fixed-fixed beam will have the highest mass responsivity when mass is bound to the center of the beam, which happens to be the location of maximum amplitude. Likewise, the second mode of a fixed-fixed beam will have the highest mass responsivity when mass is bound to the two maximum amplitude points of the beam. Therefore, provided that this structure can be selectively functionalized, the use of these higher order localized modes can double the number of analytes that can be distinctly detected with a single input and a single output signal. Also, due to the position depended mass sensitive behavior of these modes, the location of a single biomolecule or group of biomolecules can be determined by the relative frequency shift of each of the microbeam modes,

which can ultimately help determine the distribution of bound and/or unbound mass in each of the microchannels.

The structure also has localized microbeam modes where the microbeams behave essentially as fixed-fixed beams resonating at their third harmonic (see Figures 8.4(H)). Sensing with these modes, however, may be hindered by higher order in-plane modes, as shown in Figure 8.4(I), that begin surfacing at nearby frequencies. Sensing with this third set of localized modes can be enabled by designing the microbeams to have higher in-plane stiffenesses (i.e. making the beams wider).

The analysis discussed here shows that this concept will work for the proposed SISO multi-functional SMR sensor application. While there are many geometries that can be realized for this application, it is in our opinion that this configuration will provide significant bandwidth and flexibility for a large number of microbeams to be implemented. At the same time this device concept is ideal for fitting into the current SMR framework.

8.5 Device Response

To investigate the response of the sensor previously discussed, a prototype device was fabricated. Figure 8.5 shows a scanning electron micrograph of the fabricated sensor, with labeled shuttle mass SM, microbeam sensors M, and sup-

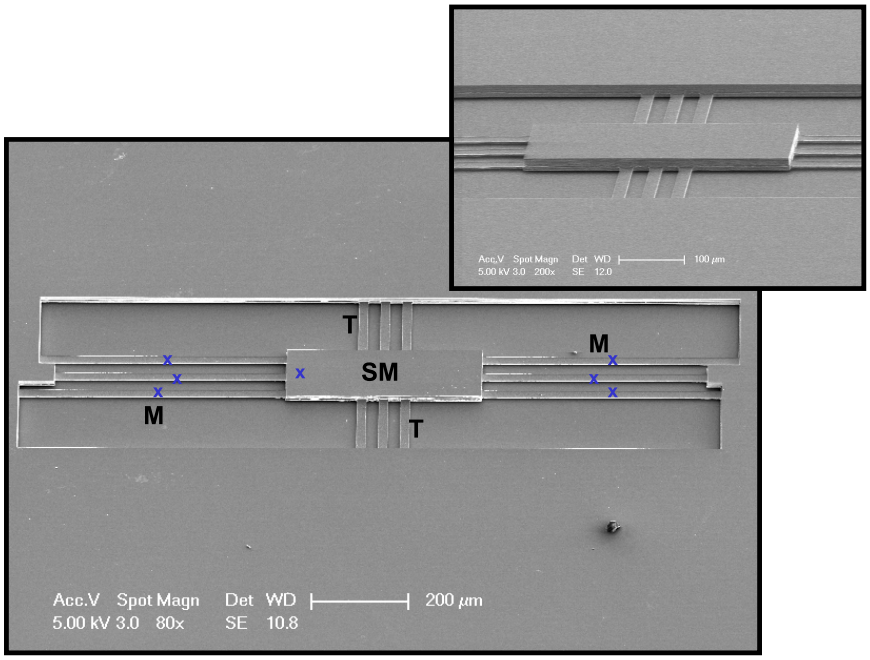

Figure 8.5: Scanning electron micrograph of a prototype device built to investigate the dynamics of the SISO multi-analyte device shown in Figure 8.3. The device was micromachined out of bulk silicon and is composed of a shuttle mass SM, microbeam sensors M, and supporting flexures T. Note that the seven laser locations corresponding to each of the seven responses shown in Figure 8.6 are depicted as blue x's.

porting flexures T. The device was fabricated on a silicon-on-insulator (SOI) wafer with a $30\,\mu m$ device layer and a $5\,\mu m$ buried oxide layer. The fabrication process flow discussed in Section 7.2 was used to fabricate the device, but without backside processing. The approximate dimensions for the fabricated device are shown in Table 8.2.

The device was actuated electrostatically by grounding the substrate beneath the device and applying a 2V square root cosine signal to the top device layer.

Table 8.2: Approximate dimensions for the prototype SISO multi-analyte device shown in Figure 8.5.

	Length (μm)	**Width** (μm)	**Thickness** (μm)
Shuttle Mass	406	126	30
Microbeams	548 527 508 491 476 461	20	3
Supporting Flexures	135	20	3

To reduce viscous damping and squeeze film damping, caused by fluid pumping between the device and the underlying substrate, testing was carried out in a chamber held at 7.6 $Torr$. The response of the shuttle mass and each of the microbeams were recovered by sweeping the frequency of the excitation signal and measuring the resulting motion, at each location labeled with a blue x in Figure 8.5, with a the laser vibrometer. The top panel of Figure 8.6 shows the response of the shuttle mass. The low frequency resonance labeled (1) is the trampoline mode and the six higher frequency resonances labeled (A)−(F) are the localized microbeam modes. In the bottom panel of Figure 8.6 the response near each resonances (A)−(F), for the shuttle mass and each of the microbeams, are shown. The relative amplitude of each response at resonance verifies the localized nature each microbeam mode. To verify the mode shape at each resonance a scanning laser vibrometer was used. Figure 8.7 depicts the experimental mode shape at

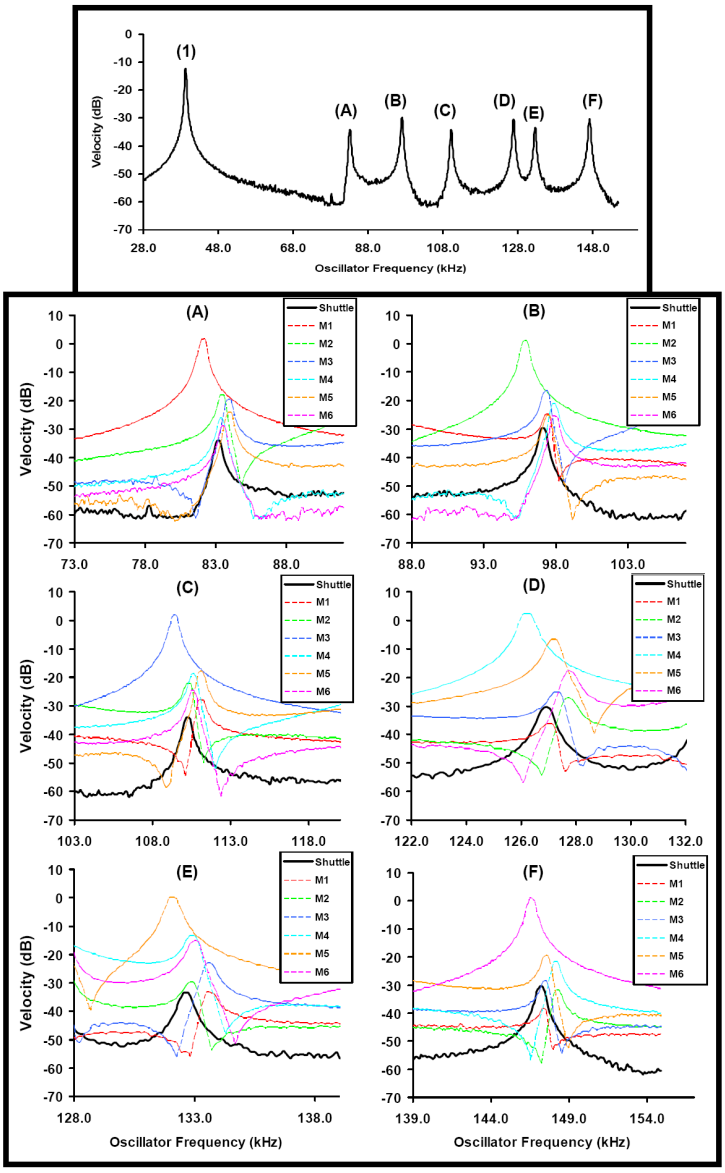

Figure 8.6: Frequency response, obtained using a laser vibrometer, of the prototype device shown in Figure 8.5 actuated electrostatically by a $2\,V$ square root cosine signal in $7.6\,Torr$ vacuum. The top panel shows the response of the shuttle mass and the bottom panel shows the response of each microbeam and the response of shuttle mass near each resonance labeled (A)−(F).

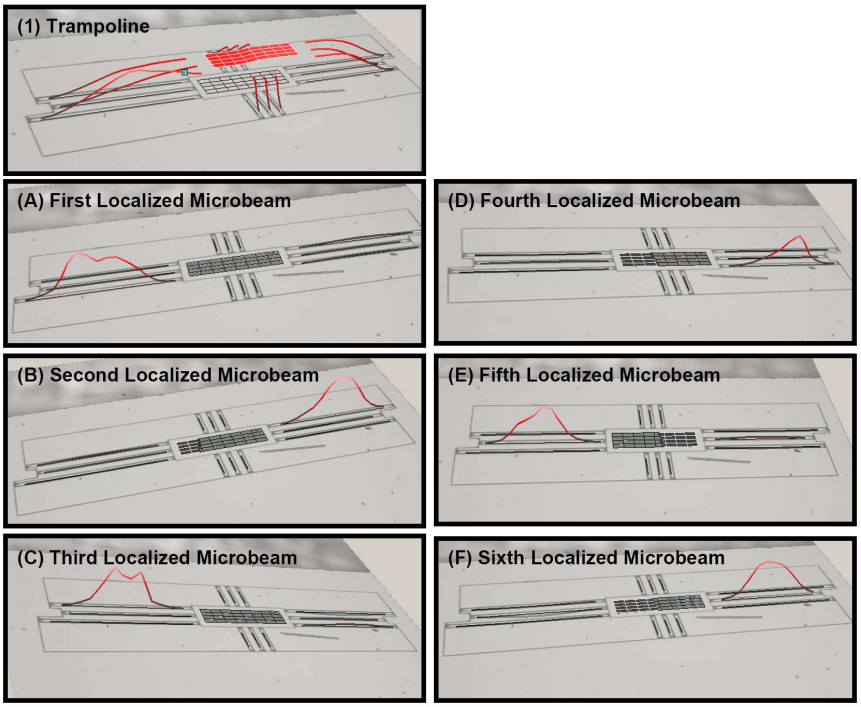

Figure 8.7: Mode Shapes, obtained experimentally using a scanning laser vibrometer, at each of the resonance frequencies shown in Figure 8.6. Note that modes (A)−(f) are highly Localized and agree well with the mode shapes predicted with FEA in Figure 8.4.

each of the seven resonances in Figure 8.6. The low frequency resonance exhibits 'trampoline-like' motion and the six higher frequency resonances are the highly localized as expected.

The results from this preliminary study show that the response of the device has six distinct resonances that correspond to a highly localized modes where the vibration energy is confined to a single microbeam. This will lead to the desired diagonally dominant mass responsivity matrix. The localized microbeam resonances are well separated from other modes in the system, such as the low

frequency trampoline mode. Also, there are six well defined microbeam resonances in the shuttle mass response, which indicates that this structure can successfully detect six distinct analytes with a single input single and a single output signal. One interesting aspect of this study is that the first torsional mode, which was predicted with FEA, was not observed in the frequency response. This is likely due to the fact that the entire structure is electrostatically forced with the same signal, which effectively suppresses the torsional modes. Torsional modes would appear if the the structure was asymmetrically forced.

Chapter 9

Conclusions and Future Work: Coupled MEMS

9.1 SISO Multi-Analyte Sensor

In the second portion of this dissertation, a novel concept that utilizes an array of coupled microelectromechanical resonators is investigated for mass sensing applications. By utilizing vibration localization in a set of frequency-mistuned microbeams, all requisite resonance frequency information is embedded in the response of a common shuttle mass oscillator, which is used for both actuation and sensing. As a result, multiple analytes can be uniquely detected with a single input signal and a single output signal. This coupled architecture therefore reduces

the hardware and signal processing requirements, as well as the overall cost and complexity of the sensor.

A relatively simple mathematical model used to describe the dynamics of this system has been formulated. In Chapter 5 the mathematical model, the desired frequency response characteristic, and design considerations are thoroughly discussed. The mass sensitivity of the coupled architecture is investigated and compared to the sensitivity of the conventional uncoupled architecture. It is shown that the mass responsivity of the coupled system will always be less than the mass responsivity of the uncoupled system; however, it will be close provided that the microbeam modes are sufficiently localized. The frequency resolution, which also affects mass sensitivity, is derived for the uncoupled system and used to gain an initial understanding of how the coupled system's frequency resolution will compare. The full derivation is set up for the coupled system, but is left for future work. Despite a reduced responsivity, frequency resolution, and therefore mass sensitivity, the platform is shown to have unique scaling benefits. Specifically, for the capacitive transduction case, it is shown that the detectiblility is drastically increased by sensing the resonances of the microbeams through a larger shuttle mass oscillator, which is expected to lead to increased sensor performance.

In Chapter 6 a proof-of-concept SISO multi-analyte sensor is presented, which was designed using the theoretical framework in Chapter 5. The response of the

device is investigated experimentally and the modes are investigated using finite element analysis (FEA). A mass detection experiment, which involved focused ion beam (FIB) depositing a small amount of Platinum on the tip of one of the microbeams, successfully proved the viability of the innovative mass sensing concept. The mass responsivity of the mass loaded microbeam was approximately $3.3\,Hz/pg$, a metric which is improved by device scaling in the second generation device. Some issues such as poor spacing between certain modes and low quality factors in air are observed in the experiments and used to help design the next generation devices.

In Chapter 7, the unique ability to detect and identify multiple chemicals using a single input and single output signal is experimentally demonstrated for the first time using the second generation coupled microresonator array. The sensor was backside processed to remove the substrate beneath the device to increase the Q-values of the localized microbeam modes in air. Each microbeam was functionalized with a different polymer coating, which readily absorbs volatile organic vapors, using a capillary tube dipping method. Solvent vapors (toluene, methanol, and toluene/methanol mixtures) were detected and identified based on the frequency shift pattern of the localized microbeam resonances. The sensor was operated in closed loop to self-excite each localized microbeam mode and affectively amplify their quality factors by two orders of magnitude. Using this

setup, the localized modes were tracked in real time. The frequency resolution was approximately 0.82 Hz in air for one of the localized resonances when it was tracked through the shuttle mass, which leads a mass sensitivity of 59 fg. This relatively high sensitivity in air shows significant improvement over the first generation device and is believed to be more than sufficient for many applications.

In Chapter 8 the concept for a third generation SISO multi-analyte biosensor is presented. When operated in liquids for biosensing applications, resonant sensors suffer from severely reduced Q-values. The internal flow-through concept developed by Burg *et al.* [26] solves this issue by allowing fluid to flow through the inside of the resonator while the surrounding environment is pumped down to low pressures. This concept is incorporated into the SISO coupled microresonator framework. This unique structure is discussed and analyzed using FEA. A prototype device is created to investigate the frequency response and mode shapes experimentally. The preliminary results verify that this device can be used to detect six distinct analytes using a single input and a single output signal. In addition this configuration will provide significant bandwidth and flexibility for a large number of microbeams to be implemented. At the same time this device concept is ideal for fitting into the current suspended microchannel resonator framework.

9.2 Future Work

There are many possible research directions for the SISO multi-analyte mass sensor platform detailed in this work. Here, future research topics that are believed to be the most important are discussed.

- **Ultrasensitive Coupled Nanomechanical Cantilever Arrays for Chemical Sensing Applications:** The SISO multi-analyte chemical sensor in Chapter 7 was created for proof-of-concept purposes. Future research is aimed at developing larger arrays of coupled mass sensors and optimizing their performance for chemical sensing applications such as explosive (TNT) detection and environmental monitoring. This will involve increasing the device's sensitivity to chemical analytes in ambient environmental conditions. The cantilevers in the coupled array can be downsized to the nano-scale in order to increase the mass responsivities of the localized modes. The goal will be to achieve sub-femtogram mass sensitivities and sub-ppm analyte sensitivities. By creating coupled arrays of nano-cantilevers that are capacitively actuated and sensed, the scaling benefits discussed in Section 5.6 will be investigated. Specifically, it will be demonstrated that the increased transducer area provided by the shuttle mass improves the detectability and therefore sensitivity of the mass sensor array. Further improvements

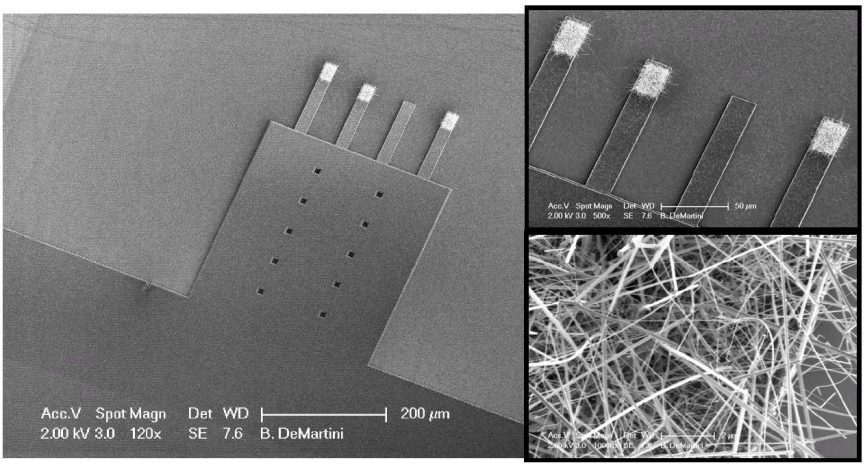

Figure 9.1: Scanning electron micrograph of a SISO multi-analyte sensor incorporating tin oxide nanowire patches on the tip of three microbeams. Note that the two righthand panels show close-ups of the nanowires.

in sensitivity can be made by using the self-excitation method discussed in Section 7.8 along with on-chip electronics for capacitive read-out. This novel platform will simultaneously enable single input-single output detection and ultrasensitive detection in realistic environments.

- **Surface Functionalization and Enhancement:** One of the major issues that chemical mass sensors still face is specificity. Non-specific binding events occurring at the chemically sensitized surface, when operating in a realistic environment, are not fully understood. In the future, collaborations with chemists and material scientists can be established to form an interdisciplinary research team to tackle this issue and engineer new chemical coatings that are resistant to non-specific binding. Also, selectively apply-

ing these coatings to individual nano-scale cantilevers will be non-trivial and will likely be accomplished by using techniques such as dip-pen lithography. In addition, methods for enhancing the active surface area to increase sensitivity are currently being developed by our research group. Figure 9.1 shows a SISO multi-analyte sensor with chemical vapor deposited tin oxide nanowire patches on the tips of three microbeams. Incorporating functionalized nanowire patches into SISO multi-analyte chemical sensors is expected to increase the active surface area by two to three orders of magnitude, thereby enhancing the overall sensitivity.

- **SISO Multi-Analyte Biosensor:** A concept for a biosensor that incorporates coupled microbeams with internal flow-through, which circumvents issues associated with operating the resonator in liquid environments and selective funcationalization, has been developed. While the dynamics of the structure have been investigated with FEA and preliminary experiments using a solid silicon structure, a considerable amount of work remains to fully develop the device. Future work is aimed at modifying the process flow developed by Burg *et al.* [26], for fabricating hollow resonators, to create the complex SISO multi-analyte biosensors. Once fabricated, each microbeam will be functionalized differently and multiple biomolecules will be detected with a single input signal and single output signal.

- **Quality Factor Control:** The second generation SISO multi-analyte chemical sensor was self-excited using a positive feedback scheme similar to [127]. While this method successfully amplified the quality factors of the localized microbeam modes by more than two orders of magnitude in air, it is uncertain whether or not it will work the same in liquids. Due to inherently low quality factors in liquids, the localized microbeam modes are expected be indistinguishable when operated in open loop. An interesting study would be to self-excite these sensors in liquids and investigate whether or not this method renders distinguishable resonances. Operating the self-excited loop in a nonlinear regime can also be utilized to help squeeze noise and therefore increase mass sensitivity in liquids [100]. In addition, the geometric configuration of future devices can be modified to passively reduce drag and therefore increase Q-values in liquids.

- **Frequency Resolution:** In Chapter 5.5 statistical techniques are used to determine the frequency resolution for an uncouple microresonator in the limit of thermal-mechanical noise. While this metric can be used to estimate how the frequency resolution of the coupled system compares to the uncoupled system, a more thorough treatment is necessary to fully understand how the coupled system's parameters effect the frequency resolution.

Future efforts will be aimed at deriving a frequency resolution metric for the coupled system using the same techniques used in the uncoupled derivation.

Bibliography

[1] http://www.comsol.com/.

[2] F. T. G. Abadal, J. Arcamone, J. Teva, J. V. A. Uranga, J. Lopez, X. Borrise, F. Perez-Murano, and N. Barniol. Coupling resonant micro and nanocantilevers to improve mass responsivity by detectability product. *Solid-State Sensors, Actuators and Microsystems Conference, TRANSDUCERS 2007. International*, pages 237–240, 2007.

[3] G. Abraham and A. Chatterjee. Approximate asymptotics for a nonlinear Mathieu equation using harmonic balance based averaging. *Nonlinear Dynamics*, 31:347–365, 2003.

[4] S. Adams, F. Bertsch, and N. MacDonald. Independent tuning of linear and nonlinear stiffness coefficients. *Journal of Microelectromechanical Systems*, 7 (2):172–180, 1998.

[5] T. Albrecht, P. Grtter, D. Horne, and D. Rugar. Frequency modulation detection using high-Q cantilevers for enhanced force microscope sensitivity. *Journal of Applied Physics*, 69 (2):668–673, 1991.

[6] A. Alsuwaiyan and S. Shaw. Localization of free vibration modes in systems of nearly-identical vibration absobers. *Journal of Sound and Vibration*, 228 (3):703–711, 1999.

[7] P. Anderson. Absence of diffusion in certain random lattices. *Physical Review*, 109 (5):1492–1505, 1958.

[8] Y. Arntz, J. Seelig, H. Lang, J. Zhang1, P. Hunziker, J. Ramseyer, E. Meyer, M. Hegner, and C. Gerber. Label-free protein assay based on a nanomechanical cantilever array. *Nanotechnology*, 14 (1):86–90, 2003.

[9] M. Ashhab, M. Salapaka, M. Dahleh, and I. Mezić. Dynamical analysis and control of microcantilevers. *Automatica*, 35 (10):1663–1670, 1999.

[10] M. Ashhab, M. Salapaka, M. Dahleh, and I. Mezić. Melnikov-based dynamical analysis of microcantilevers in scanning probe microscopy. *Nonlinear Dynamics*, 20 (3):197–220, 1999.

[11] K. Åström. Maximum likelihood and prediction error methods. *Automatica*, 16:551–574, 1980.

[12] M. Baller, H. Lang, J. Fritz, C. Gerber, J. Gimzewsk, U. Drechsler, H. Rothuizen, M. Despont, P. Vettiger, F. Battiston, J. Ramseyer, P. Fornaro, E. Meyer, and H. Guntherodt. A cantilever array-based artificial nose. *Ultramicroscopy*, 82(1-4):1–9, 2000.

[13] F. Bannon, J. Clark, and C.-C. Nguyen. High-Q HF microelectromechanical filters. *IEEE Journal of Solid-State Circuits*, 35 (4):512–526, 2000.

[14] M. Basso, L. Giarré, M. Dahleh, and I. Mezić. Numerical analysis of complex dynamics in atomic force microscopes. *Proceedings of the IEEE International Conference on Control Applications, Trieste, Italy 1-4 September 1998*, pages 1026–1030, 1998.

[15] F. Battiston, J.-P. Ramseyer, H. Lang, M. Baller, C. Gerber, J. Gimzewski, E. Meyer, and H.-J. Guntherodt. A chemical sensor based on a microfabricated cantilever array with simultaneous resonance-frequency and bending readout. *Sensors and Actuators B: Chemical*, 77 (1-2):122–131, 2001.

[16] A. Bietsch. Rapid functionalization of cantilever array sensors by inkjet printing. *Nanotechnology*, 15:873–880, 2004.

[17] G. Binnig, C. Quate, and C. Gerber. Atomic force microscope. *Physical Review Letters*, 56 (9):930–933, 1986.

[18] G. Binnig and H. Rohrer. Scanning tunneling microscopy. *Surface Science*, 152-153:17–26, 1985.

[19] G. Binnig, H. Rohrer, C. Gerber, and E. Weibel. Surface studies by scanning tunneling microscopy. *Physical Review Letters*, 49:57–61, 1982.

[20] T. Brown. Harsh military environments and microelectromechanical (MEMS) devices. *in Second IEEE International Conference on Sensors (Toronto, Ontatio)*, 2:753–760, 2003.

[21] E. Buks and M. Roukes. Electrically tunable collective response in a coupled micromechanical array. *Journal of Microelectrmechanical Systems*, 11 (6):802–807, 2002.

[22] E. Buks and M. Roukes. Electrically tunable collective response in a coupled micromechanical array. *Journal of Microelectromechanical Systems*, 11 (6):802–807, 2002.

[23] T. Burg, M. Godin, S. Knudsen, W. Shen, G. Carlson, J. Foster, K. Babcock, and S. Manalis. Weighing of biomolecules, single cells and single nanoparticles in fluid. *Nature*, 446:1066–1069, 2007.

[24] T. P. Burg and S. R. Manalis. Suspended microchannel resonators for biomolecular detection. *Applied Physics Letters*, 83(13):2698–2700, 2003.

[25] T. P. Burg and S. R. Manalis. Microfluidic packaging of suspended microchannel resonators for biomolecular detection. In *Proceedings of the 3rd IEEE/EMBS Special Topic Conference on Microtechnology in Medicine and Biology*, pages 264–267, Kahuku, Hawaii, 2005.

[26] T. P. Burg, A. R. Mirza, N. Milovich, C. H. Tsau, G. A. Popescu, J. S. Foster, and S. R. Manalis. Vacuum-packaged suspended microchannel resonant mass sensor for biomolecular detection. *Journal of Microelectromechanical Systems*, 15(6):1466–1476, 2006.

[27] H. Callen and T. Welton. Irreversibility and generalized noise. *Physical Review*, 83 (1):34–40, 1951.

[28] C.-T. Chen. *Linear Systems Theory and Design*. Oxford Press, New York, third edition, 1999.

[29] C. Cleland. Thermomechanical noise limits on parametric sensing with nanomechanical resonators. *New Journal of Physics*, 7:1–16, 2005.

[30] M. A. Cooper. Optical biosensors in drug discovery. *Nature Reviews Drug Discovery*, 1(7):515–528, 2002.

[31] R. Craig. *Structural Dynamics: An Introduction to Computer Methods*. John Wiley and Sons, Canada, 1981.

[32] H. Cramer. *Mathematical Methods of Statistics*. Princeton University Press, Princeton, New Jersey, 1946.

[33] M. C. Cross, A. Zumdieck, R. Lifshitz, and J. L. Rogers. Synchronization by nonlinear frequency pulling. *Physical Review Letters*, 93, 2004.

[34] S. K. De and N. Aluru. Complex oscillations and chaos in electrostatic microelectromechanical systems under superharmonic excitations. *Physical Review Letters*, 94:204101, 2005.

[35] A. Dec and K. Suyama. Micromachined varactors with wide tuning range. *IEEE Transactions on Microwave Theory and Techniques*, 46 (12):2587–2596, 1998.

[36] B. DeMartini, J. Moehlis, K. Turner, J. Rhoads, S. Shaw, and W. Zhang. Modeling of parametrically excited microelectromechanical oscillator dynamics with application to filtering. *in: Proceedings of the IEEE Sensor Conference, Irvine, CA*, pages 345–348, 2005.

[37] B. DeMartini, J. Rhoads, S. Shaw, and K. Turner. A single input-single output mass sensor based on a coupled array of microresonators. *Sensors and Actuators A: Physical*, 137:147–156, 2007.

[38] B. DeMartini, J. Rhoads, K. Turner, S. Shaw, and J. Moehlis. Linear and nonlinear tuning of parametrically excited MEM oscillators. *Journal of Microelectromechanical Systems*, 16(2):310–318, 2007.

[39] S. Dohn, R. Sandberg, W. Svendsen, and A. Boisen. Enhanced functionality of cantilever based mass sensors using higher modes. *Applied Physics Letters*, 86:233501, 2005.

[40] D. Eigler and E. Schweizer. Positioning single atoms with a scanning tunnelling microscope. *Nature*, 344:524 – 526, 1990.

[41] K. Ekinci, X. Huang, and M. Roukes. Ultrasensitive nanoelectromechanical mass detection. *Applied Physics Letters*, 84 (22):4469–4471, 2004.

[42] K. Ekinci, Y. Yang, and M. Roukes. Ultimate limits to inertial mass sensing based upon nanoelectromechanical systems. *Journal of Applied Physics*, 95 (5):2682–2689, 2004.

[43] E. Eklund and A. Shkel. Factors affecting the performance of micromachined sensors based on Fabry-Perot interferometry. *Journal of Micromechanics and Microengineering*, 15:1770–1776, 2005.

[44] R. Feynman. There's plenty of room at the bottom. *Journal of Microelectromechanical Systems*, 1 (1):60–66, 1992.

[45] E. Forsen, G. Abadal, S. Ghatnekar-Nilsson, J. Teva, J. Verd, R. Sandberg, W. Svendsen, F. Perez-Murano, J. Esteve, E. Figueras, F. Campabadal, L. Montelius, N. Barniol, and A. Boisen. Ultrasensitive mass sensor fully integrated wtih complementary metal-oxide-semiconductor circuitry. *Applied Physics Letters*, 87:043507, 2005.

[46] J. Fritz, M. Baller, H. Lang., H. Rothuizen, P. Vettiger, E. Meyer, H.-J. Gntherodt, C. Gerber, and J. Gimzewski. Translating biomolecular recognition into nanomechanics. *Science*, 288:316–318, 2000.

[47] J. Fritz, E. Cooper, S. Gaudet, P. Sorger, and S. Manalis. Electronic detection of DNA by its intrinsic molecular charge. *Proceedings of the National Academy of Sciences of the United States of America*, 99 (22):14142–14146, October 29, 2002.

[48] T. Gabrielson. Mechanical-thermal noise in micromachined acoustic and vibration sensors. *IEEE Transactions on Electron Devices*, 40 (5):903–909, 1993.

[49] J. Gardner and P. Bartlett. *Sensors and Sensory Systems for an Electronic Nose*. Kluwer Academic Publishers, Boston, 1992.

[50] D. Ginger, H. Zhang, and C. Mirkin. The evolution of dip-pen nanolithography. *Wiley InterScience: Angewandte Chemie International Edition*, 43(1):30–45, 2003.

[51] J. Grate and M. Abraham. Solubility interactions and the design of chemically selective sorbent coatings for chemical sensors and arrays. *Sensors and Actuators B: Chemical*, 3 (2):85–111, 1991.

[52] J. Guckenheimer and P. Holmes. *Nonlinear Oscillations, Dynamical Systems, and Bifurcations of Vector Fields*. Springer-Verlag, New York, 1983.

[53] A. Gupta, D. Akin, and R. Bashir. Single virus particle mass detection using microresonators with nanoscale thickness. *Applied Physics Letters*, 84(11):1976–1978, 2004.

[54] C. Hagleitner, D. Lange, A. Hierlemann, O. Brand, and H. Baltes. CMOS single-chip gas detection system comprising capacitive, calorimetric and mass-sensitive microsensors. *IEEE Journal of Solid-State Circuits*, 37 (12):1867–1878, 2002.

[55] A. Hierlemann, D. Lange, C. Hagleitner, N. Kerness, A. Koll, O. Brand, and H. Baltes. Application-specific sensor systems based on CMOS chemical microsensors. *Sensors and Actuators B: Chemical*, 70 (1-3):2–11, 2000.

[56] C. Hodges. Confinement of vibration by structural irregularity. *Journal of Sound and Vibration*, 82 (3):411–424, 1982.

[57] H. Holscher, D. Ebeling, and U. Schwartz. Theory of Q-controlled dynamic force microscopy in air. *Journal of applied Physics*, 99:084311, 2006.

[58] R. Howe and R. Muller. Integrated resonant-microbridge vapor sensor. *IEEE International Electron Devices Meeting*, 30:213–216, 1984.

[59] R. Howe and R. Muller. Resonant-microbridge vapor sensor. *IEEE Transactions on Electron Devices*, 33(4):499–506, 1986.

[60] S. Hu and A. Raman. Chaos in atomic force microscopy. *Physical Review Letters*, 96:036107, 2006.

[61] B. Ilic, D. Czaplewski, H. G. Craighead, P. Neuzil, C. Campagnolo, and C. Batt. Mechanical resonant immunospecific biological detector. *Applied Physics Letters*, 77 (3):450, 2000.

[62] B. Ilic, D. Czaplewski, M. Zalalutdinov, H. Craighead, P. Neuzil, C. Campagnolo, and C. Batt. Single cell detection with micromechanical oscillators. *Journal of Vacuum Science and Technology B: Microelectronics and Nanometer Structures*, 19 (6):28252828, 2001.

[63] B. Ilic, Y. Yang, and H. G. Craighead. Virus detection using nanoelectromechanical devices. *Applied Physics Letters*, 85(13):2604–2606, 2004.

[64] F. Jamitzky, M. Stark, W. Bunk, W. Heckl, and R. Stark. Chaos in dynamic atomic force microscopy. *Nanotechnology*, 17:S213–S220, 2006.

[65] J. Judge, C. Pierre, and O. Mehmed. Experimental investigation of mode localization and forced response amplitude magnification for a mistuned bladed disk. *Journal of Engineering for Gas Turbines and Power*, 123:940–950, 2001.

[66] M. Kendall. *The Advanced Theory of Statistics*, volume 2. Griffin, London, second edition, 1967.

[67] S. Kim, T. Ono, and M. Esashi. Capacitive resonant mass sensor with frequency demodulation detection based on resonant circuit. *Applied Physics Letters*, 88:053116, 2006.

[68] K. M. Klein, G. T. Ostrowicki, A. Gewirtz, and S. K. Sitaraman. Micro and nano thin film devices as bio-assays for cancer diagnosis. In *IMECE 2006: The 2006 ASME International Mechanical Engineering Conference and Exposition*, Chicago, Illinois, 2006.

[69] T. Kouh, D. Karabacak, D. Kim, and K. Ekinci. Diffraction in optical interferometric displacement detection in nanomechanical systems. *Applied Physics Letters*, 86:013106, 2005.

[70] H. Lang, M. Baller, R. Berger, C. Gerber, J. Gimzewski, F. Battiston, P. Fornaro, J. Ramseyer, E. Meyer, and H. Guntherodt. An artificial nose based on a micromechanical cantilever array. *Analytica Chimica Acta*, 393 (1-3):59–65, 1999.

[71] H. Lang, M. Hegner, and C. Gerber. Cantilever array sensors. *Materials Today*, 8 (4):3036, 2005.

[72] H. Lang, J. Ramseyer, W. Grange, T. Braun, D. Schmid, P. Hunziker, C. Jung, M. Hegner, and C. Gerber. An artificial nose based on microcantilever array sensors. *Journal of Physics - Conference Series: International Conference on Nanoscience and Technology*, 61:663667, 2007.

[73] S. Lee and C. T.-C. Nguyen. Mechanically-coupled micromechanical resonator arrays for improved phase noise. In *2004 IEEE International Ultrasonics, Ferroelectrics, and Frequency Control Joint 50th Anniversary Conference*, pages 144–150, Montreal, Canada, 2004.

[74] R. Lifshitz and M. C. Cross. Response of parametrically driven nonlinear coupled oscillators with application to micromechanical and nanomechanical resonator arrays. *Physical Review B*, 67, 2003.

[75] S. Liu, A. Davidson, and Q. Lin. Simulation studies on nonlinear dynamics and chaos in a MEMS cantilever control system. *Journal of Micromechanics and Microengineering*, 14:1064–1073, 2004.

[76] E. Lorenz. Deterministic nonperiodic flow. *Journal of the Atmospheric Sciences*, 20:130–141, 1963.

[77] A. Luo and F. Wang. Nonlinear dynamics of a micro-electro-mechanical system with time-varying capacitors. *Journal of Vibration and Acoustics*, 126:77–83, 2004.

[78] Y. Martin, C. Williams, and H. Wickramasinghe. Atomic force microscope-force mapping and profiling on a sub 100-A scale. *Journal of Applied Physics*, 61 (10):4723, 1987.

[79] A. Mehta, S. Cherian, D. Hedden, and T. Thundat. Manipulation and controlled amplification of Brownian motion of microcantilever sensors. *Applied Physics Letters*, 78 (11):1637, 2001.

[80] G. Meyer and N. Amer. Novel optical approach to atomic force microscopy. *Applied Physics Letters*, 53 (12):1045–1047, 1988.

[81] F. Moon. *Chaotic Vibrations: An Introduction for Applied Scientists and Engineers*. Wiley Interscience, Toronto, Canada, 1987.

[82] M. Napoli, W. Zhang, K. Turner, and B. Bamieh. Characterization of electrostatically coupled microcantilevers. *Journal of Microelectromechanical Systems*, 14 (2):295–304, 2005.

[83] A. H. Nayfeh and D. T. Mook. *Nonlinear Oscillations*. Wiley-Interscience, New York, 1977.

[84] C. T.-C. Nguyen. Micromechanical resonators for oscillators and filters. In *1995 IEEE International Ultrasonics Symposium*, pages 489–499, Seattle, Washington, 1995.

[85] C. T.-C. Nguyen. High-Q micromechanical oscillators and filters for communications. In *1997 IEEE International Symposium on Circuits and Systems*, pages 2825–2828, Hong Kong, 1997.

[86] N. Nugaeva, K. Gfeller, N. Backmann, H. Lang, M. Duggelin, and M. Hegner. Micromechanical cantilever array sensors for selective fungal immobilization and fast growth detection. *Biosensors and Bioelectronics*, 21 (6):849–856, 2005.

[87] Y. Oh, B. Lee, S. Baek, H. Kim, and J. K. S. K. C. Song. A surface-micromachined tunable vibratory gyroscope. *in: Proceedings of the IEEE Tenth Annual International Microelectromechanical Systems Workshop, Nagoya, Japan*, pages 272–277, 1997.

[88] T. Okamoto, T. Suzuki, and N. Yamamoto. Microarray fabrication with covalent attachment of dna using bubble jet technology. *Nature Biotechnology*, 18:438–441, 2000.

[89] T. Ono, X. Li, H. Miyashita, and M. Esashi. Mass sensing of adsorbed molecules in subpicogram sample with ultrathin silicon resonator. *Review of Scientific Instruments*, 74 (3):1240–1243, 2003.

[90] L. Oropeza. *Investigations on Novel Platforms of Micro Electro Mechanical Inertial Sensors: Analysis, Construction and Experimentation*. Ph.d., University of California, Santa Barbara, 2007.

[91] K. Peterson. Silicon as a mechanical material. *Proceedings of the IEEE*, 70(5):420–457, 1982.

[92] C. Pierre and E. Dowell. Localization of vibrations by structural irregularity. *Journal of Sound and Vibration*, 114 (3):549564, 1987.

[93] L. Pinnaduwage, A. Gehl, D. Hedden, G. Muralidharan, T.Thundat, R. Lareau, T. Sulchek, L. Manning, B. Rogers, M. Jones, and J. Adams. Explosives: A microsensor for trinitrotoluene vapour. *Nature*, 425:474, 2003.

[94] L. Pinnaduwage, T.Thundat, A. Gehl, S. Wilson, D. Hedden, and R. Lareau. Desorption characteristics of uncoated silicon microcantilever surfaces for explosive and common nonexplosive vapors. *Ultramicroscopy*, 100:211–216, 2004.

[95] H. W. C. Postma, I. Kozinsky, A. Husain, and M. L. Roukes. Dynamic range of nanotube- and nanowire-based electromechanical systems. *Applied Physics Letters*, 86:223105, 2005.

[96] S. Pourkamali, Z. Hao, and F. Ayazi. VHF single crystal silicon capacitive elliptic bulk-mode disk resonators-part I: implementation and characterization. *Journal of Microelectromechanical Systems*, 13 (6):1043–1053, 2004.

[97] S. Pourkamali, Z. Hao, and F. Ayazi. VHF single crystal silicon capacitive elliptic bulk-mode disk resonators-part II: implementation and characterization. *Journal of Microelectromechanical Systems*, 13 (6):1054– 1062, 2004.

[98] A. Qazi, D. Nonis, A. Pozzato, M. Tormen, M. Lazzarino, S. Carrato, and G. Scoles. Asymmetrical twin cantilevers for single molecule detection. *Applied Physics Letters*, 90:173118, 2007.

[99] R. Raiteri, M. Grattarola, H.-J. Butt, and P. Skladal. Micromechanical cantilever-based biosensors. *Sensors and Actuators B: Chemical*, 79 (2-3):115–126, 2001.

[100] D. Ramos, J. Mertens, M. Calleja, and J. Tamayo. Photothermal self-excitation of nanomechanical resonators in liquids. *Applied Physics Letters*, 92:173108, 2008.

[101] T. Remtema and L. Lin. Active frequency tuning for micro resonators by localized thermal stressing effects. *Sensors and Actuators A-Physical*, 91 (3):326–332, 2001.

[102] M. Requa and K. Turner. Electromechanically driven and sensed parametric resonance in silicon microcantilevers. *Applied Physics Letters*, 88:263508, 2006.

[103] M. Requa and K. Turner. Precise frequency estimation in a microelectromechanical parametric resonator. *Applied Physics Letters*, 90:173508, 2007.

[104] J. Rhoads, S. Shaw, K. Turner, and R. Baskaran. Tunable MEMS filters that exploit parametric resonance. *Journal of Vibration and Acoustics*, 127 (5):423–430, 2005.

[105] J. Rhoads, S. Shaw, K. Turner, J. Moehlis, B. DeMartini, and W. Zhang. Generalized parametric resonance in electrostatically-actuated microelectromechanical oscillators. *Journal of Sound and Vibration*, 296:797–829, 2006.

[106] J. Riddick. *Organic Solvents; Physical Properties and Methods of Purification*. Wiley-Interscience, New York, third edition, 1970.

[107] D. Rugar, R. Budakian, H. Marmin, and B. Chui. Single spin detection by magnetic resonance force microscope. *Nature*, 430:329–332, 2004.

[108] D. Rugar and P. Grutter. Mechanical parametric amplification and thermomechanical noise squeezing. *Physical Review Letters*, 67 (6):699–702, 1991.

[109] O. Sahin, G. Yaralioglua, R. Growa, S. F. Zappea, A. Atalarb, C. Quatea, and O. Solgaarda. High-resolution imaging of elastic properties using harmonic cantilevers. *Sensors and Actuators A: Physical*, 114 (2-3):183–190, 2004.

[110] D. Sarid. *Scanning Force Microscopy with Applications to Electric, Magnetic, and Atomic Forces*. Oxford University Press, New York, 1994.

[111] M. Sato, B. E. Hubbard, L. Q. English, A. J. Sievers, B. Ilic, D. A. Czaplewski, and H. G. Craighead. Study of intrinsic localized vibrational modes in micromechanical oscillator arrays. *Chaos*, 13(2):702–715, 2003.

[112] M. Sato, B. E. Hubbard, and A. J. Sievers. Nonlinear energy localization and its manipulation in micromechanical oscillator arrays. *Reviews of Modern Physics*, 78(1):137–157, 2006.

[113] M. Sato, B. E. Hubbard, A. J. Sievers, B. Ilic, D. A. Czaplewski, and H. G. Craighead. Observation of locked intrinsic localized vibrational modes in a micromechanical oscillator array. *Physical Review Letters*, 90(4), 2003.

[114] S. Schmid, P. Senn, and C. Hierold. Electrostatically actuated nonconductive polymer microresonators in gaseous and aqueous environments. *Sensors and Actuators A: Physical*, 145-146:442–448, 2008.

[115] F. Sears and G. Salinger. *Thermodynamics, Kinetic Theory, and Statistical Thermodynamics*. Addison-Wesley Pub. Co., Reading, Mass., third edition, 1975.

[116] S. Shaw, K. Turner, J. Rhoads, and R. Baskaran. Parametrically excited MEMS-based filters. *in: Proceedings of IUTAM Symposium on Chaotic Dynamics and Control of Systems and Processes*, 122:137–146, 2003.

[117] M. Spletzer, A. Raman, H. Sumali, and J. Sullivan. Highly sensitive mass detection and identification using vibration localization in coupled microcantilever arrays. *Applied Physics Letters*, 88:254102, 2006.

[118] M. Spletzer, A. Raman, A. Wu, X. Xu, and R. Reifenberger. Ultrasensitive mass sensing using mode localization in coupled microcantilevers. *Applied Physics Letters*, 88:254102, 2006.

[119] M. B. Stern, M. W. Geis, and J. E. Curtin. Nanochannel fabrication for chemical sensors. *Journal of Vacuum Science and Technology B*, 15(6):2887–2891, 1997.

[120] T. Stievater, W. Rabinovich, N. Papanicolaou, R. Bass, and J. Boos. Measured limits of detection based on thermal-mechanical frequency noise in micromechanical sensors. *Applied Physics Letters*, 90:051114, 2007.

[121] T. Stowe, K. Yasumura, T. Kenny, D. Botkin, K. Wago, and D. Rugar. Attonewton force detection using ultrathin silicon cantilevers. *Applied Physics Letters*, 71 (2):288, 1997.

[122] M. Su, S. Li, and V. Dravid. Microcantilever resonance-based DNA detection with nanoparticle probes. *Applied Physics Letters*, 82 (20):3562–3564, 2003.

[123] M. Su, S. Li, and V. P. Dravid. Microcantilever resonance-based DNA detection with nanoparticle probes. *Applied Physics Letters*, 82(20):3562–3564, 2003.

[124] X. Su, C. Dai, J. Zhang, and S. J. O'Shea. Quartz tuning fork biosensor. *Biosensors and Bioelectronics*, 17(1-2):111–117, 2002.

[125] R. Syms. Electrothermal frequency tuning of folded and coupled vibrating micromechanical resonators. *Journal of Microelectromechanical Systems*, 7 (2):164–171, 1998.

[126] J. Tamayo. Study of the noise of micromechanical oscillators under quality factor enhancement via driving force control. *Journal of Applied Physics*, 97 (4):044903, 2005.

[127] J. Tamayo, A. Humphris, A. M. Malloy, and M. Miles. Chemical sensors and biosensors in liquid environment based on microcantilevers with amplified quality factor. *Ultramicroscopy*, 86 (1-2):167–173, 2001.

[128] J. Tamayo and L. Lechuga. Decrease of the resonance bandwidth of micromechanical oscillators by phase control of the driving force. *Applied Physics Letters*, 82 (17):2919, 2003.

[129] T. Thundat, G. Y. Chen, R. J. Warmack, D. P. Allison, and E. A. Wachter. Vapor detection using resonating microcantilevers. *Analytical Chemistry*, 67(3):519–521, 1995.

[130] T. Thundat, P. I. Oden, and R. J. Warmack. Microcantilever sensors. *Microscale Thermophysical Engineering*, 1(3):185–199, 1997.

[131] T. Thundat, E. A. Wachter, S. L. Sharp, and R. J. Warmack. Detection of mercury vapor using resonating microcantilevers. *Applied Physics Letters*, 66(13):1695–1697, 1995.

[132] K. Turner, P. Hartwell, and N. MacDonald. Multi-dimensional MEMS motion characterization using laser vibrometry. *in: Transducers 1999 The Tenth International Conference on Solid-State Sensors and Actuators*, pages 1144–1147, 1999.

[133] K. Turner, P. Hartwell, and N. MacDonald. Multi-dimensional mems motion characterization using laser vibrometry. *in: Proceedings of Transducers 99: The 10th International Conference on Solid-state Sensors and Actuators, Sendai, Japan*, page 11441147, 2004.

[134] K. Turner, S. Miller, P. Hartwell, N. MacDonald, S. Strogatz, and S. Adams. Five parametric resonances in a microelectromechanical system. *Nature*, 396:149–152, 1998.

[135] A. Venkatesan and M. Lakshmanan. Bifurcation and chaos in the double-well Duffing-van der Pol oscillator: Numerical and analytical studies. *Physical Review E*, 56:6321–6330, 1997.

[136] J. Verd, A. Uranga, G. Abadal, J. Teva, F. Torres, F. Pérez-Murano, and J. Fraxedas. Monolithic mass sensor fabricated using a conventional technology with attogram resolution in air conditions. *Applied Physics Letters*, 91 (1):013501, 2007.

[137] A. Vidic, D. Then, and C. Ziegler. A new cantilever system for gas and liquid sensing. *Sensors and Actuators A: Physical*, 97 (1-4):407–416, 2003.

[138] B. Wacaser, M. Maughan, I. Mowat, T. Niederhauser, and M. Linford. Chemomechanical surface patterning and functionalization of silicon surfaces using an atomic force microscope. *Applied Physics Letters*, 82 (5):808, 2003.

[139] K. Wang and C. T.-C. Nguyen. High-order micromechanical electronic filters. In *1997 IEEE International Micro Electro Mechanical Workshop*, pages 25–30, Nagoya, Japan, 1997.

[140] K. Wang, A. Wong, W. Hsu, and C. Nguyen. Frequency trimming and Q-factor enhancement of micromechanical resonators via localized filament annealing. *in: Proceedings of the International Conference on Solid-State Sensors and Actuators (Transducers 97)*, pages 109–112, 1997.

[141] Y. Wang, S. Adams, J. Thorp, N. MacDonald, P. Hartwell, and F. Bertsch. Chaos in MEMS, parameter estimation and its potential application. *IEEE Transactions on Circuits and Systems-I: Fundamental Theory and Applications*, 45 (10):1013–1020, 1998.

[142] S. Wiggins. *Introduction to Applied Nonlinear Dynamical Systems and Chaos*. Springer-Verlag, New York, second edition, 2003.

[143] Y. Yang, C. Callegari, X. Feng, K. Ekinci, and M. Roukes. Zeptogram-scale nanomechanical mass sensing. *Nano Letters*, 6 (4):583586, 2006.

[144] J. Yao, S. Park, and J. DeNatale. High tuning ratio MEMS based tunable capacitors for RF communications applications. *Tech. Digest, Solid-State Sensors and Actuators Workshop, Hilton Head Island, SC*, pages 124–127, 1998.

[145] M.-F. Yu, G. Wagner, R. Ruoff, and M. Dyer. Realization of parametric resonances in a nanowire mechanical system with nanomanipulation inside a scanning electron microscope. *Physical Review B*, 66:073406, 2002.

[146] M. Zalalutdinov, J. Baldwin, M. Marcus, R. Reichenbach, J. Parpia, and B. Houston. Two-dimensional array of coupled nanomechanical resonators. *Applied Physics Letters*, 88:143504, 2006.

[147] W. Zhang, R. Basharan, and K. Turner. Tuning the dynamic behavior of parametric resonance in a micromechanical oscillator. *Applied Physics Letters*, 82 (1):130–132, 2003.

[148] W. Zhang, R. Baskaran, and K. Turner. Effect of cubic nonlinearity on auto-parametrically amplified resonant MEMS mass sensor. *Sensors and Actuators A-Physical*, 102 (1-2):139–150, 2002.

[149] W. Zhang, R. Baskaran, and K. Turner. Changing the behavior of parametric resonance in MEMS oscillators by tuning the effective cubic stiffness. *in: Proceedings of the Sixteen Annual International Conference on Micro Electro Mechanical Systems*, pages 173–176, 2003.

[150] W. Zhang and K. Turner. Parametrically resonant mass sensor. *in: Proceedings of the Workshop on Solid-State Sensors and Actuators*, 2004.

[151] W. Zhang and K. Turner. Frequency-tuning for control of parametrically resonant mass sensors. *Journal of Vacuum Science and Technology A*, 23 (4), 2005.

[152] W. Zhang, W. Zhang, K. Turner, and P. G. Hartwell. SCREAM'03: A single mask process for high-Q single crystal silicon MEMS. In *Proceedings of the 2004 ASME International Mechanical Engineering Congress and Exposition*, Anaheim, California, 2004.

[153] J. Zou, C. Liu, J. Schutt-Aine, J. Chen, and S. Kang. Development of a wide tuning range MEMS tunable capacitor for wireless communication systems. *IEEE International Electron Devices Meeting*, pages 403–406, 2000.

[154] R. Zounes and R. Rand. Subharmonic resonance in the non-linear Mathieu equation. *International Journal of Non-linear Mechanics*, 37:43–73, 2002.

[155] A. Zribi, A. Knobloch, W.-C. Tian, and S. Goodwin. Micromachined resonant multiple gas sensor. *Sensors and Actuators A: Physical*, 122(1):31–38, 2005.

Appendices

Appendix A

Magnetically Buckled Microbeam

As discussed in Section 4.3, chaotic behavior is expected to occur in a microbeam buckled by a compressive end load. A microbeam with an end load generated by a Lorentz forces is shown in Figure A.1. Here, a DC current I_{DC} is applied to a conductive loop on the microbeam's top surface and a magnetic field is supplied by an external magnet to generate a Lorentz force F_b to axially compress the microbeam. The Lorentz force is

$$F_b = I_{DC} w_a B(\cos\theta \hat{x} + \sin\theta \hat{z})$$

where θ is the angle of the magnetic field with respect to the positive z-axis and has to be $0, \pi, 2\pi, \cdots$ in order for an axial load to be produced, I_{DC} is the DC current that is positive in the clockwise direction and negative in the counterclockwise direction, and w_a is the width of the current loop. The orientation of B and I_{DC} should be chosen such that a compressive end load is produced (i.e., in the negative x-direction).

The compressive load at the end of the microbeam will cause the microbeam to buckle to a new equilibrium position due to the double-well nature of the potential energy, a consequence of the effective linear stiffness being negative. The critical load for buckling to occur can be approximated by the Euler buckling load equation

$$F_{cr} = \frac{\pi^2 EI}{4L^2}$$

where E is the Young's Modulus, L is the length of the microbeam, and $I = w_b t^3/12$ is the moment of inertia for a microbeam with a rectangular cross section (see Figure A.1 for dimensions). The criterion for buckling, and therefore a double well potential, to occur is

$$|I_{DC} B| > \frac{\pi^2 E w_b t^3}{48 w_a L^2}$$

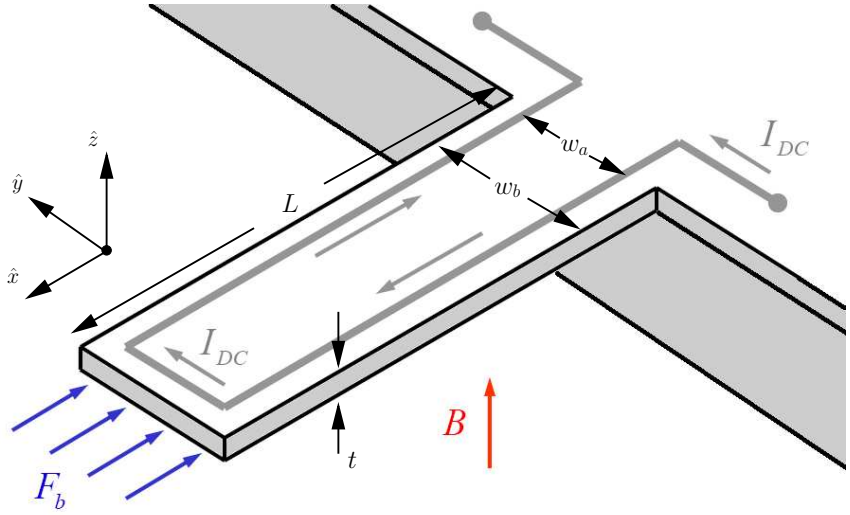

Figure A.1: Concept for a chaotic oscillator based on a microbeam buckled by an end load.

and $\theta = 0, \pi, 2\pi, \cdots$. A variety of different actuation methods (i.e. magnetic, piezoelectric, capacitive) can be used to excite the device when it is in the buckled state. Devices can be fabricated using standard micromachining techniques, similar to [103]. Melnikov analysis will be used to predict the existence of chaos for the system and the dynamics of the device will be studied numerically and experimentally.

Appendix B

Additional Chemical Sensing Experiments

The lowest frequency microbeam (M_1) of a device similar to the one studied in Chapter 7 (the only difference is the thickness of the microbeams and therefore the frequency of the localized resonances) was functionalized with a standard photoresist (OCG 825 from Arch Chemicals, Inc.), which readily absorbs volatile organic vapors. The device was base excited with a piezoelectric actuator and the motion of the shuttle mass B was sensed with a laser vibrometer. Figure B.1(a) shows the resulting frequency response when operating in a 1 *torr* environment. The device has a bulk out of plane mode B depicted in Figure B.1(b) (labeled but below the spectrum in Figure B.1(a)), and four higher frequency localized microbeam modes M_1 through M_4. Note that localized modes M_1 and M_2 are depicted in Figures B.1(c) and B.1(d), respectively, and M_3 and M_4 have similar behavior but are not depicted here for the sake of brevity. Also note that all mode shapes are obtained by using a scanning laser vibrometer.

The device was placed into a vacuum chamber with a constant nitrogen supply, which was held at 100 torr, and frequency responses of the shuttle mass B, driven near each of the localized microbeam modes were recorded. A nitrogen bubbler was then used to introduce methanol vapor into the chamber, which was again held at 100 torr, and the frequency responses were again rerecorded. The presence of methanol vapor causes the resonance peak corresponding to the polymer coated microbeam to shift downward by about 85 Hz (see Figure B.2(a)), while the resonance peaks corresponding to the uncoated microbeams undergo much smaller shifts that are induced solely through coupling (see Figures B.2(b)-B.2(d)). Upon switching the gas back to nitrogen, the resonance frequencies of microbeams shift upwards, close to their original values. Clearly these results demonstrate that the

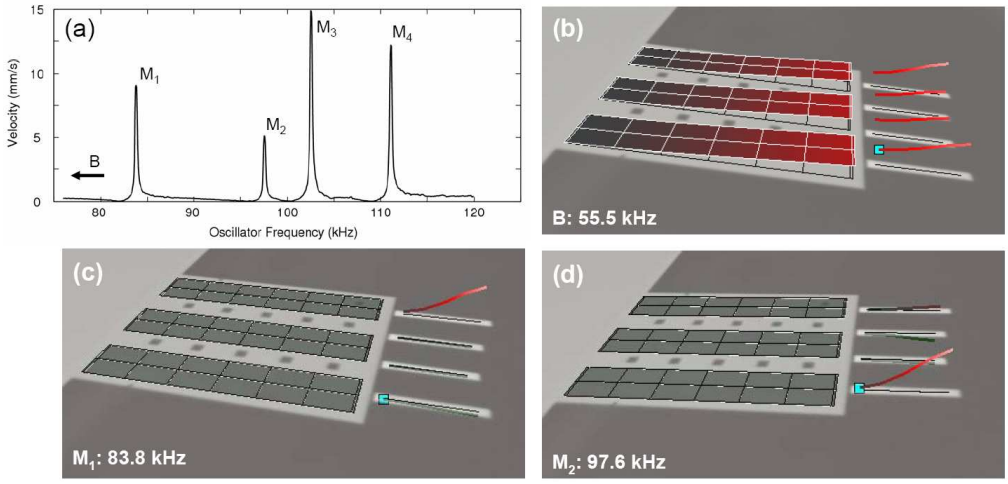

Figure B.1: (a) The frequency response of the device obtained experimentally by base exciting the sensor with a piezoelectric actuator and sensing the shuttle mass motion with the laser vibrometer in 1 Torr vacuum. (Note that the response was taken before polymer coating sensor M_1). The three mode shapes depicted in (b)-(d) were obtained experimentally by using a Polytec scanning laser vibrometer. Resonances M_1 and M_2 in (a) correspond to the modes in (c) and (d) respectively. Note that resonances M_3 and M_4 have similar mode shapes to M_1 and M_2. The mode shape in (b) corresponds to the low frequency bulk out of plane mode occurring below the resonant modes shown in (a).

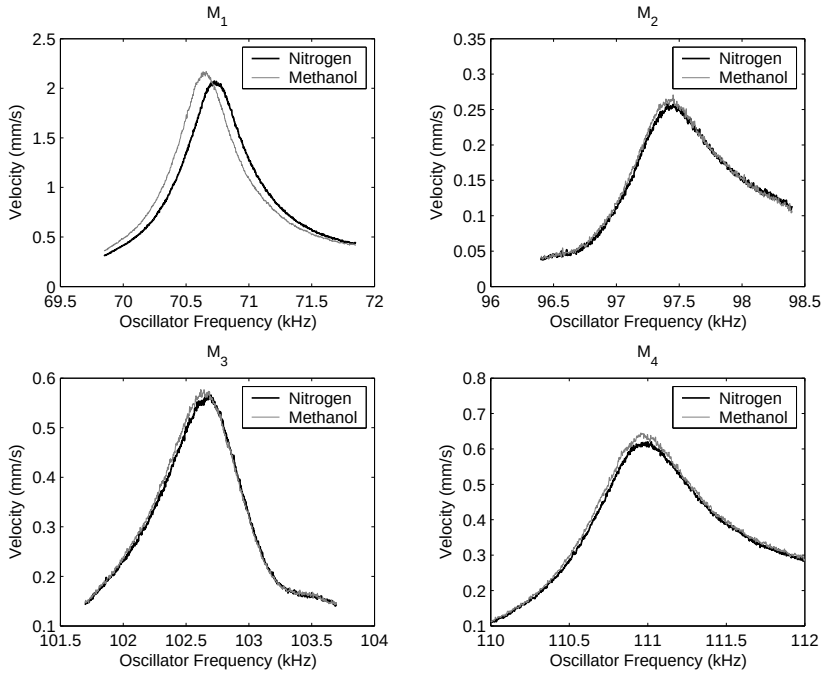

Figure B.2: Experimentally obtained frequency response curves of localized mode (a) M_1, (b) M_2, (c) M_3, and (d) M_4 for the sensor driven by a piezoelectric actuator in a 100 torr vacuum with nitrogen gas (black curves) and methanol vapor (grey curves) flowing into the chamber. (Note that the grey curves were recorded after allowing the methanol to flow for 30 minutes.) The resonance corresponding to the polymer coated microbeam M_1, shifts much more than the resonance corresponding to the uncoated microbeams due to the adsorption of methanol vapor and corresponding increase in mass.

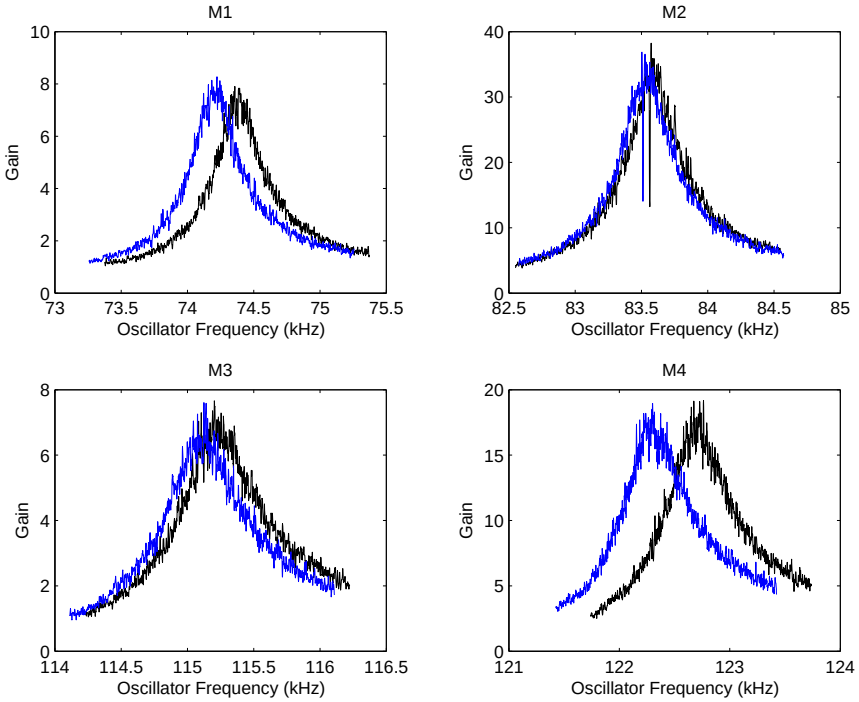

Figure B.3: Experimentally obtained frequency response curves near localized modes (a) M_1, (b) M_2, (c) M_3, and (d) M_4 when the sensor driven by a piezoelectric actuator with a band-limited white noise signal signal in $200Torr$ vacuum with pure nitrogen gas (black curves) and 6.0% methanol vapor (blue curves) flowing into the chamber. (Note that the blue curves were recorded after allowing the methanol to flow for 30 minutes.)

sensor has sufficiently localized modes, a diagonally dominant mass responsivity matrix, and possesses the ability to detect the presence of a single solvent.

In Section 7.7 of Chapter 7 the chemical detection and identification experiments were carried out using a swept sine signal to excite each localized microbeam mode. Similar results were achieved using a band-limited white noise signal to simultaneously excite all modes. This is evident in Figure B.3, which shows the downward shift of each localized microbeam mode due to the presence of 6.0% methanol vapor in the test chamber when the device was excited with band-limited white noise.

Appendix C

Q-Control

In this section Q-control of a single-degree-of-freedom (SDOF) resonator is described theoretically. Note that this method has been thoroughly investigated for SDOF resonators in previous work [5, 57, 79, 114, 127, 137]. Consider a resonator with a linear response described by the transfer function

$$G(i\omega) = \frac{1}{1 - \left(\frac{\omega}{\omega_0}\right)^2 + i\left(\frac{1}{Q}\right)\left(\frac{\omega}{\omega_0}\right)}, \tag{C.1}$$

where ω_0 is the resonance frequency and Q is the quality factor. In the feedback scheme shown in C.1(a), the motion of the cantilever is fed into a controller, summed with an arbitrary force, and fed back into the input of the cantilever. The loop transfer function for this system is

$$\mathbf{G}(i\omega) = \frac{G(i\omega)}{1 \pm C(i\omega)G(i\omega)}, \tag{C.2}$$

where the transfer function of the controller is [127]

$$C(i\omega) = e^{i\omega_0 t_0} g, \tag{C.3}$$

and g is the gain and t_0 is the time shift. In a practical implementation an amplifier would be used to provide the gain and a phase shifter would be used to provide the time shift. Note that the time shift is related to the phase shift by $\phi_0 = \omega_0 t_0$. The magnitude of the closed loop transfer function is

$$|\mathbf{G}(i\omega)| = \frac{1}{\sqrt{\left[1 - \left(\frac{\omega}{\omega_0}\right)^2 + g\cos(\omega_0 t_0)\right]^2 + \left[\left(\frac{1}{Q}\right)\left(\frac{\omega}{\omega_0}\right) - g\sin(\omega_0 t_0)\right]^2}}. \tag{C.4}$$

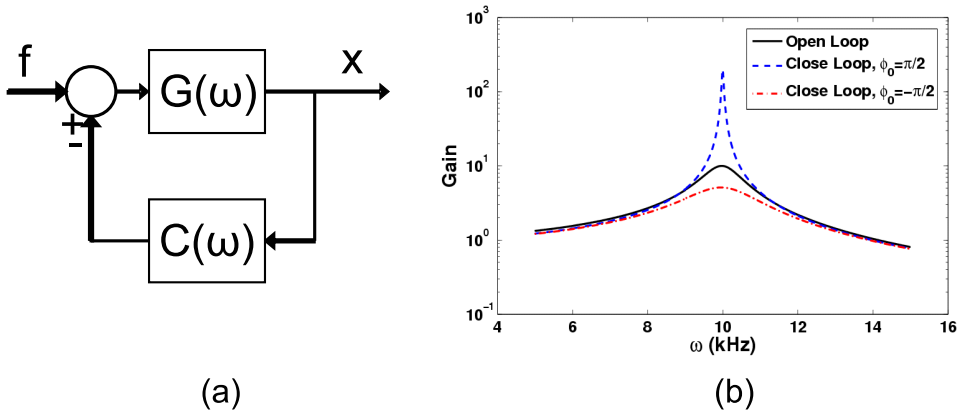

Figure C.1: (a) Block diagram of the feedback scheme used for control the quality factor of a resonator. (b) The simulated response of a resonator when operated in open loop (black solid curve), closed loop with $\phi_0 = \pi/2$ (blue curve), and closed loop with $\phi_0 = -\pi/2$ (blue curve).

Therefore, the effective quality factor is

$$\frac{1}{Q_{eff}} = \frac{1}{Q} - g\sin(\omega_0 t_0). \tag{C.5}$$

It is important to note that the effective quality factor can be controlled by adjusting the gain and phase shift. At resonance ($\omega = \omega_0$) the effective quality factor becomes very large as g approaches $1/Q$ and for $g \geq 1/Q$ Equation C.4 will have a singularity and the oscillator will become unstable (this is investigated in [100]).

The open loop and closed loop transfer function in Equations C.1 and Equations C.2, respectively, were simulated for a resonator with open loop parameters $\omega_0 = 10kHz$ and $Q = 10$. For a gain $g = 0.095$ and a phase shift of $\phi_0 = \pi/2$ the effective quality factor of the oscillator is increased. In contrast, for a gain $g = 0.095$ and a phase shift of $\phi_0 = -\pi/2$, the effective quality factor is reduced.

Appendix D

SISO Multi-Analyte Chemical Sensor Design

Here, further design considerations are discussed for the SISO multi-analyte chemical sensor detailed in Chapter 7. The dimensions of the sensor were primarily chosen based on limitations set by the functionalization apparatus discussed in Section 7.4. Future sensors can be made smaller by adopting a more sophisticated method coating method such as spray coating [55, 88, 16] or dip-pen lithography [50, 138].

The low frequency mode occurring just below the first localized and the torsional mode occurring just above the last localized mode in Figure 7.2 can be estimated analytically by making some reasonable assumptions. Since the microbeams are much smaller than the shuttle mass (their masses are two orders of magnitude smaller than the mass of the shuttle mass), the the lowest frequency mode can be approximated by the expression for the first harmonic of the isolated shuttle mass

$$\Omega_{low} \approx 3.52\sqrt{\frac{E}{12\rho}}\frac{h}{L^2}, \tag{D.1}$$

where E is Young's Modulus of silicon, ρ is the density of silicon, h is the thickness of the shuttle mass, and L is the length of the shuttle mass. The torsional mode can be approximated by the expression for the first torsional mode of the isolated shuttle mass

$$\Omega_T \approx \frac{\pi}{L}\sqrt{\frac{G}{\rho}}\frac{h}{w}, \tag{D.2}$$

where G is the shear modulus of silicon, and w is the width of the shuttle mass. Note that Equation (D.2) assumes that $h \ll w$, which is a reasonable assumption

for this architecture (in the current device $h = 5\mu m$ and $w = 310\mu m$). Applying Equations (D.1) and (D.2) to the device in Chapter 7 yields $\Omega_{low} \approx 60.0$kHz and $\Omega_T \approx 127.5$kHz, respectively. These values are reasonably close to the values obtained for the corresponding modes using FEA, which are 55.8 kHz and 137.0 kHz, respectively. These analytical approximations give a conservative estimate of the amount of available bandwidth for localized microbeam modes. This bandwidth is given by

$$B \approx (\Omega_T - \Delta_T) - (\Omega_{low} + \Delta_{low}), \tag{D.3}$$

where Δ_T and Δ_{low} are frequency offsets from the torsional mode and low frequency mode, respectively. This bandwidth will help determine the number of microbeams that can be implemented in a given design. Consider Equation (5.8) from Section 5.2.1 and assume that all resonances have the same nominal quality factor Q_{nom} and that the nominal resonance frequency of the localized microbeam modes is given by $\omega_{nom} = [(\Omega_T - \Delta_T) + (\Omega_{low} + \Delta_{low})]/2$. The maximum number of microbeams that can be implemented is given by

$$N_{max} \approx \frac{2(\Omega_T - \Delta_T) - (\Omega_{low} + \Delta_{low})}{(\Omega_T - \Delta_T) + (\Omega_{low} + \Delta_{low})} Q_{nom}. \tag{D.4}$$

Using this expression, in conjunction with finite element analysis, will help optimize the geometry to obtain the maximum number of microbeams in future SISO multi-analyte chemical sensors.